Faculty of Civil and Industrial Engineering
Department of Astronautical, Electrical and Energy Engineering

Analysis of the Water Injection Process in Industrial Gas Turbines Axial Compressor

Ph. D Candidate: Serena Gabriele

Supervisor: Prof. Domenico Borello

Reviewer: Prof. Joern Sesterhenn

Reviewer: Prof. Paolo Capobianchi

Author's Web Page: SERENA GABRIELE | ENERGY AND ENVIRONMENT (uniroma1.it)

Author's LinkedIn Page: https://www.linkedin.com/mwlite/in/serena-gabriele-b48ab438

Author's e-mails: serena.gabriele@bakerhughes.com ;

Author's address: Nuovo Pignone, Via Felice Matteucci 2, 50121, Firenze

THE PRESENT DOCUMENT IS DISTRIBUTED UNDER THE LICENSE "ALL RIGHTS RESERVED"

To my family

Abstract

In this work, the water injection process in the AXial COmpressor (AXCO) of industrial Gas Turbines (GT) has been analyzed to identify the benefits on the GT operation and the associated risks for GT and AXCO mechanical integrity.

Water injection is a technique in which a flow of water is injected and dispersed at the suction of industrial Gas Turbines. This technique has been largely used either for washing purposes or to improve GT output power in specific conditions. In the water washing application, the water injection allows to recover the performance losses due to fouling of the GT internals, while in the power augmentation application, water injection is used to increase GT power output. Although the water injection has shown to be effective in both applications, site experiences demonstrated that it could yield to components erosion with most of the damages detected in the Leading Edge section of the AXCO first stage rotor blades. Since the control and reduction of performance detriment due to AXCO fouling is of paramount importance for an industrial GT operation, the present work is focused on the water washing application; however, some of the results could be extended also to power augmentation application.

Through the analyses of the present work, the leading design parameters of the water injection system have been identified to provide a design guideline for the optimized design and optimized operation of the water washing devices. The effects of the water washing have also been assessed in terms of carbon footprint reduction of a typical industrial GT.

To identify the effects of the water injection on the GT AXCO, a dedicated Water Droplets Erosion (WDE) model has been developed and assessed against the available models. The WDE has been developed considering the effects of a wide range of droplets diameters combined with the introduction of specific materials properties characterized through a dedicated experimental campaign. The model demonstrated a clear improvement compared to the models available in literature, improving the main limitations related to the droplets' dimeters and blades material selection. The novel WDE has shown consistency with experimental results when considering a wide range of droplets diameters and when considering specific GT AXCO material characteristics.

To reduce the number of variables to be considered in the performance and design space definition, a sensitivity analysis on the WDE leading parameters has been performed on simplified GT geometries through means of CFD simulations. The results highlighted the role of the injection time and of the angle and velocity of injection as the parameters with larger effect on the washing efficiency. The injection location and the droplet size distribution seem to be the leading parameters to control the water droplets distribution on the AXCO blade.

Based on the results of the sensitivity analyses, the novel WDE has been applied on a real case where the complete geometry of a real GT has been considered form the inlet plenum up to the outlet of the first AXCO rotor. The results of CFD analyses coupled with the new WDE have been compared with field data and the shop analyses of a GT subjected to several water washing cycles. The comparison of the numerical results with the experimental field data has shown good

qualitative agreement, with the ability of highlight the impact regions and of predicting the overall component erosion.

Based on the design and operations space highlighted through the simplified geometry analyses and based on the experimental verification of the model, a complete mapping of the water washing design and operation has been created. This mapping is currently being used to create a design tool for the design optimization of the water washing devices and a monitoring and diagnostic analytic to provide indications on the optimum settings of the water washing during operation. This analytic, will be able to provide real time guidance on the optimum water washing cycles, predicting GT efficiency recovery, highlighting mechanical integrity risks and, thanks to the LCA analyses and mapping, providing information on the resulting carbon footprint of the GT.

Publications relevant to this work

1. A. Chiariotti, D. Borello, P. Venturini, S. Costagliola, S. Gabriele "*Erosion Prediction of Gas Turbine Compressor Blades Subjected to Water Washing Process*" Asia Turbomachinery and Pump Symposia. 2018 Proceedings. Turbomachinery Laboratory, Texas Engineering Experiment Station.
2. P. Venturini, D. Borello, F. Rispoli, S. Gabriele "*Prediction of water droplets erosion on a subsonic compressor cascade*", 9th International symposium on turbulence, heat and mass transfer, pp. 433-436, Rio de Janeiro; Brazil (2018)
3. M. Andreoli, S. Gabriele, P. Venturini, D. Borello "*New Model to Predict Water Droplets Erosion Based on Erosion Test Curves: Application to On-Line Water Washing of a Compressor*", Proceedings of ASME Turbo Expo 2019, Phoenix, Arizona, USA (2019)
4. P. Venturini, M. Andreoli, D. Borello, F. Rispoli, S. Gabriele, "Modelling of Water Droplets Erosion on a Subsonic Compressor Cascade" Journal of Flow, Turbulence and Combustion (2019)
5. F. Di Gruttola, G. Agati, P. Venturini, D. Borello, F. Rispoli, S. Gabriele, D. Simone, 2020, "Numerical study of erosion due to online water washing in axial flow compressors", Proceedings of ASME Turbo Expo 2020, paper no. GT2020-14767
6. I. Dominizi, S. Gabriele, A. Serra, D. Borello, 2020, "Comparative Life Cycle Assessment of different Gas Turbine Axial Compressor Water Washing Systems", Proceedings of the ASME Turbo Expo 2020, paper no. GT2020-15206
7. R. Cinelli, G. Maggiani, S. Gabriele, A. Castorrini, G. Agati, F. Rispoli, 2020, "Structural analysis of a gas turbine axial compressor blade eroded by online water washing", Proceedings of the ASME Turbo Expo 2020, paper no. GT2020-152
8. G. Agati, F. Di Gruttola, S. Gabriele, D. Simone, P. Venturini, D. Borello "Water washing of axial flow compressors: numerical study on the fate of injected droplets", E3S Web of Conferences, ISSN 2267-1242. - 197(2020), pp. 1-16 75th National ATI Congress #7 Clean Energy for all, 2020
9. F. Di Gruttola, G. Agati, P. Venturini, D. Borello, F. Rispoli, S. Gabriele, D. Simone, "Numerical study of droplet erosion in the first-stage rotor of an axial flow compressor", Turbo Expo 2021, paper no. GT2021-59661
10. G. Agati, F. Di Gruttola, S. Gabriele, D. Simone, P. Venturini, D. Borello, "Evaluation of water washing efficiency and erosion risk in an axial compressor for different water injection conditions", E3S Web of Conferences 312, 11008 (2021), 76° Italian National Congress ATI, 2021

Table of contents

List of Figures

List of Tables

Chapter 1

Introduction and thesis outline

1.1. Problem Statement

Gas Turbine axial compressor fouling is a widely acknowledged problem in the Gas Turbine Industry [1] [2]. Despite the adoption of air filtration devices, the presence of solid particles, as salt, moist and other contaminants dispersed in the airflow, at the GT air intake yields to a slow but non-negligible accumulation of solid material on the internals of the Gas Turbine [3]. Due to this phenomenon, it has been shown that an industrial Gas Turbine can lose up to the 25% ÷ 30% of its initial performances during its lifecycle [4]. Of the whole amount of the performance losses, the largest part, about the 70÷85 %, is caused by the fouling of the axial compressor [4], and specifically by the effect of the solid particles present in the air that deposit on Gas Turbine axial compressor blades altering their aerodynamic profile. Fouled compressors result in reduced airflow, lower compressor efficiency and a lower compressor pressure ratio [2]. A degradation of Gas Turbine performance is indicated by a decrease in power output and increase in heat rate. An example of the performance detriment is reported in Figure 1.

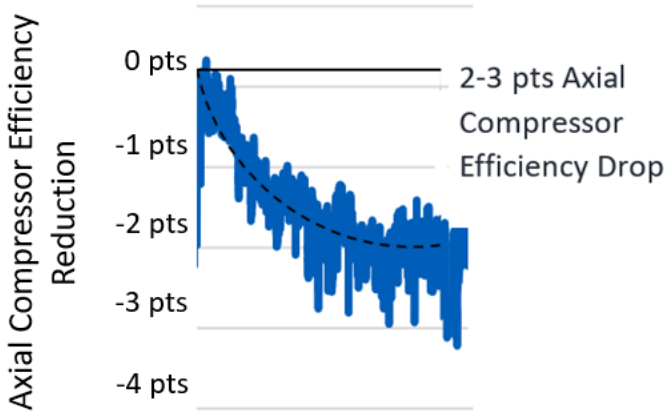

Figure 1. Gas Turbine (GT) Axial Compressor (AXCO) Efficiency Degradation Caused by Fouling. Baker Hughes archives © 2021 Baker Hughes Company - All rights reserved

For plants operating at full power and in continuous cycle, performance losses of this magnitude yield to significant profit losses every year [5]. Moreover, the decrease in Gas Turbine AXCO efficiency implies an increase of the amount of fuel needed to get the required Gas Turbine output power, with a consequent increase of Gas Turbine emissions [6].

To limit GT AXCO fouling two systems are currently used in the industrial plant: air filters to clean the air entering into the compressor [7] and on-line / off-line water washing systems to remove the residual dirt [8] [9] [10]. The difference between the on-line and the off-line water washing lies in the fact that the first is performed during GT operation, while the second is performed during GT shut-down or IDLE (low speed, no load) usually during planned maintenances. To maximize the cleaning effectiveness, both water washing systems are commonly adopted [11]. Site data demonstrated the off-line water washing technique being more effective with respect to the standard on-line water washing technique; the higher effectiveness can be mainly ascribed to additives added to the washing solution to remove grease residues, to the increase in water mass flow (about 3 times the on-line mass flow), to a longer duration of the washing procedure (typical duration of 15-30 min with respect to 5 min of on-line procedure) and to an higher penetration into the axial compressor [12]. By using off-line water washing systems field data show an efficiency recovery up to 2.5-3 pts of the overall axial compressor efficiency as shown in Figure 2.

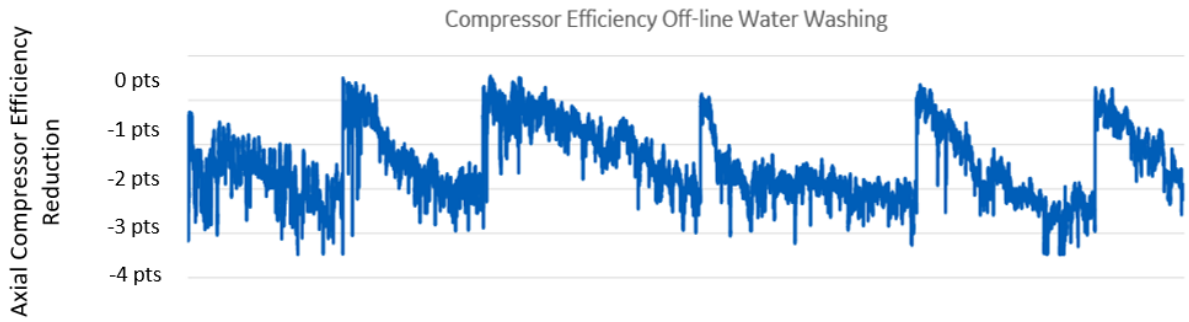

Figure 2. Off-Line Water Washing Effect on Gas Turbine (GT) Axial Compressor (AXCO) Efficiency drop in an Off-Shore platform installation. Baker Hughes archive. © 2021 Baker Hughes Company - All rights reserved

In order to ensure an optimum cleaning to maximize performances recovery, on-line washings should be at least as effective as the off-line water washings [13]. To achieve high washing efficiency avoiding the production losses associated with the GT shut down necessary to perform the off-line water washing, a novel on-line water washing has been developed and extensively tested.

The High Flow On -Line Water Washing (HFOLWW) system uses water nozzles capable to elaborate an increased water flow with respect to the standard on-line water washing devices. Typical injected mass flow rates for the HFOLWW span from 3 to 5 times the fluid mass flow used in standard on-line water washing applications, with a higher rate of water atomization and a higher water washing frequency [12]. Field tests have shown that high flow on-line water washings systems are extremely effective in recover performance losses especially in marine environment (off-shore plants) where the AXCO fouling is mainly due to salt deposits. By increasing fluid mass flow, the recovery of performances increases up to a level at which even increasing the injected mass flow it does not recover anymore [14] [15] as shown in Figure 3.

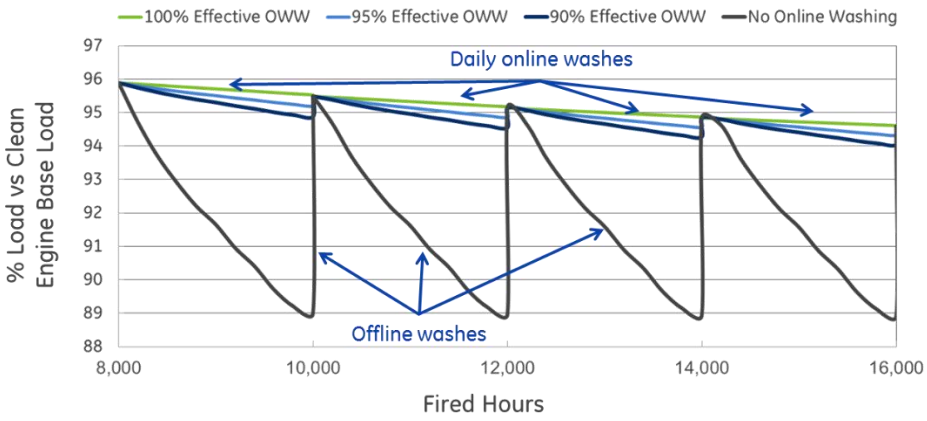

Figure 3. Effective On-Line Water Washing Vs Off-Line Water Washings on Gas Turbine (GT) Axial Compressor (AXCO) Baker Hughes achieve. © 2021 Baker Hughes Company - All rights reserved [12]

Despite the evident benefits of the use of the HFOLWW, this new technology application has shown some limitations that have to be addressed. The on-line injection of large amounts of water could emphasize the erosion effects typical of any on-line water washing [16].

It has been shown that high flow on-line washings may yield to erosion phenomena due to high-speed impact of droplets on the internal surfaces of the GT. This kind of effect has been highlighted in shop analyses as a significant erosion mainly concentrated at the leading edge of the first rotor blades of the GT axial compressors.

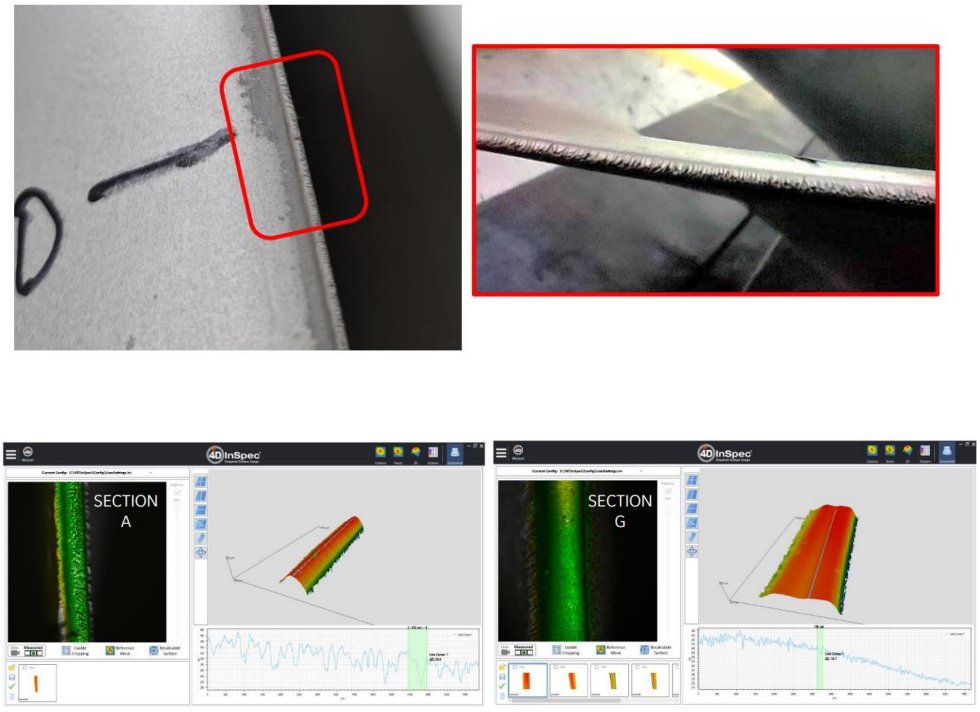

Figure 4. Erosion effect on a LM2500+ Blisk subjected to High Flow On-Line Water Washes © 2021 Baker Hughes Company - All rights reserved

Given the efficiency recovery that has been shown on field application, the adoption of the HFOLWW is very attractive since it allows to reduce the GT OPerating EXpenditure (OPEX)

ensuring the minimum possible carbon footprint. However, its application might be limited by the impacts on the mechanical integrity of AXCO rotor blades.

1.2. Literature Survey

The Water Droplet Erosion (WDE) is a form of metal erosion caused by the repeated impacts of high-speed droplets over a blade surface. This phenomenon acquired importance since the 1970s, starting with studies on the first supersonic aircraft, which presented heavy damage due to the impact with water droplets during rainstorm at high-speed flight. In a 1970 report drafted for Westinghouse, Heymann [17] tried to identify the main factors driving this phenomenon and to characterize what he called “the mysterious killer of metals”. He defined the dynamics of the material removal mechanism as based on the creation and propagation of surface cracks, which in turn lead to the formation of pit cavities inside the material and eventually removing metal chunks from the blade. In his experiments, Heymann also discovered that the erosion process starts after a certain period of exposure to droplets impingement. This period was called incubation period, later identified as one of the key parameters of the entire erosion process. Moreover, Heymann tried to identify the parameters influencing the resistance to erosion. He discovered that the hardness and strain energy characterize erosion resistance [17]. However, further analyses have shown that the strain energy is one of the less important predictors of erosion resistance when applied to a broad spectrum of materials and thermal treatments. Other experiments extended the analyses to the influence of the grain size: these experiments showed that the decreasing of the grain size improves the erosion resistance and that material containing finely dispersed small and hard particles in an elastic and ductile matrix are more resistant to erosion.

In conclusion, Heymann identified some key parameters for the WDE, but he was not able to build a comprehensive model that could predict the erosion in a various range of materials and conditions. Since 1970, the erosion was mainly studied by carrying out experimental analysis. Oka et al. [18] focused on the effective parameters governing the phenomenon. Erosion tests were conducted using a jet apparatus on an aluminium alloy under different pressure condition (from 10 MPa to 70 MPa) and various standoff distance (from 30 mm to 500 mm). These tests highlighted that jet pressure enhanced the erosion damage, while after a threshold distance the damage depth rate decreased (optimal distance). It was also demonstrated that the incubation period decreased with the increasing of jet-pressure (Figure 5). As for the relation between the impingement velocity and the erosion damage per unit mass of water, it was noted that such relation is represented by an exponential function with an exponent about 6 in the low velocity region (<100 m/s) because the impact force of the water droplets against the material rapidly decreases with the decrease of droplet velocity. At higher impingement velocities, the erosion damage per unit of mass of water was found to follow a quadratic law mainly because the erosion damage is directly related to the energy of the impinging droplet.

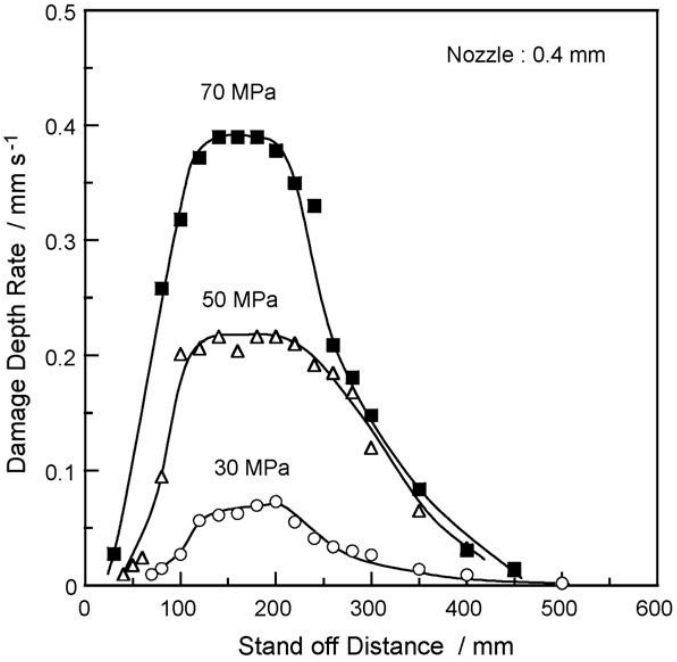

Figure 5. Effective parameters for erosion caused by the water droplet impingement and applications to surface treatment (Heymann, 1970) [17]**.**

Gujba et al. [19] performed an experimental investigation on the role and influence of impact speed on the WDE behavior. The study focused on impact speeds between 150 and 300 m/s, investigating cumulative mass losses against the exposure time and number of impingements. A rotating disc test rig was used for studying the WDE behavior; the testing rig had the capability of reaching up to 500 m/s linear speed and was provided by a working chamber coupled with a vacuum system, a compressed air driven turbine and a water droplet generating system. The study was performed on a Ti–6Al–4V alloy, a material widely adopted in the manufacturing of gas compressor rotor blades. The results showed that the higher the impact speed, the faster the erosion initiation time and the greater the erosion rate. It was also observed that the erosion rate was related to the impact speed through a log scale with an exponent of 9.9. A threshold velocity range was identified, between 150 and 200 m/s. Above such threshold, it is possible to observe the beginning of the erosion phenomenon, after an exposure time of 840 min, corresponding to 30 million impingements (Figure 6.a). The investigation carefully explored the important stages of the erosion such as the early stage of erosion damage (damage initiation stages) and advanced stages (in Figure 6.b the two stages are shown). These studies showed that the early stages were mainly limited to the formation of micro-cracks, asperities, and isolated pits of irregular shape. During the advanced stage, the hydraulic penetration was the most effective cause of material removal. Fatigue striations, walls cracks, sub surface cracks, material folding, and upheaving were also observed at the advanced stage.

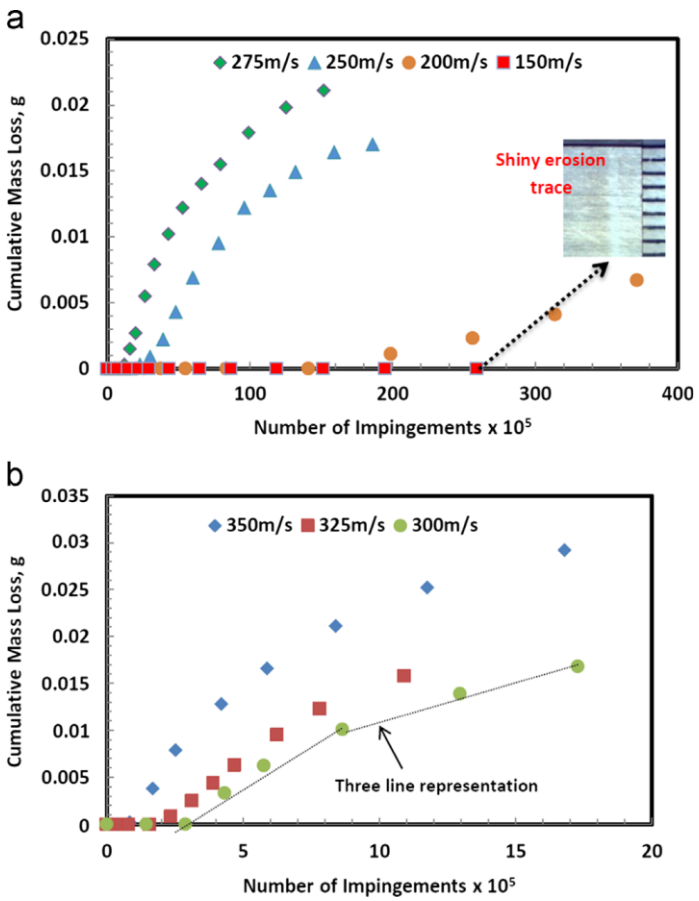

Figure 6. Threshold velocity and erosion damage (Gujba et al., 2016) [19]

While most of the analyses of the droplet erosion were experimental, numerical studies seem to be limited. Li [20] investigated the erosion effects occurred in the inner surface of nuclear power plant bent pipe by means of numerical simulations. One of the causes of WDE is the impact pressure (so called "water-hammer") exerted by the impingement of the droplets drag by the main flow. A single droplet impingement with high velocity on a solid surface was studied using volume of fluid (VOF) approach. The high Reynolds number value implies that the inertia dominates the phenomena and supports the adoption of an inviscid approach for studying the problem. The study showed that the compressibility of the liquid medium plays a dominant role in the evolution of the phenomenon. Both generation and propagation of shock waves were computed by solving the flow governing equations. The numerical results showed that critical pressure is not highest at the center of droplet surface, when the impact occurs, but it is highest behind the contact angle. This finding agreed well with the mathematical analysis and with the theoretical approximation proposed by Heymann [17].

The evaluation and prediction of the erosion effects in Gas Turbines represents an open point since no specific GT model is available in literature. The erosion mechanism, especially droplet erosion, represents one of the open issues in turbomachinery applications. Due to the geometry and the flow regimes involved, the definition and setup of experimental tests describing the erosion of the turbomachines in actual GT operating conditions represents an extremely complex problem. For this reason, the availability of specific experimental campaigns for WDE in GT is limited and no specific study seems to be available. However, the development of reliable erosion

models to be included in accurate computational codes represents a powerful support in understanding the mechanisms of blades erosion. This allows identifying the regions more exposed to erosion and the most appropriate design and operation strategies to avoid erosion damages.

To provide guidance to the assessment of performance recovery and erosion effects during on-line water washing, the present research work focuses on the development and validation of a prediction model specifically tailored for the analyses of the GT on-line water washing. The ultimate scope of the present work is to provide a design and operation space that allows the design of the on-line water washing device and its operation and monitoring to maximize the recovery of performance losses while ensuring the structural integrity of the parts.

1.3. Thesis Outline

Current PhD research is structured two main sections: in the first section the physical models and the numerical approaches are developed and tested on simplified geometries. In the second section, the developed methodologies have been applied to optimize washing effectiveness and to predict the erosion behaviour of an LT16 Gas Turbine AXCO first stage rotor subjected to water injection.

- **Chapter 2**: in this Chapter the development of a new Water Droplet Erosion model based on erosion test curves is presented. Existing WDE models and results obtained from experimental campaigns have been used to extract a comprehensive erosion model depending on droplets' velocity and diameter, impact angle and material characteristics (roughness and hardness) of the target surface.

- **Chapter 3**: in this Chapter the new WDE model developed to assess GT erosion has been applied to predict the erosion behaviour of a simplified geometry of an industrial Gas Turbine AXCO subjected to water injection. The results have been compared with those of Springer's [21] and Tabakoff's [22] models.

- **Chapter 4**: in this Chapter the analyses of the main parameters influencing the water injection process has been performed. First the model has been analysed, then a numerical analysis has been performed on the simplified geometry to quantify their impact on the washing efficiency.

- **Chapter 5**: in this Chapter the developed methodologies have been applied to predict the erosion behavior of a complete 3D model of an LT16 Gas Turbine AXCO first stage rotor subjected to on-line and off-line water washings.

- **Chapter 6**: in this Chapter, the washing process efficiency as well as the erosion rate have been evaluated by introducing specific evaluation indexes necessary to quantify the water washing efficiency. A parametric analysis was carried out by varying the flow rate of injected water on two different configurations.

- **Chapter 7**: in this Chapter a mapping of the design and operation of the online water washing has been analysed in order to define a design and operating space. Six different injection conditions have been analysed comparing the effects of the different configurations.

- **Chapter 8**: in this Chapter an Environmental Life Cycle Assessment (ELCA) has been performed to evaluate the environmental impact of an improved cleaning efficiency system. Based on actual field data, the GT performances have been evaluated before and after the introduction of the on-line washing system and the effects on the carbon footprint have been assessed.

Chapter 2

Development of a GT dedicated Water Droplet Erosion Model

Reproduced in part from: D. Borello, P. Venturini, S. Gabriele, M. Andreoli "*New Model to Predict Water Droplets Erosion Based on Erosion Test Curves: Application to On-Line Water Washing of a Compressor*", Proceedings of ASME Turbo Expo 2019, Phoenix, Arizona, USA (2019)

In this chapter a new WDE model based on erosion test curves is presented and described in detail. The novel model is then assessed against available models.

2.1. WDE Models in Literature

Erosion can be defined as "the gradual loss of a material from a surface, usually in the form of small particles and fragments, due to repeated dynamic or impulsive forces acting on the surface", thus, the mechanical stress being the primary cause in the damage mechanism [17]. When the erosion is caused by the collision of a solid surface and liquid drops at high relative velocities, the damage mechanisms is called "liquid impingement". In case the liquid impinging is water, the phenomenon is also known as Water Droplet Erosion (WDE).

There are two major contributors to liquid impingement: the high pressure generated by the fluid impacting the solid surface and the high lateral velocity of the liquid escaping to the pressure area. The fluid lateral jets can reach up to 10 times the initial droplets' velocity striking against the material and causing deformations in unfavorable oriented grains or in pronounced non - uniform structure. The depth of the region of the plastic deformation is typically 30-40 micron, depending on material characteristics and micro-cracks may generate [17]. This first phase of the erosion process coincides with the "incubation period". The duration of the incubation period depends on the material characteristics and on its microstructure. At the end of the incubation period, fatigue-like cracks begin to occur in material's weak spots as, for instance, at the base of the surface asperities. The cracks can deepen and enlarge in time, intersecting with others pits and removing material. According to Kirols, H.S. et all. [23] and Heymann F.J. et all. [17], a typical erosion test curve can be divided into three stages, as shown in Figure 7:

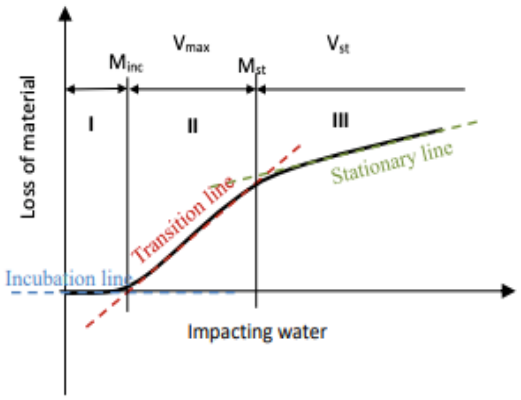

Figure 7. Erosion curve (black curve): incubation period (1), transition period (2), stationary period (3). Approximation lines: incubation period (blue dashed line), transition period (dark red dashed line), stationary period (green dashed line). [23]

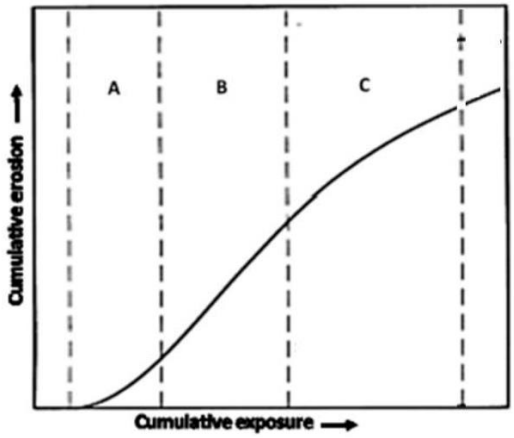

Figure 8. WDE behaviour in the transition period: A – Acceleration, B – Maximum erosion rate, C – Deceleration [23]

1. An incubation period where surface roughness increases with no material loss (generation of micro-cracks).
2. A transitional period in which erosion rate (v) increases reaching its maximum v_{max}, whose value is kept for a certain time, and then decreases (Figure 8, zones A, B and C, respectively).
3. A steady state period where there is a constant erosion rate v_{st}.

WDE curve can be well approximated with three straight segments (dashed lines in Figure 7). To identify these three lines, four characteristic parameters are needed:

- M_{inc} Impacting mass per unit surface needed to complete the incubation period.
- v_{max} Maximum Erosion Rate (eroded material per unit of impacting mass).
- M_{st} Impacting mass per unit surface needed to complete the transitional period.

- v_{st} Steady State Erosion Rate (eroded material per unit of impacting mass).

The ASTM G73-10 standard [24] proposed a method to extract the values of the four parameters from any experimental erosion curve. Such a method is illustrated in Figure 9. Each characteristic parameter depends on all the variables affecting the phenomenon: the droplet diameter d, the impact velocity v, the impact angle ϑ, the target material i.e., vickers hardness Hv and surface roughness Ra. Some experiments showed remarkable features that can link the four characteristic variables [25]. The influence of variables affecting erosion on the four characteristic variables is case specific. Let's consider, for example, the dependence from the droplets' diameter. If the droplets' diameter is greater than 1mm, then the diameter does not influence the erosion rate; if the droplets are smaller, the influence of diameter increases when decreasing droplet size [23]. For droplets in the range between 10µm to 200µm, the erosion rates are found to be dependent on d^2 [26] [27]. In the same way, several authors report dependences of the erosion rate from impact velocity that goes from $v^5$to v^{13}depending on the material and the velocity range considered [19]. To build a realistic erosion model based on empirical data, it is important to specify the material and the erosion range (in terms of droplet size and velocity).

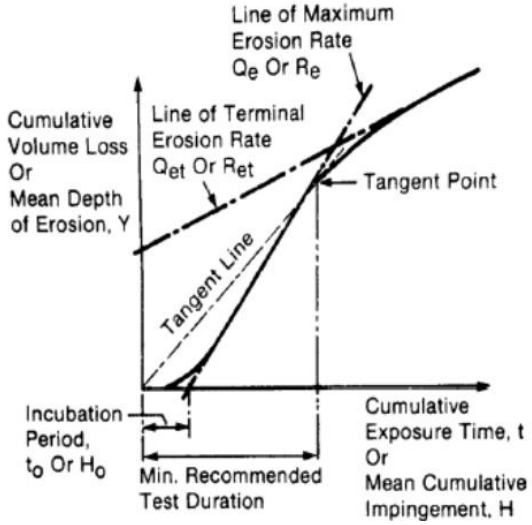

Figure 9. Method proposed by the ASTM G73 standard to extract data from an erosion curve [24]

Indeed, in some analysis (i.e., [26] [23] [19]) the behaviour seems slightly different from the general one described above: for very fine droplets, the transitional and steady state periods have the same slope, thus resulting in a single straight line (after the incubation period).

Several mathematical equations were proposed to represent the WDE behaviour. We can substantially distinguish three approaches:

1. Models based on the similarity between fatigue damage and erosion process [21], [28].
2. Models linking the erosion damage to the amount of energy applied to the surface [23].
3. Models entirely based on experimental data [26] [25] [27].

2.1.1. Models based on the similarity between fatigue damage and erosion process

This type of models starts from a detailed analysis of the liquid-solid impact. The aim is to determine, analytically or numerically, the maximum stress induced in the target material by the single impact. Once the maximum stress is known, fatigue curves are used to determine the number of impacts the material can resist to.

One of the best-known models is based on the water hammer pressure computation. Water hammer pressure is the pressure generated in the solid-liquid contact zone [23] [28].

$$P = \rho\, C_0 v_0 \left(1 + \frac{K v_0}{C_0}\right)$$

Where ρ is liquid density, C_0 the sound velocity, v_0 the impact speed and K = 2 for water.

This model leads to an excessive simplification: during the impact, a shock wave is formed in the water drop and breaks away from the droplet at a specific moment. After that, a lateral jet forms and, as the impact energy transforms into kinetic energy of the jet, the impact pressure decreases (Figure 10).

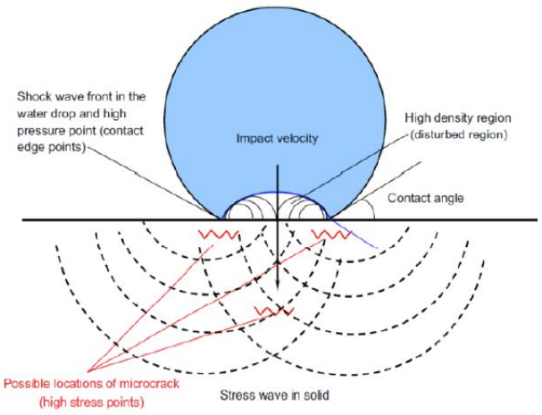

Figure 10. Schematic representation of liquid-solid impact stress and shock wave formation with maximum stress points, on and beneath the surface [28]**.**

The most challenging aspects of this problem involve solving the two coupled aspects: the transient pressure field in the liquid drop, and the stress field in the metal substrate.

Zhou et al. [28] proposed a solution for high-speed liquid/solid impact based on a nonlinear wave model. The model is developed in two parts: in the first part, the average stress induced by the single impact is computed; in the second part, an erosive behaviour occurring in two steps, the incubation period, and the constant erosion rate period, is assumed. This way the stationary period is neglected. The duration of the incubation period and the constant rate of erosion are experimentally related with the average stress by an empirical function. The average impact stress results to be dependent on droplet characteristics (velocity, dimension, and impact angle) and target material properties. The model has been developed for rain droplets whose size has been considered being 1mm.

2.1.2. Models linking the erosion damage to the amount of energy applied to the surface

If during an impact the amount of energy transferred by droplet to the target surface is constant (that is a fixed portion of the droplets kinetic energy), all erosion curves (expressed as eroded thickness, function of the energy stored per unit surface) would collapse in one. Clearly, this does not occur, and the portion of droplet kinetic energy transferred to the solid surface at each impact depends on all the quantities affecting the WDE process. Based on this consideration, an important parameter, called energy transfer efficiency coefficient ξ, can be introduced:

$$\xi = \frac{\text{transferred energy}}{\text{impact energy}}$$

This category of models aims at estimating this coefficient.

2.1.3. Models entirely based on experimental data

Since erosion is a complex phenomenon, several researchers prefer to develop models based on experimental evidence. This last class will constitute the basics of the model introduced in the next section.

2.2. New WDE Model for Stainless Steels

The new WDE model, herein developed, considers all water droplet impingement parameters and their influence on the erosion kinetic. The model is built according to Kirols [23] and Seleznev et al. [25] experiments on WDE on stainless steels, i.e. the material used for manufacturing compressor blades. The available set of experiments used to derive the model is summarized in Figure 11 indicating the examined values of droplets velocity and droplets diameter.

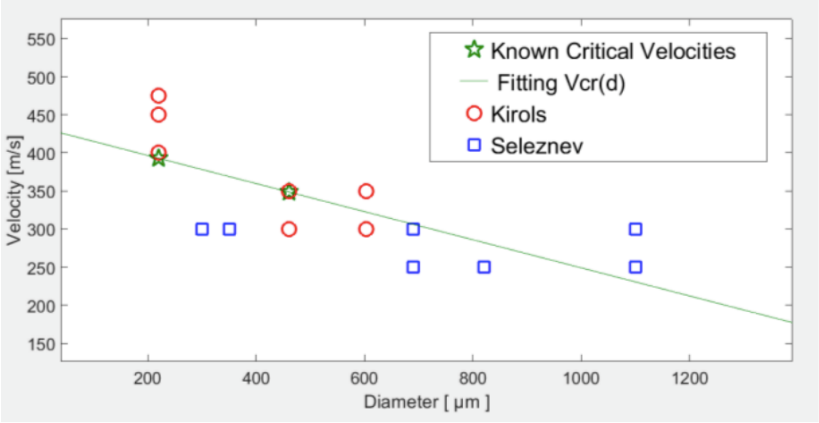

Figure 11. Experiments from Kirols [23] **and Seleznev** [25] **, and critical velocity (green line)**

2.2.1. Incubation energy and Critical Velocity

Kirols [23] noticed that for each droplet size there is a certain speed (the critical velocity) above which there is a large increase in the amount of energy transferred to the target surface during the impact. If the impact velocity is larger than this critical velocity, the incubation energy (i.e. the cumulative energy of the impacting droplets needed to complete the incubation period) per unit surface, is found to be almost constant. This value, for the tested surface roughness condition of 0.2µm average linear surface roughness (Ra), is about 200 J/mm2 (Figure 12).

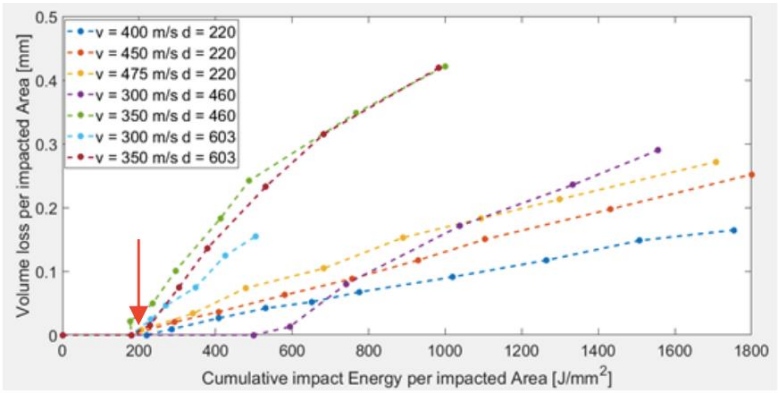

Figure 12. Erosion curves from Kirols experiments [23] **on stainless steel. Red arrow: incubation energy for impact velocity larger than the critical velocity**

In the case of droplets with diameter equal to 460µm the critical velocity is about 350 m/s, while for 603µm, such speed (not identified in Kirols data set) is expected to be lower. Critical velocity increases with decreasing droplet size. For droplets having diameter of 220µm, the critical velocity is expected to be higher than 300 m/s but lower than 400 m/s, because for this last test condition, incubation energy was found to be close to the constant value. In their experiments Seleznev et al. [25](Figure 13) confirm Kirols hypothesis. Indeed, for the erosion curves whose impact velocity is above the critical one, the incubation energy is about 200 J/mm^2, while the others, supposed below the critical velocity, have a higher incubation energy.

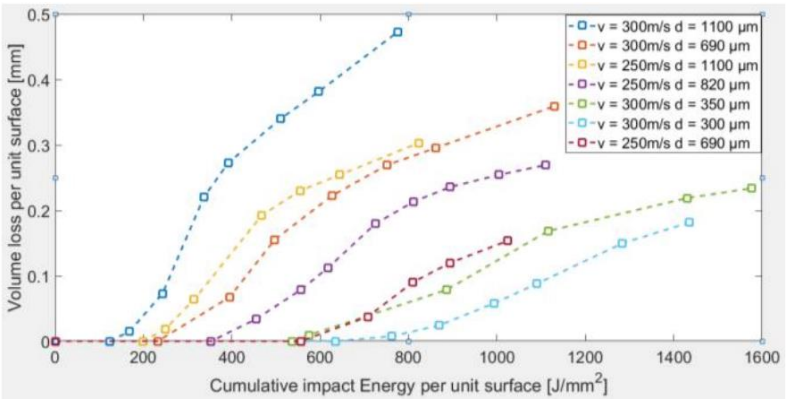

Figure 13. Erosion curves from Seleznev et al. [25] **experiments in erosion rate vs cumulative impacting energy representation**

Putting together all available experiments in the same graph (Figure 14) an approximate expression for the critical velocity can be found, v_{cr} [m/s] is expressed as a function of the droplet diameter d [µm]. A straight line satisfies very well all available experiments.

$$\mathrm{v_{cr}}\,(d) = -\,0.18446 * d + 433.47117$$

Below this value, the incubation energy increases quickly. To better understand this point and to obtain an expression that gives the incubation energy for each droplet size and velocity, in Figure 14 experimental values are plotted showing the dependence on the ratio between the impact velocity and the critical velocity ($\mathrm{v/v_{cr}}\,(d)$). The incubation energy E_{inc} is obtained from the erosion curves with the ASTM Standard G73 [24] already shown in Figure 9. Based on these data, a fitting curve is obtained (blue line in Figure 14) which writes:

$$\mathrm{E_{inc}(v,d)} = \begin{cases} 202.55 * \left(\dfrac{v}{\mathrm{v_{cr}(d)}}\right)^{-5.723} & \text{for } \left(\dfrac{v}{\mathrm{v_{cr}(d)}}\right) < 1.0 \\ 202.55 & \text{for } \left(\dfrac{v}{\mathrm{v_{cr}(d)}}\right) \geq 1.0 \end{cases}$$

Focusing on this dataset, the critical velocity can be defined as that value, dependent on droplets size, for which the incubation energy equals 202.55 J/mm^2 for the first time.

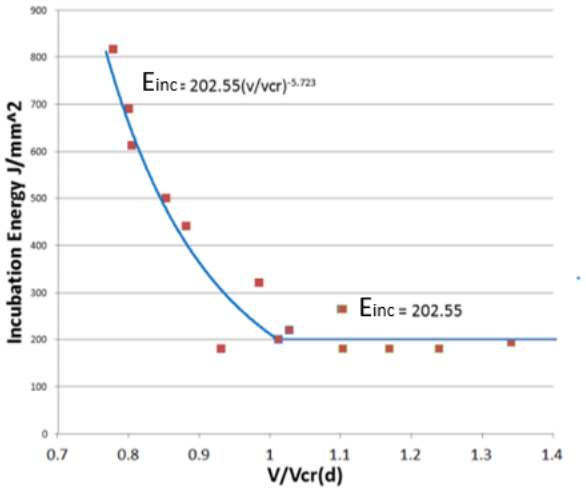

Figure 14. Incubation energy E_{inc} as a function of the impact-to-critical velocity ratio. Experimental data (red squares) and proposed fitting curve (blue line)

2.2.2. Effect of surface roughness on incubation period

The experimental data used so far are referred to an initial roughness of the target surface Ra=0.2µm. Kirols et all. [23] repeated their experiments by changing the droplet's velocities and diameters with the same material but using an initial surface roughness Ra = 0.035µm. The main effect of the roughness change on the experimental erosion curves is a variation of the incubation period as shown in Table 1.

Test	Surface finish	Incubation period (min)	Ratio between the two incubation periods (R)
v = 300 m/s	180 grit	10	1.6
d = 460 µm	polished	16	
v = 350 m/s	180 grit	3	1.5
d = 460 µm	polished	4.5	
v = 300 m/s	180 grit	5	1.7
d = 603 µm	polished	8.5	
v = 350 m/s	180 grit	2.8	1.4
d = 603 µm	polished	4	

Table 1. **Comparison of the incubation period at different surface finish [10]**

Kirols et all. [23] demonstrated that improving the initial surface roughness, the incubation period increases from 42.9% to 70.0%. Defining R as the ratio between the incubation period at a given surface roughness and the reference case (surface finish equals 180 grit), one can search for possible correlations between R and other quantities (i.e., impact velocity, droplet size). However, since from the few experiments available it is not possible to find a clear correlation, for the new WDE model, R has been considered as an average value representative of the

increase in the incubation period passing form an initial surface roughness of 0.2µm to 0.035µm. The average value is $\bar{R}$=1.5571. To build the model, a roughness coefficient Cr has been introduced. Cr is defined as the ratio between the incubation energy at a certain roughness and the incubation energy in the reference case (Ra=0.2µm):

$$\mathrm{Cr} = \frac{\mathrm{E_{inc}(Ra)}}{\mathrm{E_{inc}(Ra_{ref})}}$$

If the initial surface finishing is better than that of the reference case (i.e., Ra<$\mathrm{Ra_{ref}}$) Cr is larger than one. On the contrary, if the initial surface finishing is worse than the reference one, Cr has to be lower than one (but always bigger than zero to have physical meaning). Of course, in the reference case Cr equals one. In the case Ra = 0.035µm it is assumed Cr = $\bar{R}$. In Figure 15 the known values of Cr are shown as a function of the initial surface roughness Ra:

$$C_r = 0.66436401 * \mathrm{Ra}^{-0.254079426}$$

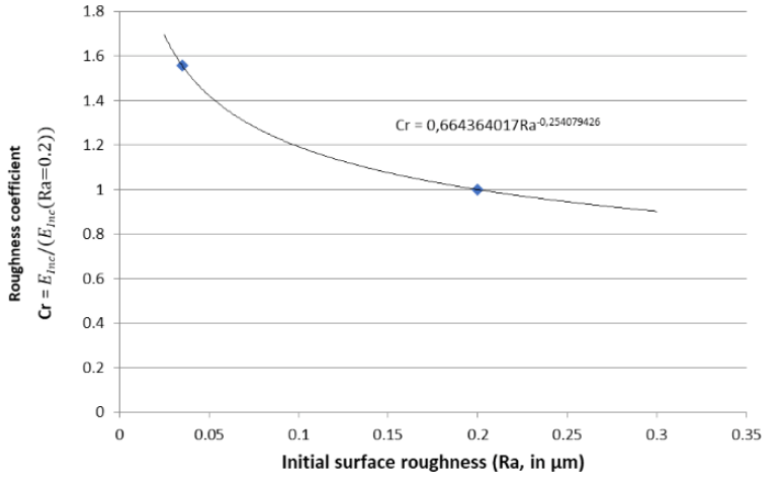

Figure 15. Roughness Coefficient i.e. Ratio between the incubation energy in the case considered and that in the reference case

The curve fits the experimental data that satisfies all conditions previously exposed. Having Cr (Ra) function, the incubation period can be modelled for any impact velocity, droplet size and initial surface roughness:

$$E_{inc} = E_{inc}(v, d)Cr(Ra)$$

2.2.3. Effect of the impact angle

Kirols [23] states that the effect of droplet impact angle is not easy to be analysed because, since the roughness of the target surface is continuously changing as the erosion proceeds, it is very

difficult to identify the actual impact angle. However, in his experiments with 100 µm droplets, Ahmad [29] measured how the eroded mass of a flat X20Cr13 specimen varies as a function of the impact angle. From those experiments, Ahmad found the erosion rate reported in Figure 16 (dots).

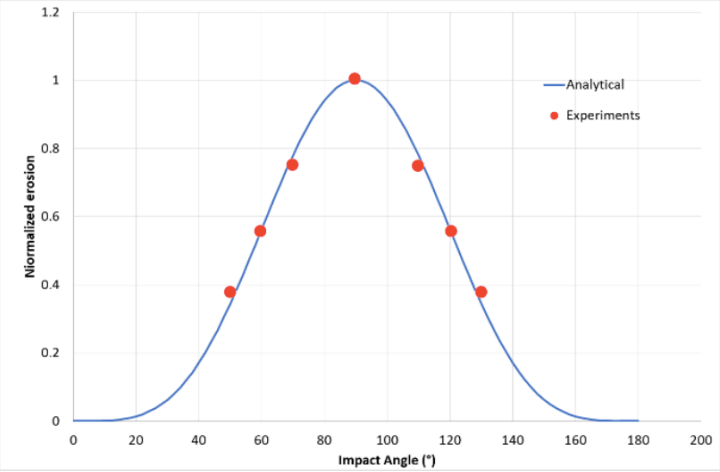

Figure 16. Normalized erosion rate as a function of impact angle. Experiments [16]: dots; analytical: continuous line

By simply considering the normal component of the impact velocity and reconstructing the Ahmad correlation for the erosion rate, the same behaviour can be found (Figure 16, continuous line). Therefore, in the present model the effect of impact angle is accounted by considering only the normal component of the impact velocity to compute the erosion.

2.2.4. Erosion Curves for small droplets

Kirol's experiments with 220µm [10] seem not to have the transitional period at maximum erosion rate v_{max} as shown in Figure 17. The erosion curve, in this case, could be well represented with just a straight line starting from the end of the incubation period.

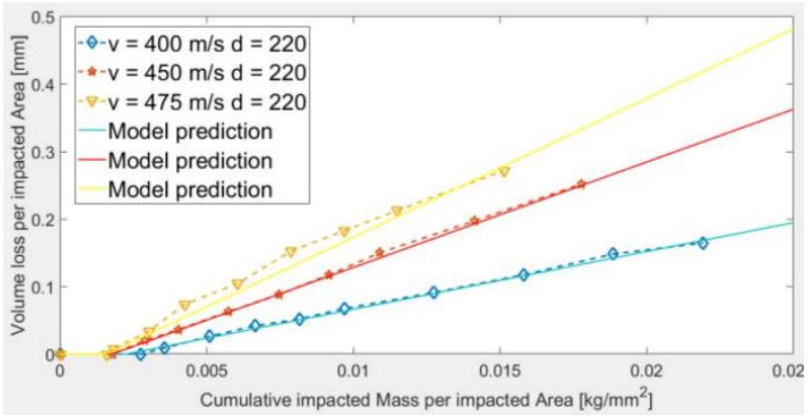

Figure 17. 220µm Kirols' experiments and straight-line model prediction for each case

Lee et al. [26] proposed a model to compute droplet erosion in large steam turbines. The model gives an expression for the erosion rate ER [mm/h], in terms of impacting droplet flow rate $\dot{m}$ [kg/mm^{2}h], droplets diameter d[µm] and impact velocity v[m/s], also considering target material's nature and hardness Hv (Vickers Hardness):

$$\mathrm{ER} = \mathrm{k}\left(\frac{\dot{\mathrm{m}}}{\dot{m}_{ref}}\right)\left(\frac{v}{\mathrm{v_{ref}}}\right)^{a}\left(\frac{\mathrm{d}}{\mathrm{d_{ref}}}\right)^{b} 10^{gHv}$$

$\dot{m}_{ref}$, v_{ref}, d_{ref} and a are constants independent from the material, while k, b and g are constants dependent on the material.

The model is calibrated on experiments whose droplets diameters are in the range 20µm-30µm. The circumstance that Lee et all [26] say nothing about the presence of a variable erosion rate and give just one expression to compute the erosion rate, strengthen the hypothesis that, under a certain droplet size value, the erosion curves have the same shape of the one obtained by Kirols for 220µm droplets. The model proposed by Lee et al. [26] has been used to verify if it fits to Kirols 220µm droplets experiments on stainless steel. To do so, it is necessary to use a different type of erosion rate with respect to the original one (ER): the erosion rate per unit of impacting droplet flow rate V:

$$\mathrm{V} = \frac{ER}{\dot{\mathrm{m}}}$$

expressed in millimetres of eroded material per impacting mass [mm/ (kg/mm^2)], i.e. the curves inclination that can be seen in Seleznev experimental graphs.

Using a Vickers Hardness of 432 for the target material, Lee model can reproduce 220µm experiments' erosion rates with very small error, as can be seen in Figure 17.

Kirols does not give specific information about test rig stainless steel hardness or nature.

d = 220 µm	v = 400 m/s	v = 450 m/s	v = 475 m/s
V_{Kirols}	8.64	15.81	20.38
V_{Lee} (Hv=432)	8.68	15.84	20.86
Δ% Lee prediction	0.54%	0.15%	2.35%

Table 2. **Comparison between experimental and computed erosion rate V (mm/(kg/mm2)) for 220µm Kirols experiments.**

In Table 2 V_{Kirols} is the erosion rate that comes from a straight-line fitting done on the three experiments while V_{Lee} is the erosion rate obtained with Lee et al. model [26] .Even if the latter model is calibrated in a different droplet size range, the found results show that it can be extended to compute the erosion rate V even for droplets size up to 220µm.

We are now able to model in two parts the WDE process for all droplets smaller or in the range of 220µm:

1) $E_{inc} = E_{inc}(v, d)\, Cr(Ra)$ – Incubation energy can be computed with the new proposed function accounting for impact velocity and angle, droplet size and surface roughness.

2) $V_{st} = V_{Lee}(d, v)$ – There is only one erosion rate that can be computed with the expression proposed by Lee taking into account velocity, droplet size and surface hardness.

In Figure 17 there is a comparison between erosion curves obtained using the new model and experiments, showing a very good agreement.

2.3. Test Cases

The proposed WDE model is applied to a blade of the first stage of a GT AXCO.

2.3.1. Simulation Details

The flow field, already studied in [30] using ANSYS CFXv16.2, was taken as an input. The turbulent flow governing equations were solved adopting a RANS closure scheme, and the well-established SST turbulence model by Menter [31] was used. Thanks to the mixing plane approach, it was possible adopting a simplified compressor geometry. The whole computational domain analyzed in the previous simulation was divided into four parts (Figure 18), and the one here studied is the 1st stage rotor (see Figure 19 for grid). Starting from the flow field solution, droplet motion was studied by adopting a Lagrangian one-way coupling approach, that is the flow field affects particle motion, but it is not affected by particles. The Newton's second law was solved for predicting particle motion, considering as driving forces only drag and pressure gradient force. Droplets are injected in a part of the inlet section of the numerical domain, varying according to the specific analysis performed (see Results and Discussion section for details). Once the dynamics of the disperse phase is simulated with the Lagrangian code, erosion is computed by comparing the results of the current model and the Springer et al. one [21]. Due to the presence of the

incubation period, it is needed to simulate a certain quantity of water to appreciate erosion. It has been assumed to consider several droplets big enough to be representative of the dynamics of the disperse phase and then a multiplication factor (MF) has been introduced to make each impact counts for a number equal to MF.

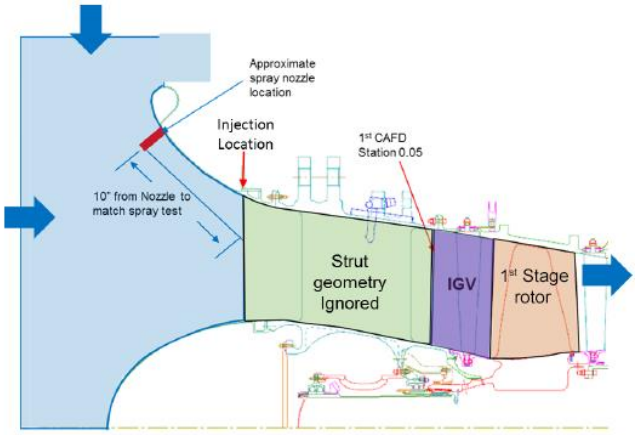

Figure 18. Geometry of the whole domain *[30]***. Present study is focused on the 1st stage rotor. © 2018 Baker Hughes Company - All rights reserved**

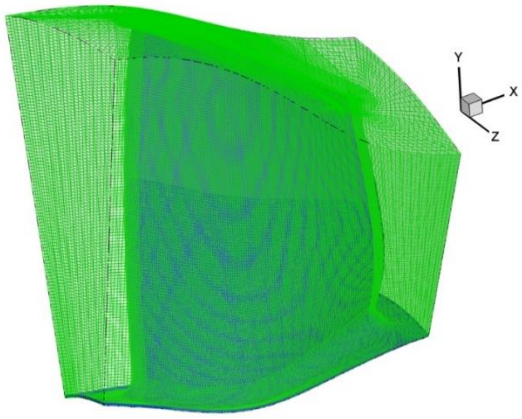

Figure 19. Discretization of the computational domain *[30]***. © 2018 Baker Hughes Company - All rights reserved**

2.3.2. Results and Discussions

To analyse the effect of all the main quantities affecting WDE process (i.e., impact velocity and angle, droplet size, roughness, and hardness of the target material) several simulations were performed. In the following sub-sections, the main results are reported.

2.3.2.1. Full simulation

In a preliminary simulation it was analysed the region of the blade inlet surface where droplets are concentrated (red zone in Figure 20). From this region more than 100,000 droplets have been injected to simulate the dynamics of the disperse phase. Droplets (100 µm diameter) enter the domain having the same flow velocity. Table 4 summarizes main characteristics of the simulated droplets. The total amount of water simulated, adjusting MF, is 540 litres. Figure 21 shows the stored energy (top) on the blade surface, and normalized erosion (bottom). The former represents the area of the blade affected by droplet impacts. However, this is not automatically converted into erosion since other quantities (i.e. incubation energy, impact angle, impact velocity, etc.) play a role in defining the final erosion. Indeed, looking at the normalized erosion pattern (Figure 21, bottom), only a part of the impacting droplets provokes erosion (red ellipse in Figure 21). Erosion pattern is a direct consequence of impact angle effect. Due to the sharp curvature of the blade in correspondence of the leading edge, this is the only zone of the blade where the impact angle is almost 90°. This results in a higher impact energy in this zone compared to the rest of the blade. WDE is strongly dependent on the normal component of impact velocity (see previous sections) and this explains why erosion is found only on the leading edge. As it can be seen in Figure 22, these results are in very good qualitative agreement with field findings.

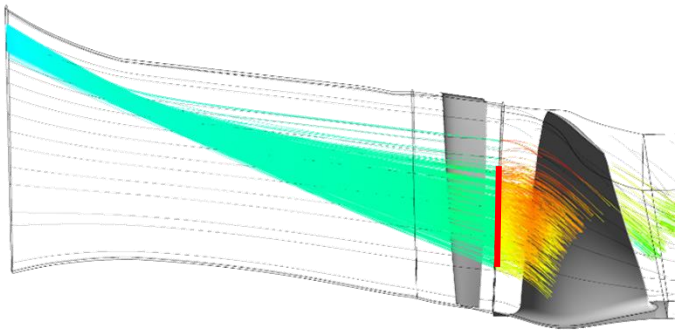

Figure 20. Preliminary simulation: trajectories of the released droplets and droplet inlet region (red line) in 1st stage rotor domain for WDE simulation *[30]***.** **© 2018 Baker Hughes Company - All rights reserved**

Table 3. Main characteristics of the simulated droplets.

Size	Inlet vel.	Material	Stk	Simulated
100 µm	Flow	Water	66.2	>100000

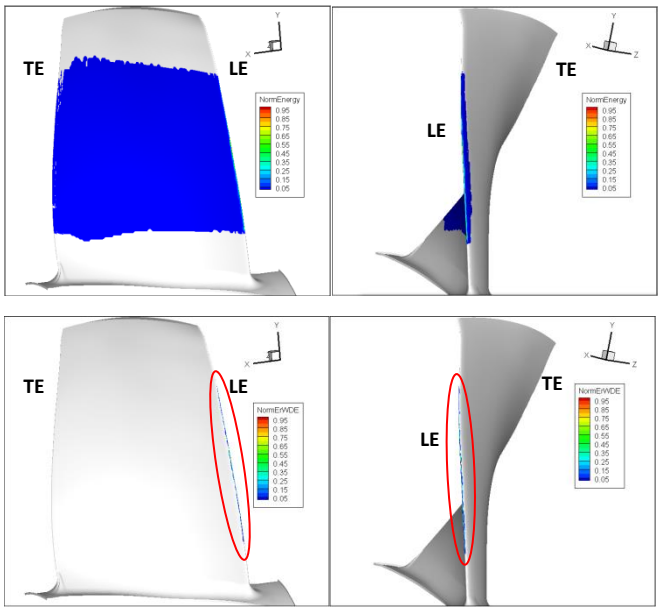

Figure 21. Normalized accumulated energy (top) and normalized erosion (bottom) on pressure (left) and suction (right) sides. © 2019 Baker Hughes Company - All rights reserved

Figure 22. Field findings of WDE from online compressor washing *[30]*. © 2018 Baker Hughes Company - All rights reserved

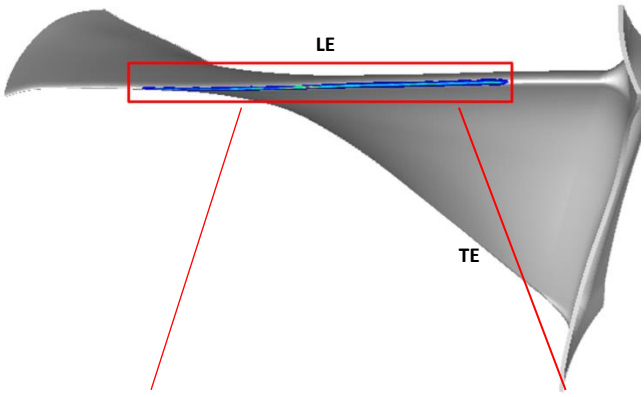

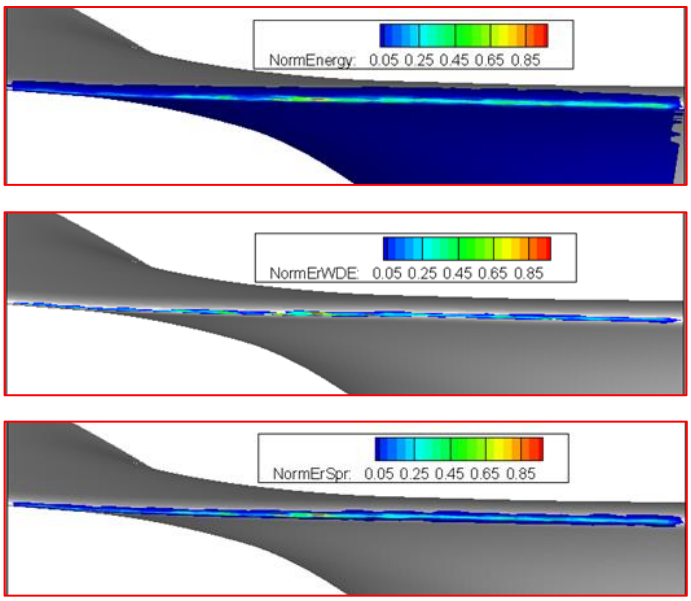

Figure 23. WDE prediction on the leading edge: normalized accumulated energy (top), normalized erosion predicted by the present model (middle) and Springer (bottom). © 2019 Baker Hughes Company - All rights reserved

Table 4. Maximum punctual results in the full simulation: 540 liters

	Springer model	**New WDE model**
Maximum erosion	2.139 mm	0.626 mm
Maximum accumulated energy	17736 J/mm^2	

In Figure 23 the different WDE predictions on the leading edge can be compared: normalized accumulated energy (top), normalized erosion predicted by the present model (middle) and Springer (bottom). In Table 4 the maximum values used to normalize the profiles are presented. As it is evident, Springer's model overpredicts the erosion. This is ascribed to several reasons: first, since Springer's model was developed to predict rain erosion of wind turbine blades, it is tuned up to very large droplets (1-7 mm). Second, material used for wind turbine blades behaves very differently from stainless steel; third, in the present model the incubation period is accurately estimated, based on experiments on material used in compressors, and using droplet size in the range used for water-washing.

2.3.2.2. Erosion at different positions on the blade

Evolution of the erosion process at different positions on the blade surface, is studied considering three different boundary cells (C1, C2, and C3 in Figure 24) and simulating 100 µm size droplets. Results are reported in Figure 25-Figure 27. Figure 25 shows the evolution of the erosion process in cell C1. Here the maximum erosion was found in the simulation and it is located exactly on the leading edge of the blade. Orange line (Figure 25 top) represents the incubation energy, that is

the energy above which erosion starts: for a given droplet size and target surface roughness, it depends on the particle impact velocity thus it is not constant. Blue line represents the energy accumulated on the C1 surface: steps in the curve means that in the considered time instant there were several impacts on the same surface. When the blue line crosses the orange line, the accumulated energy overcomes the incubation energy, then erosion can occur. This is also shown by the erosion rate (grey curve) that equals zero until the incubation energy is reached; then it is greater than zero, varying according to the impact velocity and angle. The line indicating the eroded material (Figure 25 bottom) follows this trend.

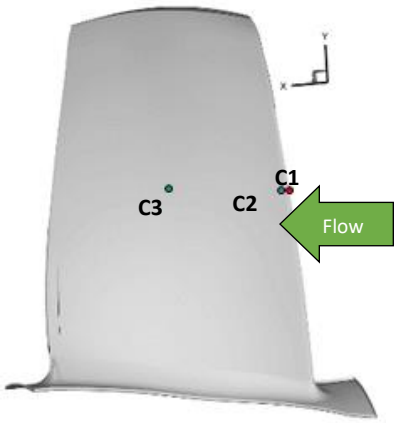

Figure 24. Boundary cells used to monitor the evolution of erosion process. ***© 2019 Baker Hughes Company - All rights reserved***

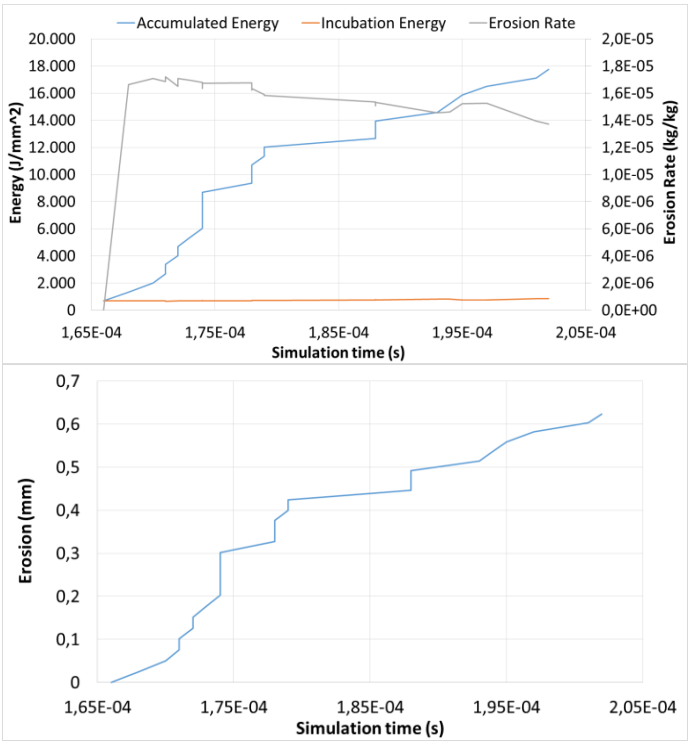

Figure 25. Evolution of the erosion process on cell C1. Accumulated energy, incubation energy, erosion rate: top; eroded material: bottom.

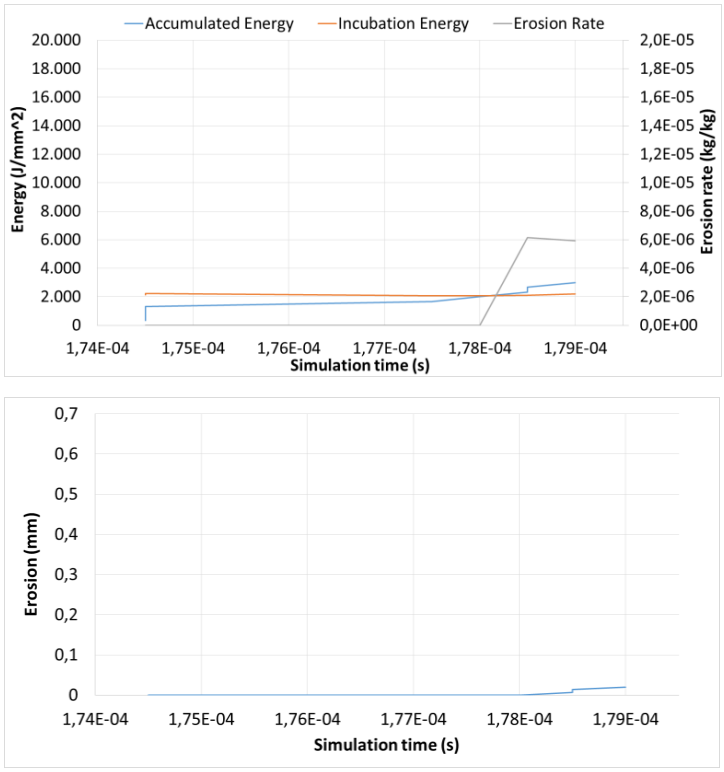

Figure 26. Evolution of the erosion process on cell C2. Accumulated energy, incubation energy, erosion rate: top; eroded material: bottom.

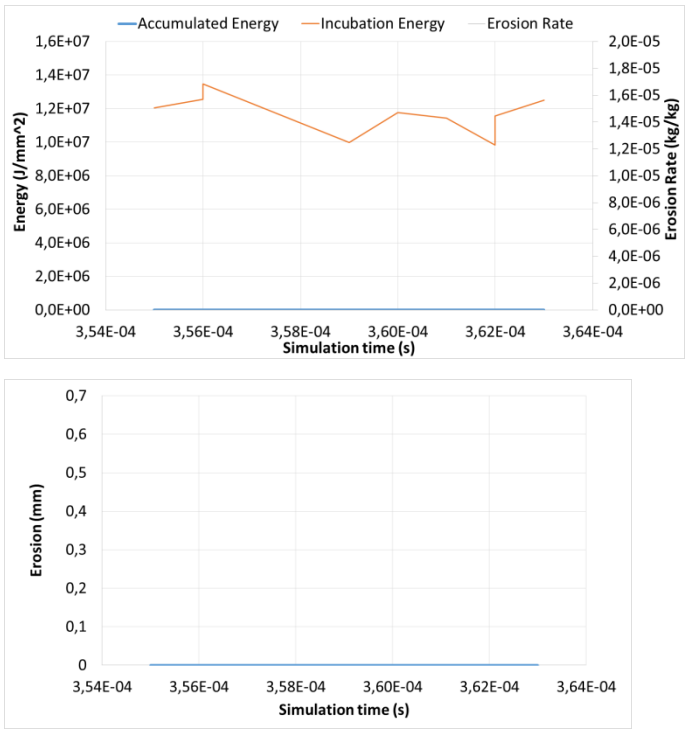

Figure 27. Evolution of the erosion process on cell C3. Accumulated energy, incubation energy, erosion rate: top; eroded material: bottom.

Cell C2 is located on the pressure side of the blade close to the leading edge. Erosion evolution in cell C2 (Figure 26) shows a larger incubation period compared with C1. This is ascribed to the fact that, in position C2, droplets impact the blade surface with a smaller impact angle because of the curvature of the blade, and this results in a smaller impact energy. The effect is even more evident when considering cell C3 (Figure 27). In this case droplets, dragged by the streamline's curvature, impact the blade surface (middle of the blade) with a relatively small impact angle. The normal component of the impact velocity is then very small as well as the impact energy. As a result, in C3 the total transferred energy is several order of magnitude lower than the incubation energy (notice that energy scale in Figure 27 is different from previous figures), then no erosion is predicted (Figure 27 bottom). With such a small normal impact velocity incubation energy is so big that likely there could never be erosion in this zone. This agrees with the fact that there is not WDE below a certain normal impact velocity [23].

2.3.2.3. Effect of initial surface finish

Three different simulations were performed to analyze the effect of initial surface roughness of the target material on the erosion process. Results of what happens on cell C2 of Figure 24, are reported in Figure 28 and Figure 29. In Figure 28 the effect of different initial roughness on accumulated energy, incubation energy, and erosion rate has been compared. As the initial roughness increases, the incubation energy decreases, which means that the incubation period reduces accordingly. This is in agreement to the findings in [26] [23]and [25]. The erosion (Figure 29) follows this trend: for very fine surface finish erosion is smaller than for rough finish. The effect is relevant on cell C2, as in the case of Ra=0.035 μm there is no erosion with the simulated amount of water; while for Ra=1 μm erosion is equal to 0.035mm.

2.3.2.4. Effect of surface hardness

Surface hardness affects the erosion rate and then the total erosion. This effect is shown in Figure 30. An increase in surface hardness results in a reduction of the erosion rate. Indeed, keeping constant the impacting energy, an increase in the surface hardness results in an increase of the energy needed to remove material from the surface, thus the same droplet is less erosive.

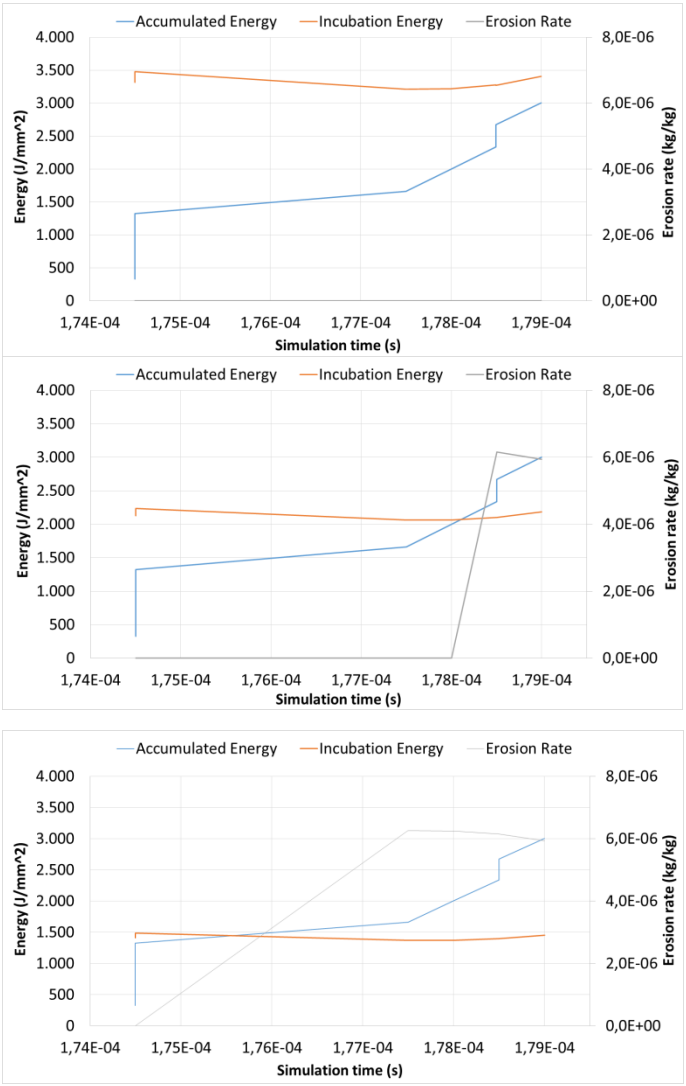

Figure 28. Effect of initial surface roughness on erosion process. Top: Ra=0.035 µm; Center: Ra=0.2 µm; Bottom: Ra=1.0 µm.

The relevance of surface roughness or hardness of the whole erosion process depends on the time interval one is interested in: for very short erosion periods, surface roughness plays a relevant role, since it affects the incubation period. On the contrary, in long erosion periods the incubation phase is less important, and the erosion rate (depending on surface hardness) becomes more relevant. In water-washing problems both the parameters may play a relevant role.

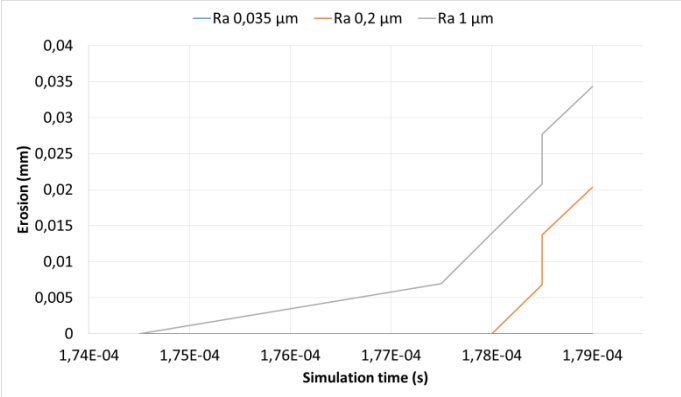

Figure 29. Effect of initial surface roughness on erosion process: erosion for different roughness.

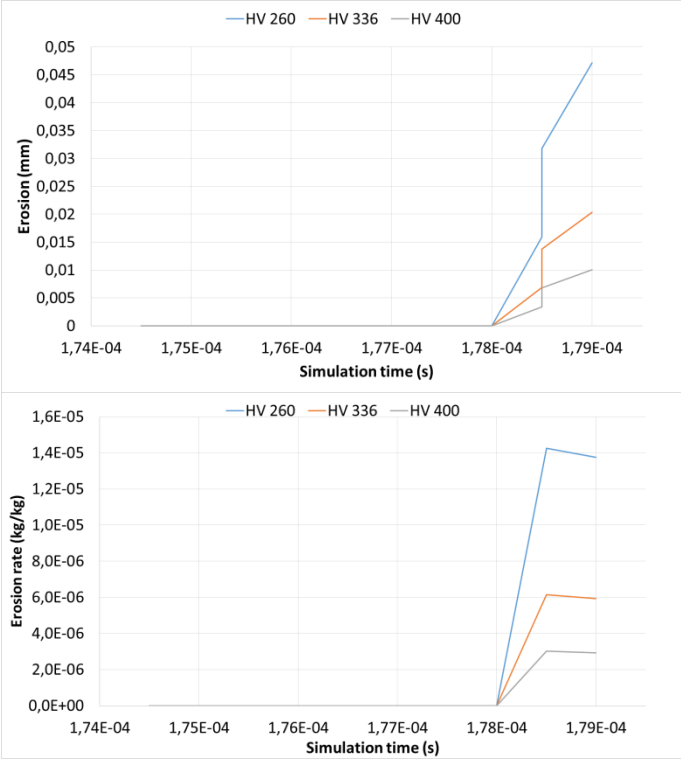

Figure 30. Effect of surface hardness on erosion process.

2.3.2.5. Effect of droplet size

The effect of droplet size on erosion process is studied performing a series of simulations injecting droplets from a narrow strip of the inlet section (see Figure 31). Stokes number is defined as the ratio between the particle response time and the fluid characteristic time scale. By means of simplification its definition yields:

$$Stk = \frac{vt}{d}$$

where v is the undisturbed velocity flow, t is the fluid relaxation time and d is the characteristic diameter of the body. For St >> 1, particles response time is much larger than fluid characteristic times and thus the particle motion is dominated by its own inertia and requires very large and strong fluid structures to be modified. For St << 1, particles response time is much lower than the fluid response time, thus the particle motion is dominated by the flow motion and particles are responsive even to small flow fluctuations. Very low Stokes particles are usually called tracers.

Keeping constant the volume of injected water (50.0 l), droplets size ranging from 25 to 200 µm have been simulated, as reported in Table 5. As it can be seen, respective Stokes numbers are quite large (inlet velocity is about 377.0 m/s), which means that droplets have a certain inertia. However, this is the size range commonly used in water-washing process, then it is important to study it. In the four simulations performed, not appreciable differences in the accumulated energy are reported, neither in quantity nor in the pattern. This is to be attributed to the fact that the same amount of water in all four simulations has been considered. In Figure 32 normalized accumulated energy on the blade is reported. This gives us an indication of the zone affected by droplet impacts.

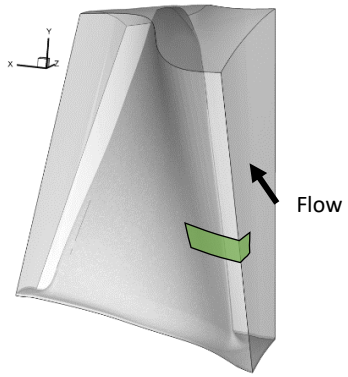

Figure 31. Droplets' injection region (green strip) for studying the effect of droplet size on WDE process. ***© 2019 Baker Hughes Company - All rights reserved***

Table 5. Simulated droplet size and Stokes number.

Droplet diameter	25 µm	50 µm	100 µm	200 µm
Stokes number	4.1	16.5	66.2	265.8

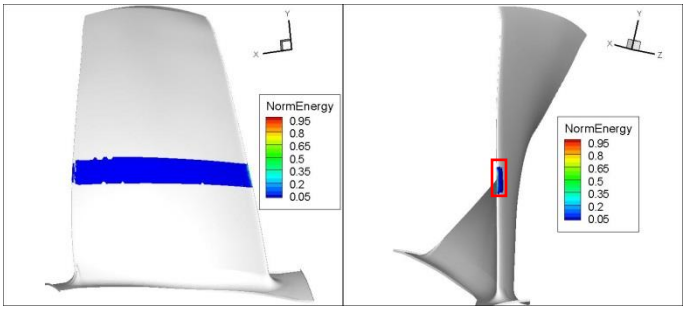

Figure 32. Normalized energy accumulated on the blade. © 2019 Baker Hughes Company - All rights reserved

Erosion is found only on the leading edge. Erosion results, normalized by the maximum erosion found in the 200 µm simulation, are reported in Figure 33. In Table 6 the local maximum found in the four simulations are reported. Contrary to what happens with accumulated energy, erosion changes a lot with droplets diameter. This is because greater droplets are more destructive. In Figure 34 the peak variation as a function of droplet size (25 µm case is taken as a reference) is shown. According to the increase in particle inertia, impact energy increases with droplet size, and hence the erosion rate tends to be more severe. Moreover, as the inertia increases, droplets impact the leading edge with an impact angle closer to 90°, which means that the normal component of the impact velocity increases. The combination of both these effects results in a larger erosion as the droplet size increases.

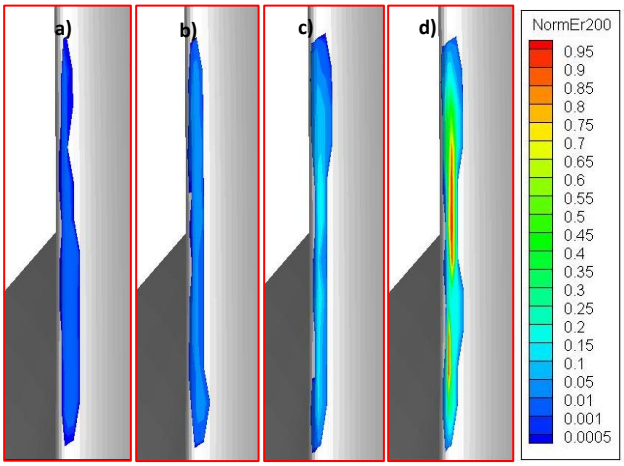

Figure 33. Normalized erosion on the leading edge (rectangular region in Figure 32) with respect to 200 µm simulation maximum: 25 µm (a), 50 µm (b), 100 µm (c), 200 µm (d). ***© 2019 Baker Hughes Company - All rights reserved***

Table 6. Maximum erosion changing droplets diameter.

Droplet diameter	25 µm	50 µm	100 µm	200 µm

Maximum erosion	0.015mm	0.074mm	0.480mm	1.489mm

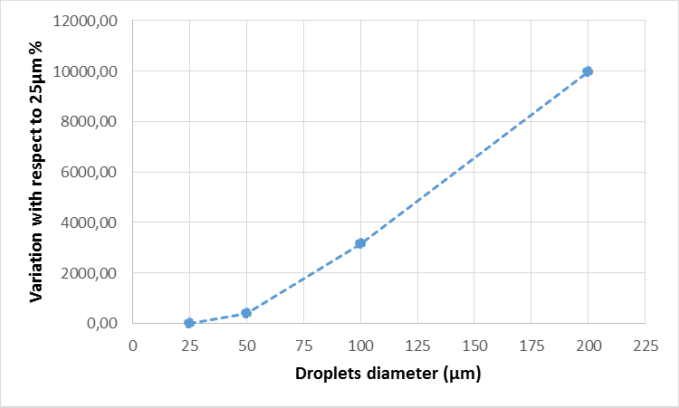

Figure 34. Variation of the erosion peak when varying the droplets diameter.

Chapter 3

Comparison of the new WDE model with erosion models available in literature

Reproduced in part from: Venturini P., Andreoli M., Borello D., Rispoli F., Gabriele S., "*Modelling of Water Droplets Erosion on a Subsonic Compressor Cascade*" Journal of Flow, Turbulence and Combustion (2019)

In this chapter a numerical analysis of the WDE phenomenon is applied to a subsonic compressor cascade, adopting three different models. The study is performed using an in-house CFD tool developed at Sapienza University of Rome.

3.1. Models

As anticipated in Chapter 2, modelling approaches to water droplets erosion (WDE) can be classified into three main categories, briefly described below.

3.1.1. Models Based on the Similarity Between Fatigue Damage and Erosion Process

This type of models [21] [28] focus on a study of the liquid-solid impact, aiming at determining, analytically or numerically the maximum stress induced in the target material by a single impact. Once this stress is known, fatigue curves are used to evaluate the number of impacts the material can resist to. Among these models, the simplest is the one based on the computation of the so-called water hammer pressure, namely the pressure that develops on the contact surface due to the droplet impact [28]. However, it could lead to an excessive simplification of the complex WDE phenomenon. For predicting rain erosion of wind turbine blades, Springer et al. [21] developed a two parts model: first the average stress induced by the single impact is computed, then an erosive behaviour occurring in two steps is assumed. After an incubation period, during which droplet impacts do not generate erosion, a constant erosion rate period develops during which the material loss increases linearly with the number of impacts. This model was then generalized for other target materials.

3.1.2. Models Linking the Erosion Damage to the Amount of Energy Discharged on the Target Surface

Assuming that during an impact the amount of energy transferred by droplet to the target is constant, all erosion curves would collapse into one. Of course, this is an approximation, because in real applications the portion of droplet kinetic energy transferred to the solid surface at each impact depends on all the quantities affecting the WDE process. Based on this consideration, an energy transfer coefficient (the ratio between the energy transferred to the target surface and the impact energy) can be introduced. This kind of models focuses on the proper estimation of this coefficient. Kirols' model [23] belongs to this category.

3.1.3. Models Based on Experiments

Due to the complexity of the WDE process, some researchers (see for instance [26] [27] [25]) preferred to develop experiments-based models in which correlations between the different quantities affecting the process and the erosion rate are found from the experimental research. Here, a numerical analysis of WDE phenomenon applied to a subsonic compressor blade has been presented, adopting three different models, one belonging to the first category, one to the last, and one related to solid particle erosion, described in the following sections. The study is performed using an in-house CFD tool developed at Sapienza University of Rome coupled with an in-house particle/cloud tracking software. In view of approximations involved in modelling WDE, complex unsteady multi-phase Flow, Turbulence and Combustion flow simulations such as DNS or LES [26] seem inappropriate. It has been considered sufficient to carry out Hybrid LES-RANS study [32]. As for the droplets tracking, different coupling approaches (namely one-way, two-way, and four-way coupling, [33]) are possible, depending on the concentration and size of droplets/particles. Since in the present application the droplet concentration is relatively small, a one-way coupling approach has been adopted. This allows to perform a CFD calculation and to compute subsequently droplets tracking and erosion simulation.

3.1.4. Unsteady Turbulence Models

The unsteady turbulent flow is solved using a seamless hybrid LES/RANS model. The adopted hybrid model uses the dynamic Smagorinsky LES proposed by Germano et al. [34] with a near wall treatment based on the elliptic relaxation ζ-f turbulence model. This near-wall treatment can recover the turbulence anisotropy induced by the presence of a solid wall, as demonstrated in [35]) Details of the model and numerical validation can be found in [35]. The dispersed phase tracking model adopts a Lagrangian one-way coupling approach [36] in which equation of motion of the dispersed phase is solved, assuming that drag is the only relevant force acting on droplets. Since rotation is not accounted for in the present case, no apparent forces (i.e. Coriolis or centrifugal forces) are considered. Such forces affect droplet dynamics, thus can influence their trajectories, impact velocity and angles, and might lead to different blade erosion patterns.

Present work focuses on the comparison and assessment of erosion models in which the influence of rotation was disregarded. However, apparent forces were considered in other publications on the same topic (see for instance [[30], [37], [38], [39]). Three different erosion models are adopted: two of them have been developed for simulating WDE, and the third one is for solid particle erosion. The aim of the comparison is to show the importance of selecting the proper model. The erosion models used for comparison are the Springer et al. model [16], developed for wind turbine materials but then extended to other materials; the Tabackoff et al. model [22], for solid particle erosion of ductile materials; and the present WDE model developed by the authors based on experiments reported in the literature specifically for WDE of metal surface [39]. The three models directly or indirectly account for target material properties, that in the present work is assumed to be stainless steel. The material properties and model coefficients/constants are, therefore, selected accordingly.

The novel WDE model described in Chapter 2 is compared with the two models described in the following paragraphs.

3.1.5. Springer's model for water droplet erosion

In the last decades several models for predicting droplet erosion have been proposed (i.e., [26] [21] [40] [41]). Among them, Springer et al. approach [21] is considered the more general and widely used. Springer et al. expressed the erosion rate (that is, the amount of eroded mass per impacting droplets) as a function of the properties of both the droplets and target material (including possible coating protection layer), together with the impact velocity and angle. Besides, it accounts for the incubation period, identified by Heymann [17] as one of the Flow, Turbulence and Combustion key parameters of the entire WDE process. The incubation period is the minimum number of droplet impacts (n_i) below which the erosion process does not occur. Knowing the concentration and flow of droplets, it is easy to convert n_i into a time interval (the incubation period). After n_i impacts the erosion rate linearly increases with the number of impacts until a second threshold number of impacts n_f is reached. Then, the erosion process becomes almost independent from the successive droplet impacts. A typical erosion curve is reported in Figure 35. Denoting with m the eroded mass per number of impacted droplets, the model is formulated as:

$$\begin{cases} m = 0, & if \;\; n < n_i \\ m = \alpha\left(n - n_i\right), & if \;\; n_i < n < n_f \\ m = const, & if \;\; n > n_f \end{cases}$$

where n denotes the number of impacts. The minimum number of impacts needed to have erosion (n_i) depends on the impact pressure, which in turn is a function of the properties of the target material. This is called the water hammer pressure, defined as

$$P = \frac{z_R v_{imp} \sin\beta}{1 + z_R / z_C}$$

where, v_{imp} is the impact velocity, β is the impact angle, *z* is the impedance and subscripts *C* and *R* refers to coating and substrate materials, respectively (Springer assumes that the blade is formed of a coating layer and a substrate). The slope α is related to n_i by the following empirical expression

$$\alpha = \alpha^* \pi \rho_w d^3 / 6$$

being

$$\alpha^* = 0.023 \left(\frac{1}{n_i^*} \right)^{0.7}$$

$$n_i^* = 7.0 \cdot 10^{-6} \frac{S_{eff}}{\bar{\sigma}_0} = n_i \frac{\pi d^2}{4}$$

ρ_w is the droplet density, S_{eff} is a quantity accounting for the properties of the target material, σ_0 is the mean stress at the impact point, and d is the droplet diameter. The material properties are selected according to the target material assumed. For further details see Springer et al. [21].

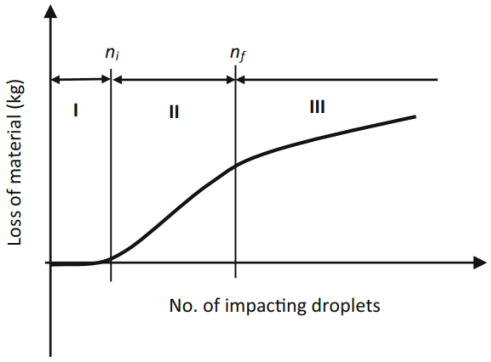

Figure 35. Erosion curve: incubation period (I), transition period (II), stationary period (III)

3.1.5.1. Solid particle erosion

Solid particle erosion is modelled by adopting the well-established semi-empirical model of Tabakoff et al. [22]. The model consists of an empirical correlation that can predict the erosion per unit mass of impacting particles (ER, in mg/g) of several materials:

$$ER = K_1 f_\alpha \left|\mathbf{v}_{bc}\right|^2 \cos^2\alpha\left(1 - R_T^2\right) + f_i$$

where

$$R_T = 1 - 0.0061\left|\mathbf{v}_{bc}\right|\sin\alpha$$

$$f_\alpha = \left\{1 + K_C\left[K_{12}\sin\left(90\alpha/\alpha_0\right)\right]\right\}^2$$

$$f_i = K_2\left(\left|\mathbf{v}_{bc}\right|\sin\alpha\right)^4$$

α is the impact angle, and α_0 is the angle of maximum erosion for the given material (about 30° for stainless steel); K_1, K_2 and K_C depend on the material properties of particles and target surface. The material coefficients adopted in this work are those for coal ash particles impacting a stainless-steel surface, as reported in Table 7 [22].

Table 7. Erosion model coefficients

K_C	$\alpha \leq 3\ \alpha_0$	1
	$\alpha > 3\ \alpha_0$	0
K_1		1.505101×10^{-06}
K_{12}		0.296077
K_2		5.0E-12

3.2. Numerical Details

The main details of the considered computational domain are reported in Table 8. Numerical predictions of flow in these configurations have been reported by some of the present authors in several publications since 2009, e.g. [42]. A sketch of the grid used for solving the flow field is shown in Table 8. Droplets enter the domain from a portion of the inlet section, and they are uniformly distributed along the whole blade pitch and span. Since the flow field has non-negligible fluctuations surely affecting the droplet motion, this effect has been accounted by dividing the wake oscillation period (T = 1.35 10−3 s) into 30 consecutive realizations (one every 4.5 10−5 s). At the proper time instant the right realization is provided to the particle laden flow solver (P-Track), and it is assumed to be constant until the next realization is loaded. In other words, the flow field seen from droplets/ particles is variable in steps. This is considered sufficient to consider the influence of time dependent fluctuations on the particle motion. As for the spatial discretization, a large part of the domain is solved by LES and the Unsteady RANS solution is limited to very thin regions where viscosity effectively dumps the turbulent fluctuations. In this way it has been assumed that the unresolved fluctuations were properly addressed. At each realization (new configuration of the flow field), 80 droplets per starting cell enter the domain from randomly generated positions, having the same velocity as the flow field. The droplets are individually tracked, and once they impact a solid wall erosion rate is predicted. The size of the

injected droplets/particles is 50 µm, which corresponds to a Stokes number (S_{tk}) equal to 0.8. Such S_{tk} value is representative of a transition regime from the particle inertia point of view. Indeed, when S_{tk}> > 1 particle inertia is large making the particles react slowly to flow fluctuations; when S_{tk} <<1 inertia is small, and the particle response is quicker. In the range 0.8-1.2 the S_{tk} is in a kind of transition regime, thus particle inertia is important but not large enough to annul the effect of flow fluctuations on particle motion.

3.3. Results and Discussion

The flow field analysis of this test case already discussed in [42] is not reported here. Figure 37 [32] shows the instantaneous iso surface Q = 60 colored with pressure, and some streamlines. The two main turbulence structures are highlighted with ellipses (tip leakage vortex: continuous line; hub vortex: dashed line). The tip leakage flow (TLF) gives rise to a large vortical structure, while the strong adverse pressure gradient in the aft part of the suction side (SS), near the hub, provokes a large flow separation leading to the birth of the hub vortex. These features originate from the specific domain geometry since a linear cascade cannot be optimized to reduce the effects of secondary motions. This circumstance will affect the droplet motion and hence the erosion patterns. Figure 38 reports the trajectories of some of the droplets injected. The effect of the TLF is evident: droplets in the pressure side (PS) are captured by it and dragged toward the SS (Figure 38 -left). Droplets injected in the same region but in the SS are trapped by the large vortex and do not impact the blade. Moving toward the hub, droplets in the PS still feel the effect of TLF. However, because of the inertia, most of them impact on the blade tip (see zoom in Figure 38 left). In the other regions of the blade the flow field does not show any relevant motion apart from that close to the hub. In this region the hub vortex (HV) entraps the droplets and drags them toward the blade wall up to about the mid-span (Figure 38 -right). Figure 39 shows the energy accumulated on the blade surface due to impacts. The energy levels are normalized with its maximum. The energy accumulated on the blade surface is only dependent on droplet dynamics (i.e., trajectory and velocity) and not on the erosion model used, thus it is the same in all the simulations. Firstly, it can be noted that while the PS is completely affected by impacts (and then the energy accumulates on the whole side, Figure 39-left), the SS is less exposed to them (Figure 39-right), as demonstrated by the presence of wide regions without energy accumulated. This is due to the combined effect of droplet inertia and blade geometry: because of the blade curvature, droplets tend to leave the SS rather than going toward it, thus they hardly impact that side. On the SS, droplets impact on three main regions (Figure 39-right): the leading edge (LE, continuous ellipse), the tip (dashed ellipse), and the bottom part of the blade (dot-dashed ellipse). Most of the impact energy is accumulated on the LE. The TLF entraps droplets and then push part of them toward the tip of the blade. The accumulation of impact energy on the bottom part of the blade is due to the interaction of droplets with the HV shown in Figure 38 -right and Figure 40- bottom. Anyway, the zone in which the larger amount of impact energy is accumulated is the LE. As said above, the accumulated energy is due to droplet dynamics, a combination of impact angle and impact velocity. Droplets impacting on the LE show a high impact angle (close to 90°, that is they impact almost normally to the target surface), thus the normal component of the impact velocity is very high. On the contrary, on the other parts of the blade, the impact angle

or the impact velocity are smaller, as well as the energy accumulated. For the same reason at the hub and the casing accumulated energy is very small.

Table 8. Details of the simulated case

Chord length	Stagger angle	Inflow angle	Pitch	Span	Axial chord length	Passage width	Tip gap	Bulk velocity
25.4 cm	56.9°	65.1°	0.929 of chord	25.4 cm	13.868 cm	23.6 cm	1.65% of chord	25.0 m/s

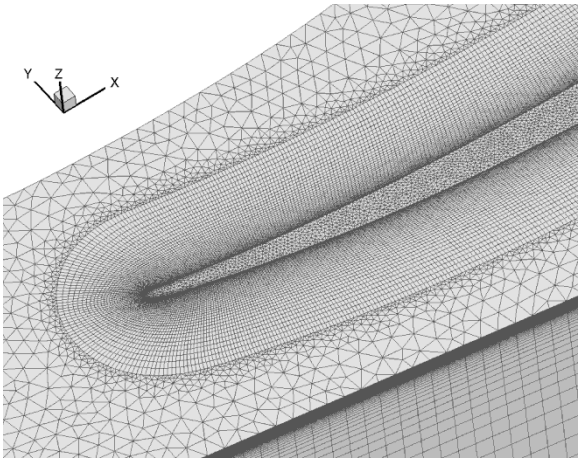

***Figure 36. Computational grid*.**

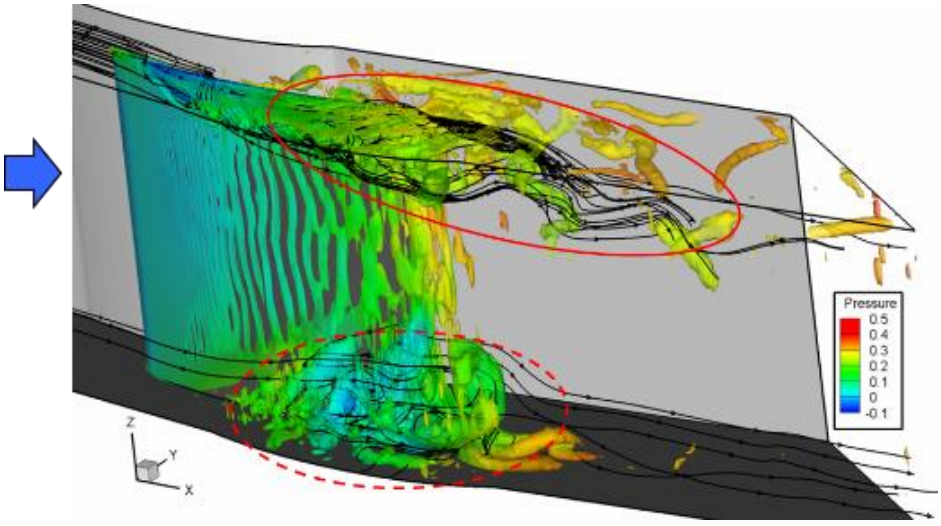

Figure 37. Isosurface of Q=60 colored with pressure

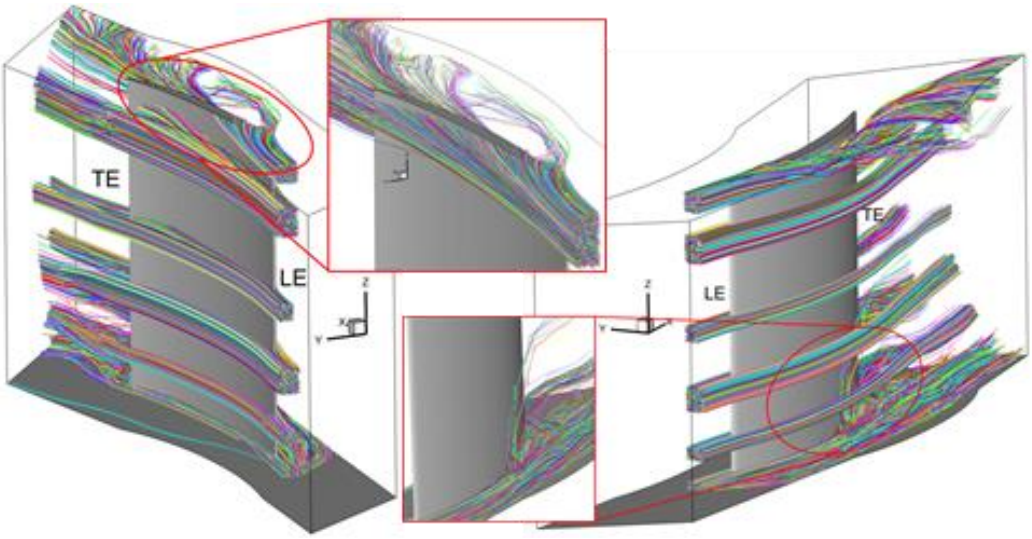

Figure 38. Some droplets trajectories (left: PS; right: SS; LE: leading edge; TE: trailing edge).

The impact energy accumulated on the PS (Figure 39-left), is concentrated on the LE (continuous ellipse, where the peaks are found), and at the tip (dashed curve) and root (dash-dotted curve) of the blade. Impacts on the tip region are again due to the TLF that entraps droplets and drags them toward the SS. Along this path some of the droplets impact on the tip of the blade because of their inertia (Figure 38-left). The curvature of the blade plays a role for those impacts occurring close to the trailing edge, for both the tip and the root. The accumulated energy translates into eroded material depending on the model used. In Figure 41 the prediction of the proposed WDE model (left) and that of the Springer et al. model (right) are compared. The present WDE model does not predict any erosion, while Springer et al. model predicts erosion only on the leading edge. To assess the superior performance of our WDE model, Kirols [23] model can be recalled stating that for stainless steel (the material we are assuming for the blade in our simulations) the threshold velocity is about 150 m/s. Here the bulk velocity is 25 m/s, therefore in this case erosion is not expected, in agreement with the prediction of the present model

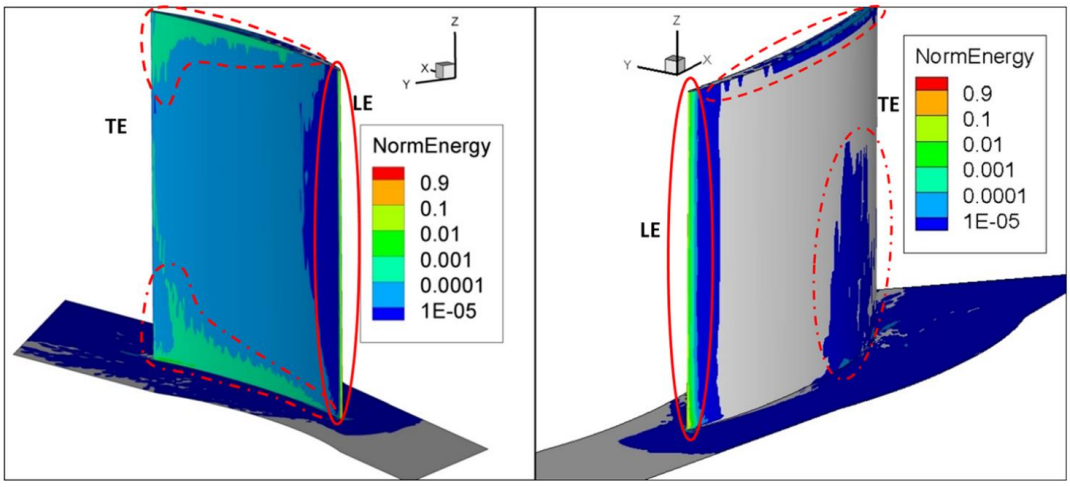

Figure 39: Energy stored on the blade surface (left: PS; right: SS; LE: leading edge; TE: trailing edge).

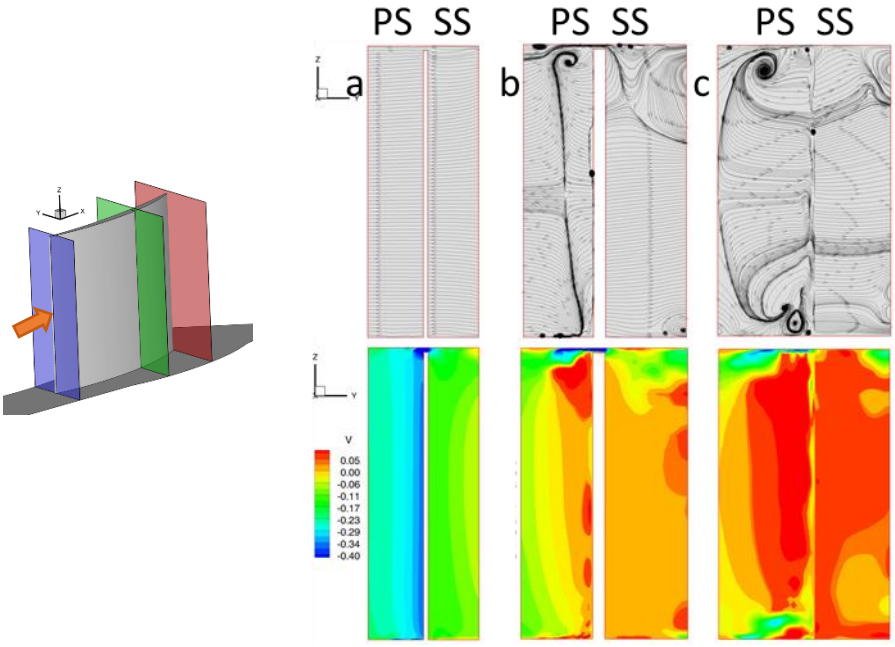

Figure 40. Streamlines (top) and y-component of the flow velocity (bottom)

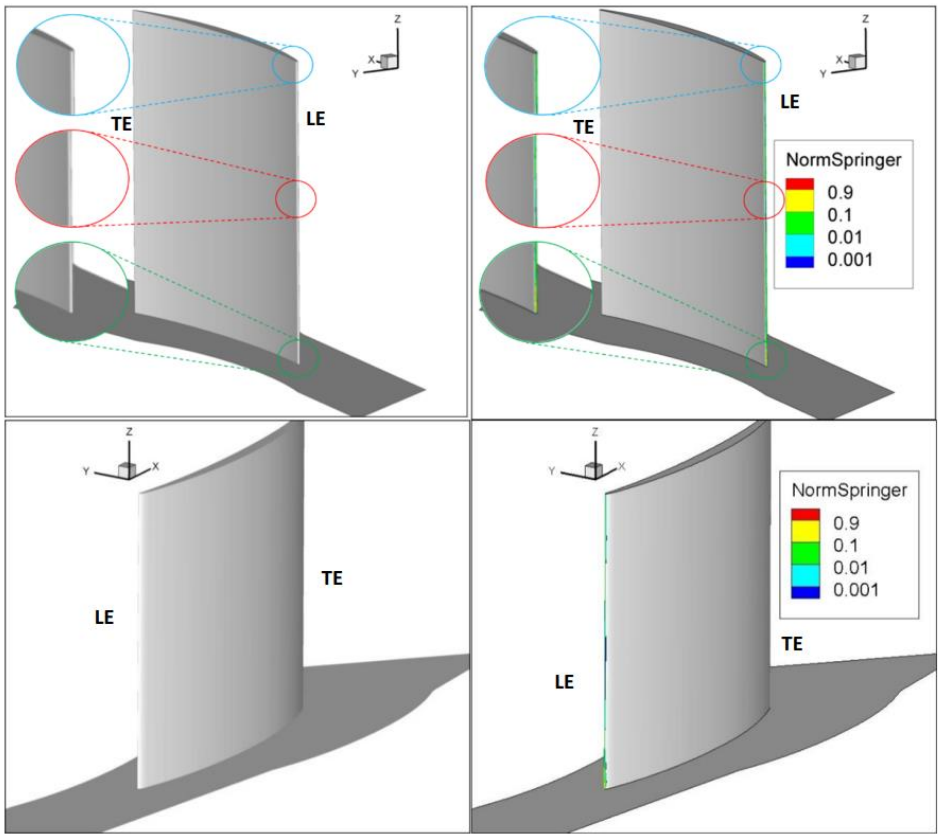

Figure 41: Normalized eroded material left: present model; right: Springer's model; top: PS; bottom: SS

The difference between the two models should be ascribed to the fact that the Springer et al. model was originally developed for predicting rain erosion on wind turbine blades (i.e., epoxy resins), and then generalized to other materials. This model was tuned for large droplets (1-7 mm), while in the case of water washing the droplets are much smaller, about 100-250 µm. Moreover, the present model accounts for surface hardness and roughness since they play a non-negligible role in the incubation period and erosion rate; the same quantities are not considered in the Springer et al. model. The difference between the two models is revealed in the computation of the incubation energy. In the present model this quantity is always at least 30 times larger than the accumulated energy, which means that erosion can occur only when injecting an unrealistically huge amount of water. On the contrary, in Springer et al. model the incubation energy is smaller and the accumulated energy overcomes it soon after some droplet impacts, leading to prediction of early erosion.

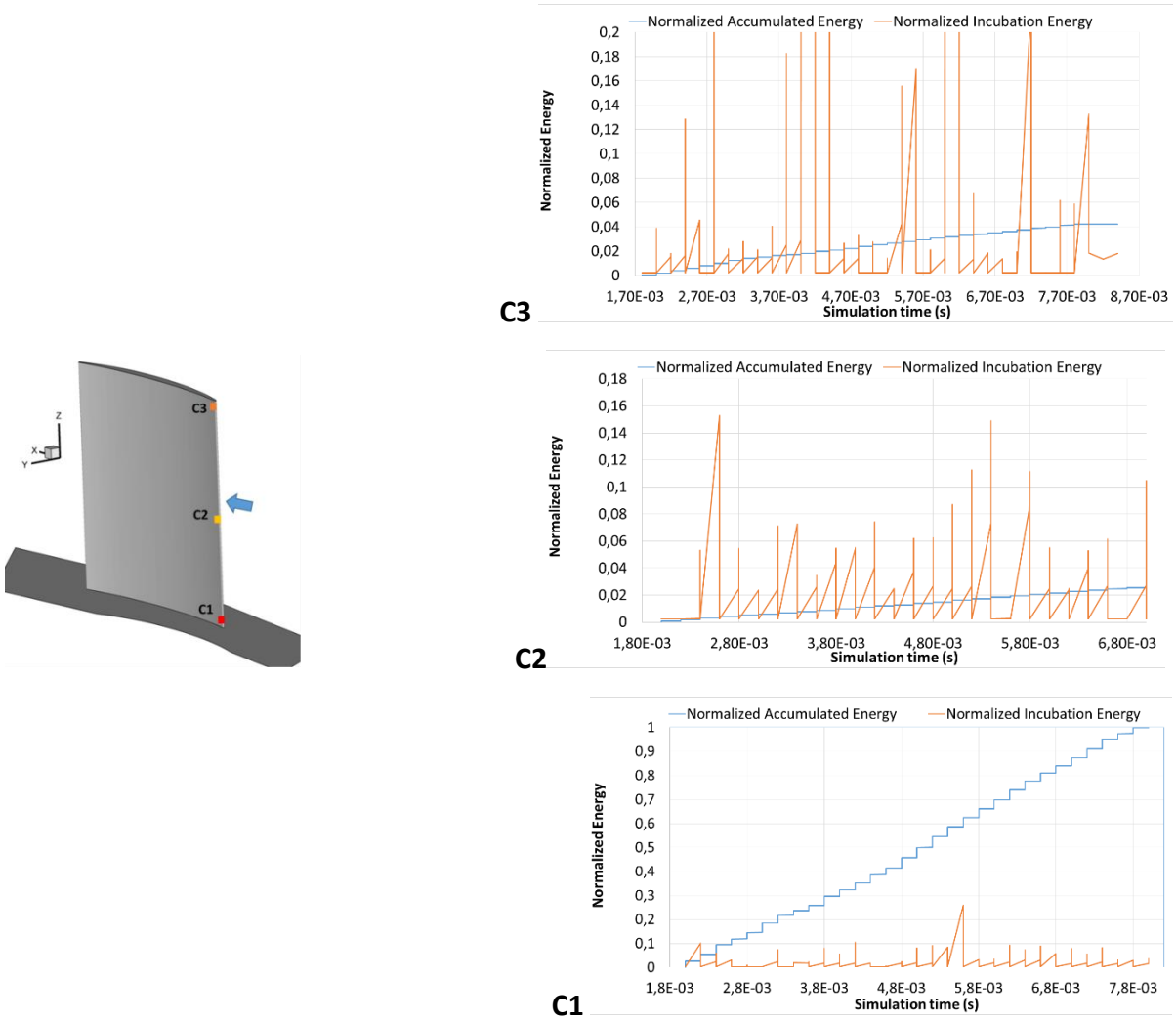

Figure 42: Normalized accumulated and incubation energy on the LE at the tip (C1, top), midspan (C2, middle) and root (C3, bottom)

In any case, the accumulated energy is larger at the bottom and smaller at the midspan; at the tip it is larger than at the midspan, but it does not reach the maximum. This is due to the particular blade configuration investigated. A stationary cascade has been simulated; thus, no centrifugal

and Coriolis effect are considered. Therefore, the peak in the accumulated energy is at the bottom part of the LE, close to the hub. Furthermore, there are some small horseshoe vortices entrapping droplets and pushing them toward the LE. In Figure 53 the normalized accumulated and incubation energy are shown at three different positions on the LE of the blade, namely at the root, at the midspan, and at the tip, as predicted by the Springer et al. model. As shown and as said above, the peak of erosion is predicted at the root of the blade (Figure 53 -C1). Here, the incubation energy is small, and a combination of the number of impacts and impact velocity leads to an increase of the accumulated energy, quickly overcoming the incubation energy; when it happens, erosion takes place. At the midspan (Figure 53 -C2), no relevant secondary motions form within the flow, thus droplet impacts are only due to their inertia. This results in a larger incubation period and then in a smaller erosion. On the contrary, at the tip the presence of the TLF increases the number of impacts on the blade and their velocity, leading to a reduction of the incubation period and then an increase of the erosion. A comparison with the erosion due to solid particle is also carried out. This simulation was performed to analyse the difference between the WDE and solid particle erosion models and consider the possibility of adopting the latter even for predicting erosion due to liquids. In this case, the simulation has been performed keeping constant the mass of injected particles, normalized by the maximum value of erosion. Results of this simulation are shown in Figure 54. In this case the erosion pattern is very similar to that of accumulated energy (Figure 39).

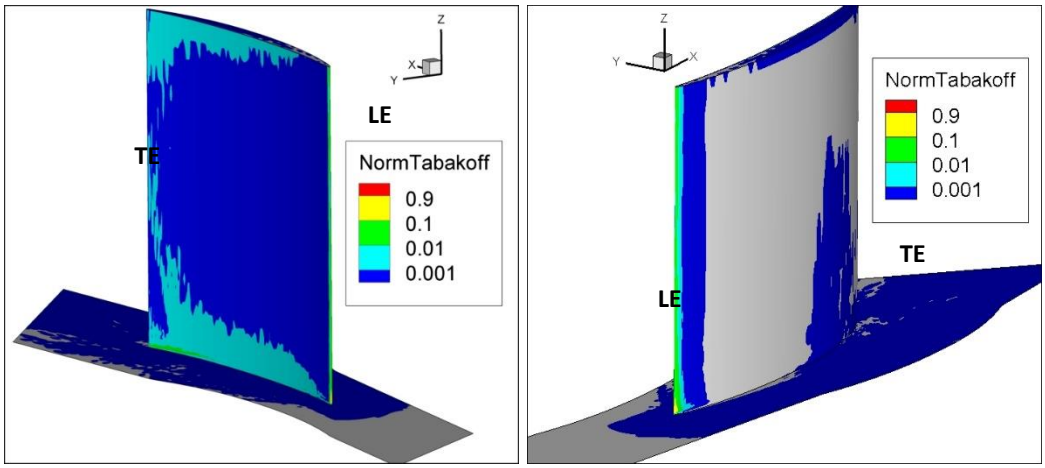

Figure 43: Normalized erosion due to solid particle impacts: pressure side (left), suction side (right).

The reason for this behaviour can be ascribed to the fact that particle erosion does not have any incubation period, and then at each impact material is eroded from the target surface. The only exception is the effect on the erosion rate of the impact angle, as in this case there is an angle of maximum erosion rate that, in the case of stainless steel, is about 30°. The results overpredict Water Droplets Erosion. This finding implies that modelling WDE using solid particle erosion models is incorrect and only qualitative results can be obtained when using the original Tabakoff et al. model [22].

Chapter 4

Sensitivity analysis of the main parameters affecting Water Efficiency

Reproduced in part from: F. Di Gruttola, G. Agati, P. Venturini, D. Borello, F. Rispoli, S. Gabriele, D. Simone, 2020, *Numerical study of erosion due to online water washing in axial flow compressors*, Proceedings of ASME Turbo Expo 2020, London, England (virtual conference), paper no. GT2020-14767.

In this chapter, a sensitivity analysis of the main parameters affecting the water washing efficiency is performed on a compressor-like geometry. The chapter is organized as follows: part 4.1 deals with the numerical models employed and explains how a User Define Function (UDF) has been used to implement the WDE model. In part 4.2 the configuration is investigated, and the simulation details are described. In part 4.3 the obtained results are discussed and reported.

4.1. Numerical models and computational approach

Simulations are performed using Ansys Fluent 19 [43]. To simulate both continuous and discrete phase the Discrete Phase approach is adopted, meaning that the flow field is computed in a Eulerian reference frame, while particles in a Lagrangian one. Moreover, since in the region close to the injector the particle concentration could be quite high, the two-way coupling approach is adopted [33] [36] meaning that mutual interaction between the two phases is accounted for.

The flow field is computed through RANS (Reynolds Averaged Navier Stokes) approach, whose second moment is modelled by the Realizable k-ε turbulence model [44], and the wall treatment adopts the Standard Wall Functions [45]. The RANS equation system is coupled with the energy equation to take in account small compressibility of the carrier fluid, treated as an ideal gas. Variations of gas density could be remarkable in the examined configuration resembling the geometry of a convergent/divergent duct. The Coupled Pressure-Based algorithm [43] is used to linearize and solve the discrete algebraic conservation equations.

Droplet dynamics is computed by solving the Newton's second law. Droplets dispersion and initial size distribution depend on the injection model adopted. In the present study, the cone injection approach [43] is selected since it better represents the real application. This approach offers the opportunity of modelling a real cone injector geometry without being mesh dependent, i.e. the

water droplets are not released from faces of the domain, but randomly from the outer diameter of the cone itself. Furthermore, the droplet diameters vary in a wide range because of the random and chaotic nature of the injection process. The cone injection allows setting the size distribution using the Rosin-Rammler distribution function. Rosin-Rammler is the most used expression to represent a diameter distribution and it is expressed as:

$$Y_d = e^{-\left(\frac{d}{d_m}\right)^n}$$

Where: Y_d is the mass fraction of drops having a diameter larger than d. The mean diameter d_m is equal to the value of d such that $Y_d = e^{-1}$. In other words, it is the value of diameter where the mass fraction is the 63.2% of the total one. The spread parameter n is a measure of the spread of drop size and provides a certain behavior of the curve. It assumes values lying in a range from 1.8 to 3.0 obtained by experimental data [46]. During the injection, drops are subject to both the drag (F_D) and surface tension (σ) forces. The first one has a disruptive effect on the liquid jet, which is converted into smaller and more irregular droplets. The second one forces the droplets to be spherical, since this shape has the minimum surface energy. When the drag force is greater than surface tension force, liquid breakups occur. To evaluate whether breakup occurs, the Weber number, defined as the ratio between drag and surface tension forces, is generally introduced. The critical condition for drop breakup happens when the two forces are equal. In the present study, the droplets and the flow characteristics do not lead to liquid break-up and for this reason such phenomenon will not be taken into account.

4.1.1. User-Defined Function for WDE simulation

The User-Defined Function (or UDF) is a C/C++ function here used to customize the erosion model in ANSYS Fluent. In the present study, this function is called when the particle impacts on a reflecting wall. Once it occurs, information about tracked particles (t_p), index of the face (f) where the particle impacts, mass of the particle (m), magnitude of the particle velocity (V_{mag}), normal unit vector (normal), impact angle (alpha) are passed to the UDF by ANSYS Fluent itself. These latter can be useful to quantify some output variables of the WDE model like: erosion rate, erosion, incubation and accumulated energy. At the end of the calculation, the values of interest are opportunely store in memory locations.

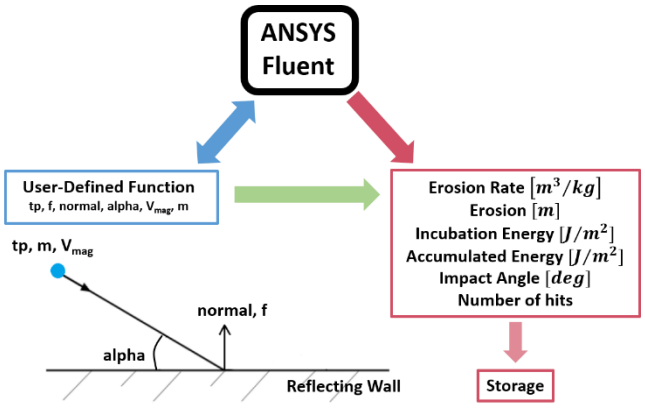

Figure 44. Schematic of the working principle of UDF implemented in Fluent to consider the WDE model presented in [39] ***and in*** [47]***.***

4.2. Simulation details

In the present section, some details about the performed simulations are described.

4.2.1. Numerical domain

The geometry considered (Figure 45) is a simplification of the compressor inlet up to the Inlet Guide Vanes (IGVs). This choice is justified by the interest in analysing the droplets distribution at the IGVs after the injection and the accelerating duct.

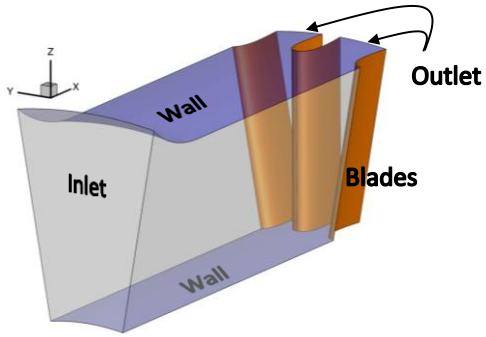

Figure 45. Numerical domain: blades (orange), walls (blue)

At the inlet, there is a bell-mouth, and then the upper and lower walls become parallel with a distance equal to 0.24 m. Close to the outlet section, the blade airfoils creates two convergent/divergent sections. The symmetric airfoils have a semi-elliptic shape with a 0.17 m chord length even if they are truncated at the middle of their extension. At the end of semi-elliptic region, the central blade has its maximum thickness of 0.034 m. The distance from inlet to outlet is equal to 0.6 m. The angular opening of the domain is 20°. The numerical domain is discretized with 410256 hexahedral cells (434010 nodes); cells close to the walls are refined presenting a 0.0014 m height. The mesh skewness ranges between 0.0039 and 0.786, and 1-11 as aspect ratio range.

The number of grid cells were selected by studying the y^+ quantity of a simple channel flow and exploiting the self-similarity of the velocity profile in turbulent boundary layers. The quantity y^+ is defined as $y^+ = u_\tau z/\nu$, where z is the distance from the wall, υ the kinematic viscosity and u_τ the friction velocity:

$$u_\tau = \frac{\sqrt{\mu \, {\partial u}/{\partial z}}}{\rho}$$

Assuming a Reynolds number (Re) for the fluid flow equal to 10^5, one can correlate this quantity with the friction Reynolds number (Reτ) according to [48]:

$$\mathrm{Re}_\tau = 0.09\ (2\mathrm{Re})^{0.88} = 4160$$

Starting from this expression, three values of y_w^+ (namely 50, 100, and 200) on the first cell row closest to the wall have been investigated. By writing the following proportion:

$$y_w^+ : y_{h/2}^+ = \Delta z : \frac{h}{2}$$

the heights of the cell adjacent to the wall (Δz) end up to be equal to 0.013, 0.025 and 0.05, respectively. Three different simulations of the channel flow were performed by varying the grid size at the wall. The log-law graph corresponding to the grid size with $y^+ = 100$ could reproduce the linear part of the curve and it was chosen since it represents the best compromise between accurate results and computational time. If the Reynolds number increases, i.e. $Re = 5 \cdot 10^5$, keeping the same value of $y^+ = 100$, the cells height decreases down to 0.00583 because of the thinner boundary layer. However, the linear part of the log-law is still respected, and this last result is applied to the present geometry. The generated grid is shown in Figure 46.

4.2.2. Boundary Conditions

At the inlet, a mass flow rate equal to 2.7 kg/s is imposed while at the outlet a pressure of 94000 Pa is set. Upper and lower walls are stationary walls with no slip condition, as well as the blades. Lateral walls are treated as periodic surfaces. As said above, droplets are injected within the domain adopting the cone injection model available in Ansys Fluent. The six droplet size classes reported in Table 9 have been assumed. The injector parameters are defined in

Figure ***47***; since they vary in each simulation, the assumptions made will be described time by time.

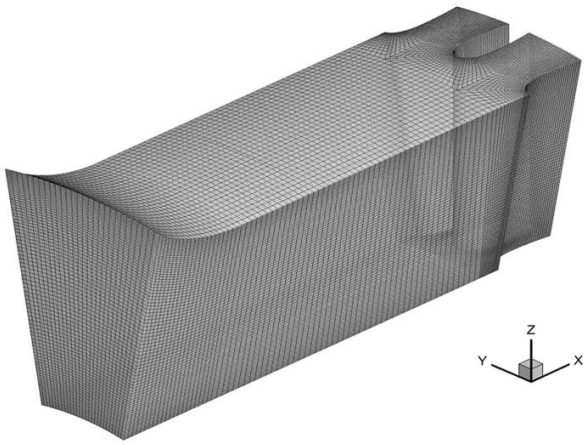

Figure 46. Grid of the numerical domain.

Table 9. Droplet size and mass fraction.

diameter (μm)	1.40	1.60	1.80	2.00	2.20	2.40
mass fraction	6%	9%	13%	18%	24%	31%

Liquid droplets can leave the computational domain through both inlet and outlet surfaces, and when they impact a wall. In the latter case, the User Defined Function developed by the authors computes the erosion rate on the wall according to the WDE model reported in [39] [47].

4.3. Results and discussions

For the present study, a series of simulations have been performed varying the main parameters affecting the WDE process on compressor blades. the following properties have been modified:

1. Injection duration
2. Droplet size
3. Spray angle
4. Injection velocity
5. Injector position

In all the simulations, apart from those at point 4, the injector position is the one sketched in Figure ***48***. Before presenting and discussing the results provided by the simulations, it is helpful to define the quantities that have been presented. Normalized Accumulated energy ($E_{acc,norm}$). As described in [39] [47] and recalled in the Introduction section, during the incubation period the impact energy of the droplets is accumulated on the target surface until it overcomes a threshold value (namely, the incubation energy). To make it independent from the number of injected droplets, the result of each simulation is normalized with its maximum.

Normalized Erosion (E_{norm}). Once the accumulated energy overcomes the incubation energy threshold, erosion takes place. Therefore, at each impact it is possible to compute the erosion rate and the material removed from the target surface. By dividing this quantity by the target material density, one can readily evaluate the thickness of the removed material. Even in this case, to make the results independent from the number of injected droplets, the result of each simulation is normalized with a reference value, specified case by case.

Wetted surface (WS). Wetted surface is the surface of the blades affected by droplets impacts. It is expressed as percentage of the blade surface.

Capture efficiency (CE). This quantity is the ratio (expressed as percentage) between the number of droplets impacting the blades, and that of the injected droplets. Some of these quantities are reported along some specific lines. In this case, the blade span is normalized (z*) with its maximum.

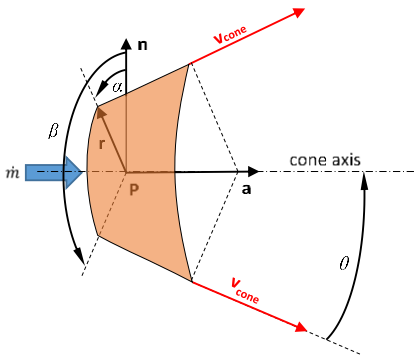

Figure 47. Sketch of a sector of the injection cone, and its main parameters.

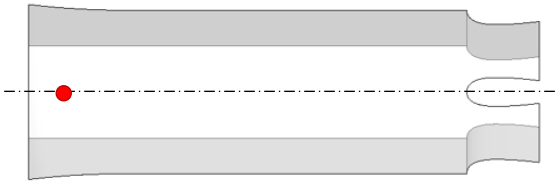

Figure 48. Reference position of the injector (red dot).

All these parameters together, may provide useful indications about how good is a certain water washing configuration, in terms of the capability of removing dirt from the blades, and how dangerous it is in terms of erosion, which is the real information industrially relevant. In the following subsections, the results obtained are presented and discussed.

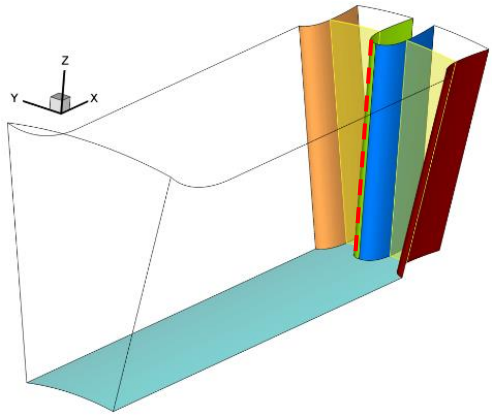

Figure 49. Surfaces and lines on which the results are shown: blade1 (red surface), blade2 (blue surface), blade3 (green surface), blade4 (orange surface), lower surface (light blue); leading edge of the central blade (red dashed line), throats (intersection of the yellow plane with the blade surfaces).

Table 10. Injection parameters assumed for studying the effect of different injection duration on erosion.

$r\ (m)$	0.00065
$\theta\ (°)$	60
$\alpha\ (°)$	0
$\beta\ (°)$	360

$injection\ time\ (time\ steps)$	10, 50, 100
$P\ \ (m)$	(0.065; 0; 0.56)
$\vec{a}\ \ (m)$	(-0.32; 0; -0.95)
$\dot{m}\ \ (kg/s)$	0.046
$v_{cone}\ (m/s)$	34.7
$droplet\ size\ (\mu m)$	140, 160, 180, 200, 220, 240 (polydisperse)

4.3.1. Injection duration

The influence of injection duration was studied by performing three different simulations, having an injection duration equal to 10, 50 and 100 time steps, being a time step equal to 5·10-5 s. The injector is positioned on the upper wall, along its intersection with the symmetry plane as in Figure ***48***. The injection parameters assumed in these cases are reported in Table 10. Figure 50 shows the accumulated energy (left column) and erosion (right column) both normalized by the respective maxima. Most of the impact energy is accumulated at the leading edges of the blades, in all the cases, but with a larger accumulation close to the blade root. This is related the specific investigated geometry, in particular to the aspect ratio.

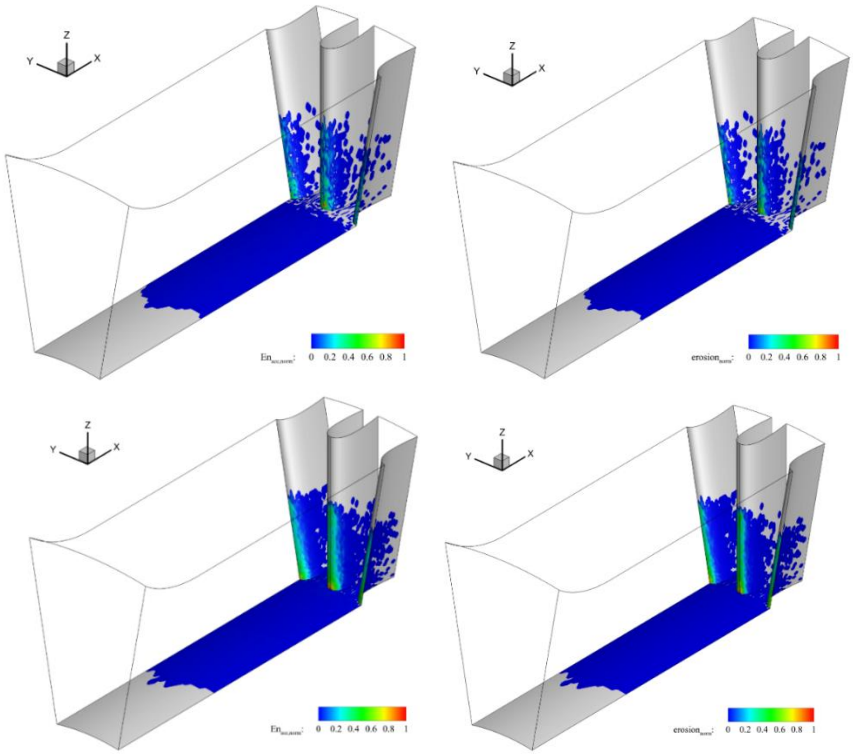

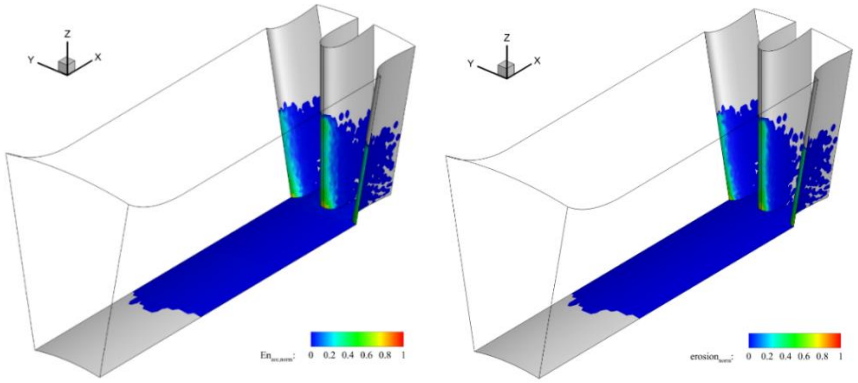

Figure 50. Normalized Accumulated Energy (left) and Erosion (right) using different injection duration: 5·10-4 s (top), 1·10-3 s (middle), 5·10-3 s (bottom)

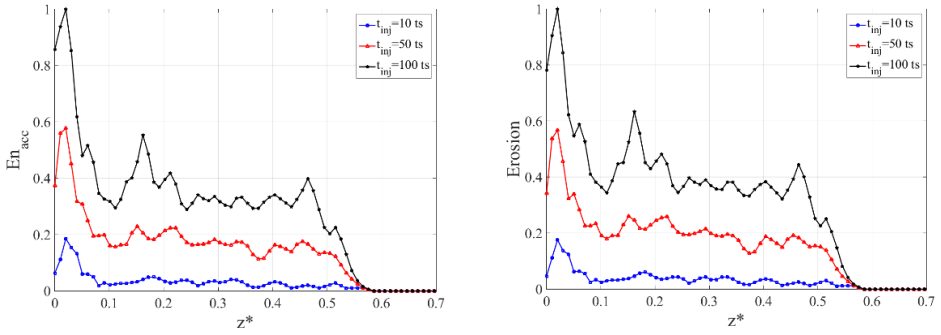

Figure 51. Normalized accumulated energy (left) and erosion (right) at the leading edge of the central blade.

However, some more general considerations can be done. In particular, the blade regions (in blade1-blade4) affected by droplets impacts increase with the injection duration, tending to an asymptotic value. Indeed, the wetted surface in the cases of 10 time step (Figure 50-left-top) is quite different (especially the blades) to those at 50 and 100 time steps (Figure 50-left-middle and -bottom), which on the contrary are very similar. This is related to the number of injected droplets: when the injection time is very short, the number of droplets is not large enough to provide statistically relevant results. As the injection time increases, the number of droplets increases accordingly, and the results become more relevant from a statistical point of view. This effect reduces as the injections time increases. Quantitatively this is measured by the WS and CE percentages (Table 11) both defined above. The Average WS grows 12% when going from 10 to 50 injection time steps, but only 3% going from 50 to 100 injection time steps. The same can be said for each blade portion. WS of the lower wall varies in a narrower range (60-67 %) in all the cases. The CE increases from 8% in the case of 10 injection time steps, to 29% for 50 and 100 injection time steps, reaching what seems a stationary value. Figure 51 focuses the attention on the leading edge of the central blade (composed of surfaces Blade2 and Blade3). In the figure, the accumulated energy and the erosion are normalized by the maximum reached at the leading edge among the three simulations. This gives us an idea of the erosive potential of the sprays. As shown, both the depicted quantities increase with time, putting in evidence the presence of some peaks in the case of a longer injection time is adopted. What is worth noting is that the general shape of the erosion is the same (droplets reach about 60% of the blade span, showing a peak close to the hub) but the more droplets are injected, the more accurate is the prediction. According to this result, in all the other simulations an injection time equal to 50 time steps has been adopted, considering it a good compromise between accuracy and computation time.

4.3.2. **Droplets size**

Another set of simulations was dedicated to studying the effect droplet size. Three droplet size classes have been separately simulated, namely 140, 190 and 240 μm. The other injection parameters are summarized in Table 12.

Table 11. Wetted surface (WS) and capture efficiency (CE) on the blades and lower wall, varying the injection time

No. of injection time steps	10		50		100	
	WS	CE	WS	CE	WS	CE
Blade1	24%	7%	41%	7%	46%	7%
Blade2	27%	8%	43%	7%	48%	7%
Blade3	27%	8%	43%	7%	48%	7%
Blade4	24%	7%	41%	7%	46%	7%
Lower wall	60%	50%	66%	51%	67%	51%
Average	40%	79%	52%	79%	55%	79%

Table 12. Injection parameters assumed for studying the effect of droplet size on erosion.

$r\ (m)$	0.00065
θ (°)	60
α (°)	0
β (°)	360
$injection\ time(s)$	50
$P\ \ (m)$	(0.065; 0; 0.56)
$\vec{a}\ \ (m)$	(-0.32; 0; -0.95)
$\dot{m}\ \ (kg/s)$	0.046
$v_{cone}\ (m/s)$	34.7
$droplet\ size\ (\mu m)$	140, 190, 240 (monodisperse)

In Figure 52 the position of droplets having different size have been reported, just after injection. Although the Stokes number of such droplets is very large, ranging in 13.3-39.1, smaller droplets still react quickly to the flow field, thus remaining more grouped than the larger ones, and positioned further on and up in the numerical domain. This will influence the wetted regions and erosion.

Figure ***53*** shows the normalized erosion for these simulations. Smaller droplets mostly impact the blades, covering a larger span. Since they are grouped and move about the middle of the channel, a very small amount of them impacts the lower surface. As the droplet size increases, the region affected by impacts moves downward the blades, and lower wall becomes more and more wetted. Table 13 reports WS and CE for this series of simulations. The average WS increases with the droplet size, ranging from 23% (smaller droplets) to 49% (larger ones). It is interesting to note that the lower wall is the most wetted surface, apart from the smaller droplet case, in which it represents the least one. The CE follows the same trend. As for the normalized erosion, it can be underlined that as the size increases the erosion peak moves toward the root of the blades, and for 240 µm droplets it almost disappears, because a large portion of impacts involves the lower wall.

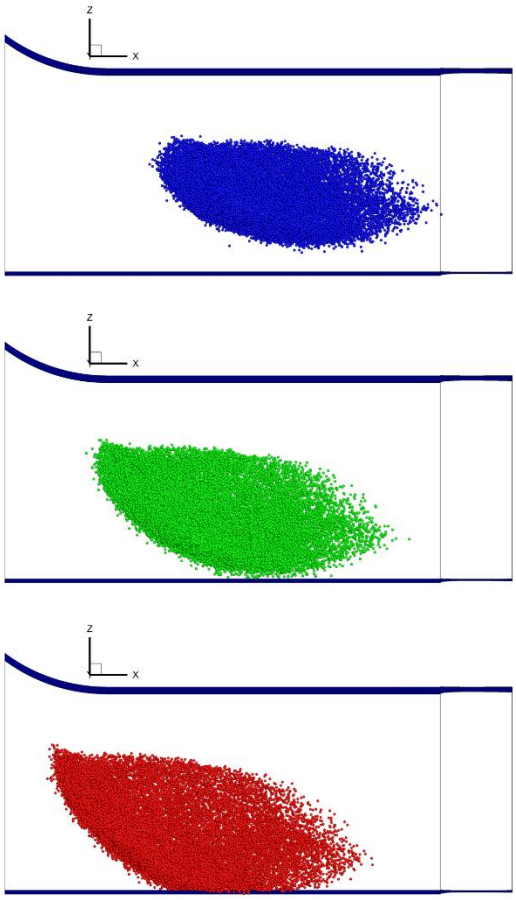

Figure 52. Droplet position at the same time instant: 140 µm (blue), 190 µm (green), 240 µm (red).

4.3.3. **Spray angle**

The semi-opening angle of the injection cone (θ in

Figure 47) is a parameter that can be modified by appropriately designing the injector. In the present simulation campaign, the effect of cone angle on WDE process by simulating four different semi-opening angles, namely 30°, 45°, 60° and 80° has been studied. All the main injection parameters for this series of simulations are reported in Table 14.

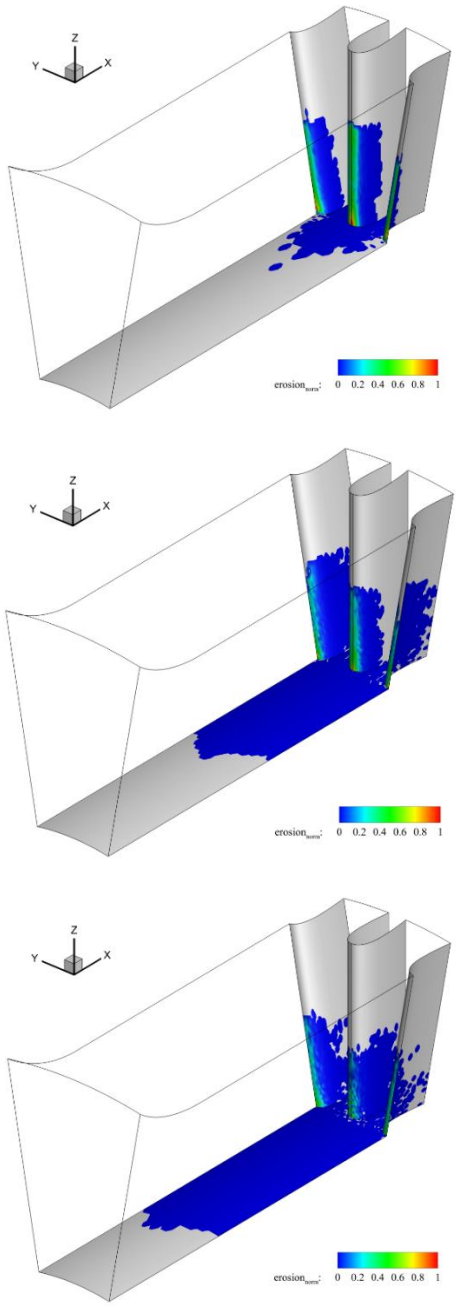

ù

Figure 53. Normalized Accumulated Energy for different droplet sizes: 140 µm (top), 190 µm (middle), 240 µm (bottom).

The variation of the injection angle reflects on the impacted surface (Figure 54). Figure 55 depicts the normalized accumulated energy (top) and erosion (bottom) varying the injection angle, at the leading edge of the central blade. As the injection angle increases the average wetted surface increases accordingly. While the wetted surface of the lower wall is about constant in all the simulations (see also Table 15), that of the blades varies largely, going from 9% up to 65%. Indeed, as the injection angle increases, the spray becomes wider, and the vertical velocity of droplets decreases. Therefore, the wetted surface of the lower wall slowly decreases accordingly, while and droplets impact the blade on a higher span (Figure 55), reaching about 80% of the blade span in the case of 80° injection angle.

Table 13. Wetted surface (WS) and capture efficiency (CE) on the blades and lower wall, varying the droplet size.

Droplet size(μm)	140		190		240	
	WS	CE	WS	CE	WS	CE
Blade1	21%	11%	48%	7%	31%	4%
Blade2	30%	14%	25%	5%	45%	5%
Blade3	30%	14%	25%	5%	45%	5%
Blade4	21%	11%	48%	7%	31%	4%
Lower wall	19%	15%	51%	58%	66%	71%
Average	23%	64%	42%	83%	49%	88%

Table 14. Injection parameters assumed for studying the effect of the semi-opening angle of the injection cone.

$r\ (m)$	0.00065
$\theta\ (°)$	30, 45, 60, 80
$\alpha\ (°)$	0
$\beta\ (°)$	360
$injection\ time(s)$	50
$P\ \ (m)$	(0.065; 0; 0.56)
$\vec{a}\ \ (m)$	(-0.32; 0; -0.95)
$\dot{m}\ \ (kg/s)$	0.046
$v_{cone}\ (m/s)$	34.7
$droplet\ size\ (\mu m)$	140, 160, 180, 200, 220, 240 (polydisperse)

4.3.4. Injection velocity

Injection velocity is another parameter that can be controlled by a proper design of the injector. In the present work the effect of the injection velocity ranging in 20-50 m/s has been analysed. The injection parameters are summarized in Table 16. Droplets injected with a smaller velocity are quickly entrained by the flow, thus they mostly impact the blades. This is shown in Figure 56, where very few droplets impact the lower wall. Increasing the injection velocity leads to an increase of the fraction impacting the lower wall, and a reduction of that impacting the blades. Focusing the attention to the leading edge of the central blade Figure 57, what said above is more evident: 20 m/s injection leads to a large accumulated energy and erosion at about the midspan of the blade, even larger than that due to 35 m/s. In the case of 50 m/s injection, most of the droplets impact the lower wall, thus the erosion of the leading edge is the smallest of the three cases. This trend is also confirmed by the WS and CE in Table 17.

4.3.5. Injection position

Two different injection positions were investigated: the central position is the standard one, and the second is shifted along the spanwise direction as shown in Figure 58.The whole set of the injection parameters are reported in Table 18. From the contour plots presented in Figure 59 it is possible to observe that when the injection is not central the maximum of the accumulated energy is no longer positioned on the leading edge of the central blade but it is now located on the hub region of the lateral blades (blade 1 and blade 4). This is due to the fact that in this case the injection is not anymore symmetric with respect to the stagnation point of the central blade. The same trend can also be seen in the profiles presented in Figure 60. This behavior is slightly reflected in the erosion contour plots. In fact, the droplets impact conditions on the lateral blades are characterized by a lower normal component of velocity (this being one of the main parameters affecting erosion). The same behavior can be observed also in the values of the WS reported in Table 19.

In comparison with the central injection, the blade 3 is the only one that experiences a higher value of the WS. This is because most of the injected droplets exit from the lateral periodic surface, impacting the central left blade (namely the blade 3). On the contrary, blade 2 and blade 4 present a lower wetted surface being hidden with respect to the left periodic surface where most of the droplets come from. Capture efficiency almost do not change in the two cases.

4.3.6. Results discussion

In previous paragraphs, a systematic numerical analysis of the parameters mostly influencing the water washing process has been presented. From the simulations it comes out that the injection time, injection angle and injection velocity are the parameters mostly affecting the washing efficiency. The injector position can be optimized to better distribute the water droplets on the

blade surface. Last, the droplet size distribution produced by the injection system affects the region of the blade reached by the water, thus it may help in increasing the washing efficiency.

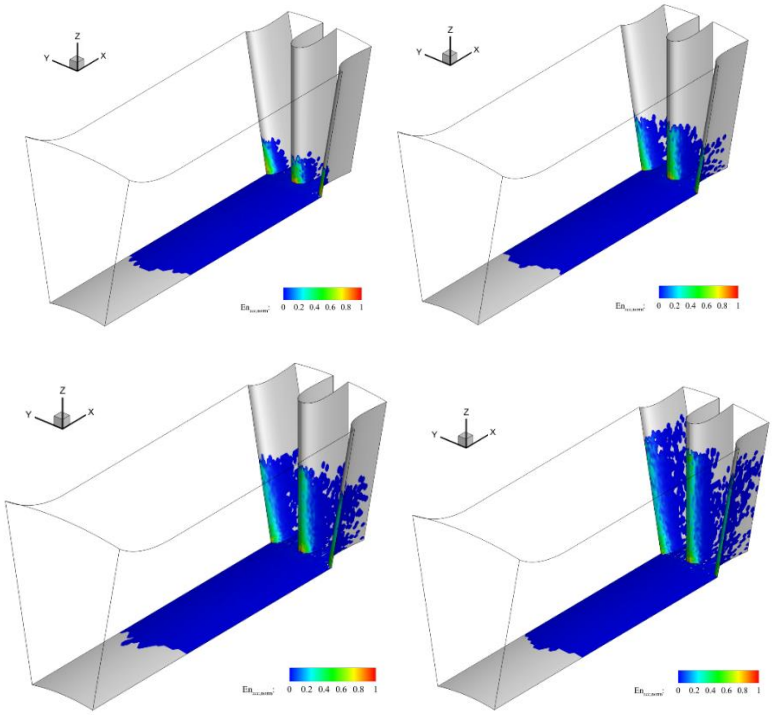

Figure 54. Normalized Accumulated Energy for different semi-opening angle of the injection cone: 30° (a), 45° (b), 60° (c), 80° (d)

Table 15. Wetted surface (WS) and capture efficiency (CE) on the blades and lower wall, varying the semi-opening angle of the injection cone

Injection angle	30°		45°		60°		80°	
	WS	CE	WS	CE	WS	CE	WS	CE
Blade1	9%	3%	22%	5%	41%	7%	65%	8%
Blade2	9%	2%	25%	5%	43%	7%	57%	9%
Blade3	9%	2%	25%	5%	43%	7%	57%	9%
Blade4	9%	3%	22%	5%	41%	7%	65%	8%
Lower wall	67%	84%	67%	66%	66%	51%	66%	38%
Average	33%	95%	41%	87%	52%	79%	63%	71%

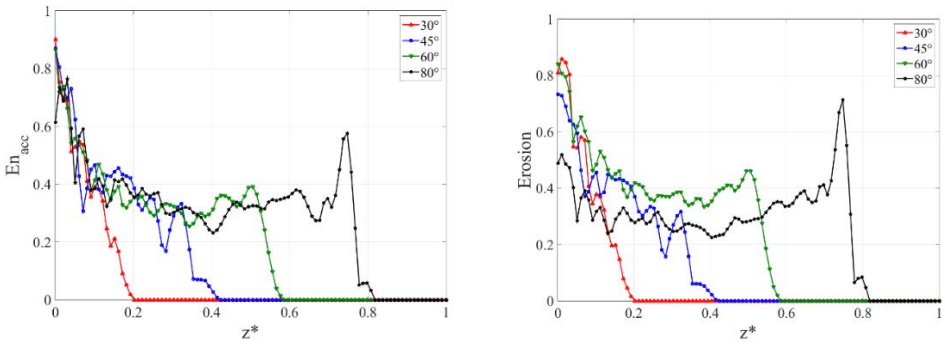

Figure 55. Normalized accumulated energy (left) and erosion (right) at different semi-opening injection angles: 30° (red), 45° (blue), 60° (green), 80° (black)

Table 16. Injection parameters assumed for studying the effect of the injection velocity

$r\ (m)$	0.00065
$\theta\ (°)$	60
$\alpha\ (°)$	0
$\beta\ (°)$	360
$injection\ time(s)$	50
$P\ \ (m)$	(0.065; 0; 0.56)
$\vec{a}\ \ (m)$	(-0.32; 0; -0.95)
$\dot{m}\ \ (kg/s)$	0.046
$v_{cone}\ (m/s)$	20.0, 34.7, 50.0
$droplet\ size\ (\mu m)$	140, 160, 180, 200, 220, 240 (polydisperse)

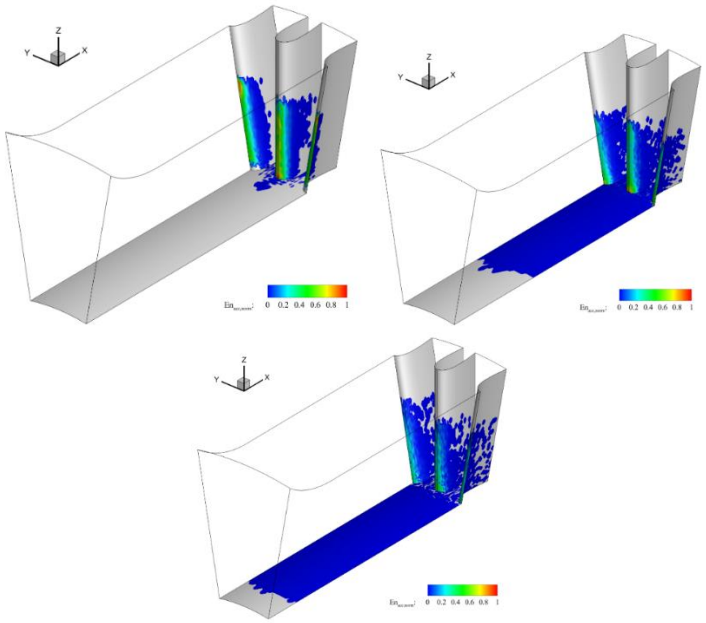

Figure 56. Normalized Accumulated Energy using different injection velocity: 20 m/s (left), 35 m/s (middle), 50 m/s (right)

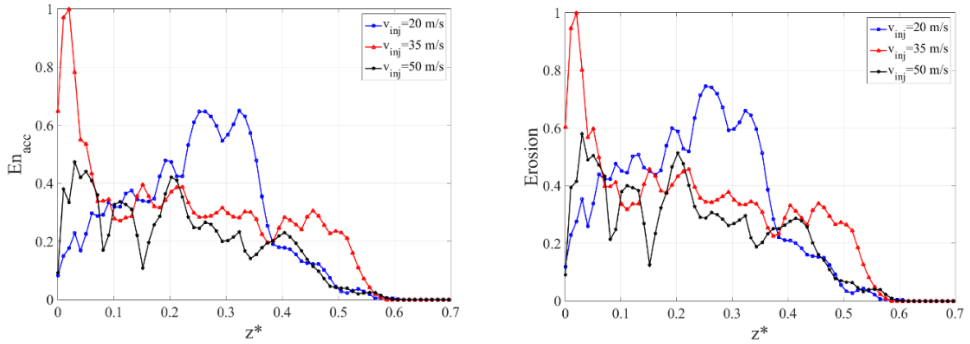

Figure 57. Normalized accumulated energy (left) and erosion (right) at different injection velocities: 20 m/s (blue), 35 m/s (red), 50 m/s (black)

Table 17. Wetted surface (WS) and capture efficiency (CE) on the blades and lower wall by varying the injection velocity

Injection velocity	20 m/s		35 m/s		50 m/s	
	WS	CE	WS	CE	WS	CE
blade1	27%	12%	41%	7%	49%	5%
blade2	33%	13%	43%	7%	43%	4%
blade3	27%	13%	43%	7%	43%	4%
blade4	33%	12%	41%	7%	49%	5%
lower wall	6%	2%	66%	51%	85%	69%
Average	21%	52%	52%	79%	62%	86%

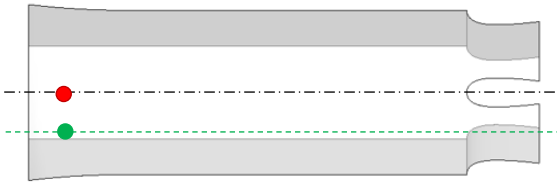

Figure 58. Reference (red dot) and shifted (green dot) positions of the injector

Table 18. Injection parameters assumed for studying the effect of the injection position

$r\ (m)$	0.00065
θ (°)	60
α (°)	0
β (°)	360
$injection\ time(s)$	50
$P\ \ (m)$	(0.065; 0.0; 0.56) (0.065; -0.048; 0.55)
$\vec{a}\ \ (m)$	(-0.32; 0; -0.95)
$\dot{m}\ \ (kg/s)$	0.046
$v_{cone}\ (m/s)$	20.0, 34.7, 50.0
$droplet\ size\ (\mu m)$	140, 160, 180, 200, 220, 240 (polydisperse)

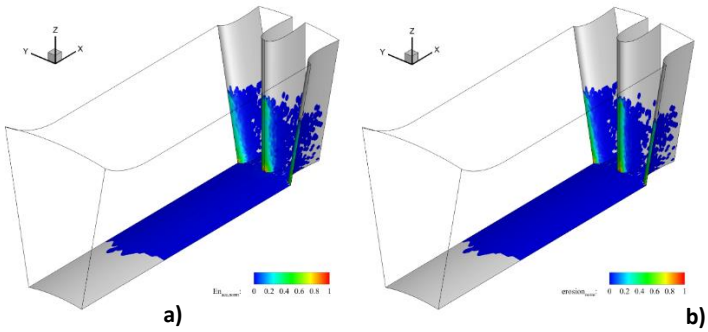

a) **b)**

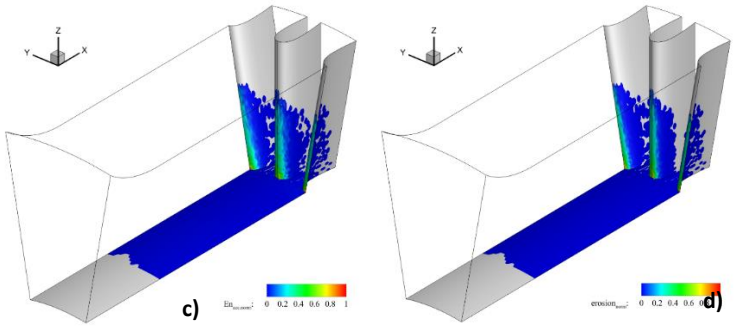

Figure 59. Normalized Accumulated Energy (left) and Erosion (right) for different injection position: central injector (top) and shifted injector (bottom)

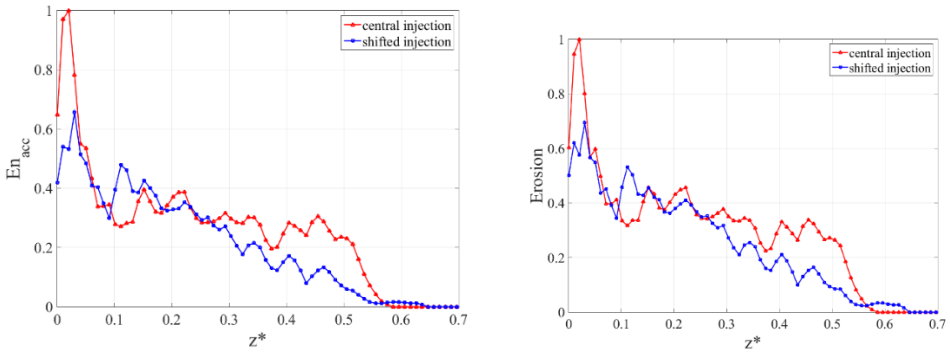

Figure 60. Normalized accumulated energy (left) and erosion (right) for different injection positions

Table 19. Wetted surface (WS) and capture efficiency (CE) on the blades and lower wall by varying the injection position

Injection Position	Central		Shifted	
	WS	CE	WS	CE
Blade1	41%	7%	38%	7%
Blade2	43%	7%	31%	6%
Blade3	43%	7%	47%	7%
Blade4	41%	7%	36%	7%
Lower wall	66%	51%	67%	52%
Average	52%	79%	50%	79%

Chapter 5

Numerical analysis of water injection in LT16 Gas Turbine AXCO

Reproduced in part from: Agati, G., Di Gruttola, F., Gabriele, S., Simone, D., Venturini, P., Borello, D. *Water washing of axial flow compressors: numerical study on the fate of injected droplets*, ATI, 2020.

In this chapter, the new WDE model is used to study the droplet fate (impact, splashing, generation of liquid film) during both off-line and on-line water injection. Some indexes are introduced to quickly visualize indications about the effect of the injection system and the washing process on each part of the machine, focusing the attention on the rotor stage that is the most exposed to the risk of erosion. In this first step the influence of geometry modification due to the erosion is not taken in account.

5.1. Models and computational approach

The study reproduces the flow in the inlet section of an LT16 axial compressor, considering inlet region, struts, Inlet Guide Vanes (IGV) and the first rotor. Two configurations are considered: non-rotating and rotating rotor. Such configurations are representative of the off-line and on-line water washing respectively. The simulations are carried out by using Ansys Fluent. The study of a multi-phase flow was based on a Eulerian-Lagrangian one-way coupling approach. The turbulent field is modelled by using Unsteady (U)-RANS employing the well-established, widely accepted k-ε realizable model. Standard wall-function is used for the near-wall treatment. The SIMPLEC scheme has been selected for the pressure-velocity coupling. Spatial discretization for the pressure term has been achieved by a second order upwind scheme while for all the other variables a first order scheme is adopted.

For all the simulations here investigated, firstly the stationary fluid flow has been solved until the solution reached the convergence by imposing the maximum accepted residual down to 1e-05 for the continuity equation, 1e-06 for the energy one and a value of 1e-03 for the k and ε equations. The static simulation took 5282 iterations to converge, while the rotating one, that has been initialized with the converged solution of the static simulation, needed 4640 more

timesteps to reach the convergence. After that, transient simulations have been run where the droplets injected were tracked until all of them reached their final destination, i.e. either they exit the domain or they impact one of the solid surfaces. In the transient simulations a timestep dt=3e-05 is adopted for the fluid flow while the integration of droplets motion is achieved by an automated tracking scheme that permits to switch between a numerically stable implicit lower order scheme and a trapezoidal higher order one. Moreover, the accuracy control option permits the solution of droplets motion equation to be within a tolerance of 1e-05.

In the rotating simulation, the Frozen Rotor approach (i.e. the Multiple Reference Frame Model) is adopted. The rotor cell zone (rotating with an angular velocity ω=7800 rpm with respect to the negative x-axis) is solved in the relative reference frame [43]. Because of the high rotation speed, the flow solution is less stable and, to guarantee the reaching of convergent solution, the angular velocity has been increased gradually starting from the non-rotating solution. Initially, an angular velocity ω= -4800 rpm has been firstly imposed to the rotor cell zone and only after this solution converged, rotational speed has been increased up to the desired value.

The fate of the injected droplets depends on the outcome of their possible impact on the solid walls. Ansys Fluent has a specific boundary condition the Stanton-Rutland model [49] to deal with droplets collision with solid surfaces based on impact conditions. The model distinguishes 4 different impact regimes, depending on the local wall temperature and on the impact energy. Here it is worth to mention that in this model the fate of an impacting droplet can be: sticking, spreading, splashing or rebounding as illustrated in Figure 61.

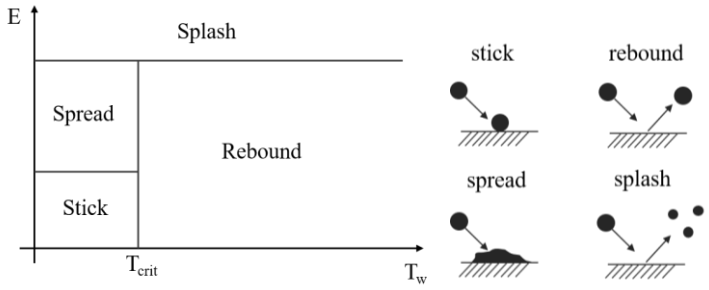

Figure 61. Different droplet impact regimes identified by the adopted model [36]

A droplet rebound can happen only when the wall temperature is above a critical value that is linked to the saturation temperature of the liquid droplet. In the present configuration, wall temperature is always lower that the T_{crit}, hence droplets can only stick, spread or splash depending on the energy of the impact. Splashing occurs when the impacting energy exceeds a threshold value. This value corresponds to the splashing criteria identified by Yarin and Weiss [50] for a train of impinging droplets. If a droplet impact results in a splashing, then secondary smaller droplets are generated. The obtained secondary droplet diameters are sampled by a cumulative probability Weibull distribution function that was fitted to the experimental data from Mundo et al. [51]. Together with the impact model, when a droplet impacts a surface, an User Defined Function (UDF), introduced and explained in [52] becomes active. The UDF contains the erosion model developed in previous chapter [47], and here it is extended to access several

information useful to study the major aspects that are relevant in the present case of study. A droplet impact, regardless of its outcome (deposit, spread, splash), accumulates energy on the impacted surface, eventually provoking erosion. If the impact energy is low, the droplet will also deposit on the surface creating a liquid film. On the other side, if the energy is strong enough to overcome the splashing threshold, the droplet will rebound forming secondary smaller droplets that may impact and erode other solid surfaces. The UDF was however implemented to extrapolate some quantitative parameters useful to assess the effectiveness of the washing strategy and to evaluate the associated erosion risk.

5.2. Simulation details

5.2.1. Numerical domain and computational mesh

The numerical domain consists of an inlet volume, 7 struts before entering the compressor, then 36 inlet guide vanes (IGVs), and then 18 blades of the first rotor stage as shown in Figure 62.

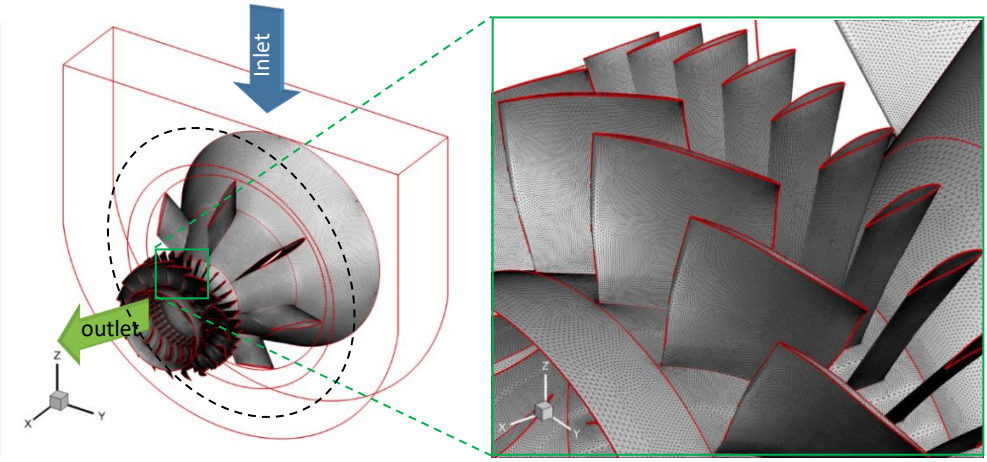

Figure 62. Numerical domain (left) and zoom-in of the first rotor stage (right); dark dashed line: line of injector positions.

Such a configuration is typical of axial compressors used in gas turbine engines. The compressor inlet section, from which air enters the domain, is a rectangular region at the top of the domain (blue arrow in figure), while the outlet is the annulus section positioned in the yz plane after the compressor rotor (green arrow in figure). Water is injected in the domain through 14 injectors distributed along the dark dashed line in Figure 62-left, upstream of the struts. Water droplets mix with air along the passage, but the mixing is not uniform or homogeneous. Due to this non-uniformity, the non-commensurable ratio among struts, IGV and rotor blades as well as the geometry of rotor, it was not possible to assume periodicity or symmetry conditions. So all the geometry must be simulated in this analysis.

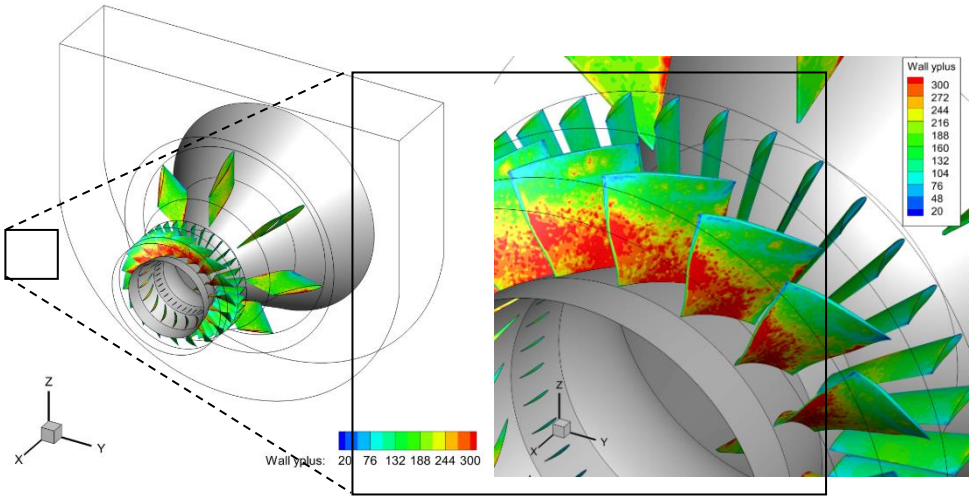

Figure 63. Values of the y+ on some of the domain walls (right); zoom-in of the first rotor stage (right).

The computational domain is discretized by using about 25.5 M tetrahedral cells, clustered close to the walls to have a mesh refinement sufficient to guarantee that the first stripe of cells close to the wall has y+ values ranging between 20-300 (as shown in Figure 63). Such range represents the interval of applicability of the adopted wall function.

5.2.2. Boundary conditions

The air flow enters the inlet section (blue surface in Figure 64 with a mass flow rate equal to 53.7 kg/s and exits from the outlet section where a calculated pressure value is imposed. The other surfaces are all treated as no slip stationary walls. In rotating configuration, downstream from the Frozen Rotor surface, no-slip BCs are imposed on the rotor blades and hub walls in the relative frame of reference while the casing was considered as a rotating wall with an angular velocity ω=7800 rpm. While at the inlet section a mass flow inlet boundary condition is used, a pressure outlet is used to fix the conditions the air exits the domain (green surface in Figure 64). Outlet conditions differ between the static and the rotating simulation. For the fixed rotor simulation, atmospheric pressure is set at the outlet domain section. In the rotating case the exit pressure (P2) was calculated from the Eulerian work exerted by the rotor to the fluid and compared with the industrial design value. The resulting value was set as pressure BC.

The droplets are injected by 14 solid cone injectors all around the circular section upstream of the struts (Figure 62). According to [39], [47] the solid cone injector releases droplets from a circular section (1.2 mm diameter) and having a 57° half-opening cone angle. The water mass flow rate is assumed about 12 g/s, which corresponds to a velocity magnitude of 10.5 m/s. In real water injection injectors the droplet size distribution covers a continuous range of diameters between 140-240µm whose characteristics depends on type of injector, injection pressure, inlet flow velocity, and water-to-air ratio. A Rosin-Rammler distribution function has been assumed with an average diameter of 198µm and grouped the droplets in 6 class of sizes.

Droplets may escape from the numerical domain through both inlet and outlet sections. However, if a droplet impacts a wall it may splash generating secondary smaller droplets according to the model explained previously and a liquid film may form on the impacted surface.

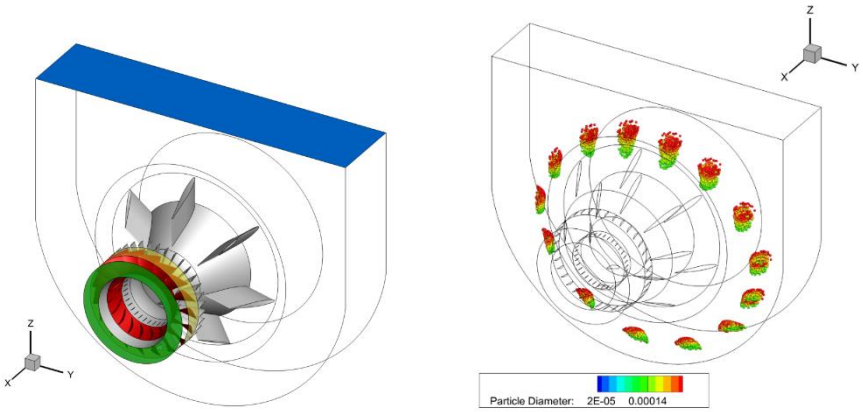

Figure 64. Boundary conditions. Left: inlet (blue), outlet (green), rotor inlet (yellow), rotating components (red). Right: injector positions and droplets coloured by their size.

5.2.3. Performed simulations

Two simulations reproducing the off-line and on-line WW processes of the first stage of typical a compressor used in gas turbine engines are carried out. Off-line water washing is performed periodically and involves the turbine shutting down and then the injection of properly nebulized water for 20-30 minutes. The turbine is put on idle, but its speed is extremely smaller than the design one (usually less than 20%). On the contrary, on-line WW is performed when the engine is at nominal load. Therefore, for simulating the off-line WW condition it has been assumed that the turbine is shut down, while for on-line one it is running at its nominal rotational speed. For each of these conditions water is injected within the domain trough the injectors. The flow field analysis supports the study of droplets/walls interaction with the aim of computing WDE in the two cases.

5.3. Results and Discussion

The relevant outcomes are presented in the following paragraphs.

5.3.1. Flow field

Flow field at the inlet of the machine is symmetric with respect to the z axis. In Figure 65, the fluid flow streamlines coloured with the velocity magnitude are reported in the non-rotating (left) and in the rotating (right) case. In both cases, the flow field is similar in the inlet vane, across the struts and up to the IGV. However, when focusing on the rotor zone it can be seen that in the not

rotating case, the fluid is accelerated because of the reduction of the passage section exiting the rotor. As for the rotation case, Figure 65 right, the streamlines of the rotating case are plotted in the absolute reference frame. The work delivered to the fluid through the shaft rotation is responsible of the increase in pressure more than flow acceleration.

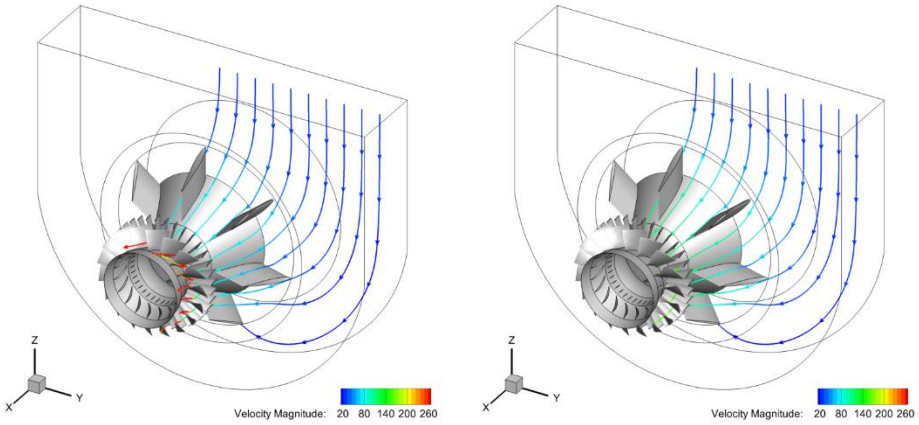

Figure 65. Streamlines coloured with velocity magnitude in the non-rotating (left) and rotating (right) simulations.

A more representative view of the fluid streamlines crossing a rotor vain is presented in Figure 66 for both the not rotating (left) and the rotating simulation (right). As previously seen, in the non-rotating case, the fluid is slightly deviated by the blades geometry and accelerated because of the reduction of the flow passage section. In the rotating simulation, the relative velocity streamlines are shown. In the relative frame of reference, a large increase in the velocity field is shown due to the contribution of the tangential velocity to the value of velocity module. At the rotor outlet (W2) velocity magnitude is higher than the inlet one (W1).

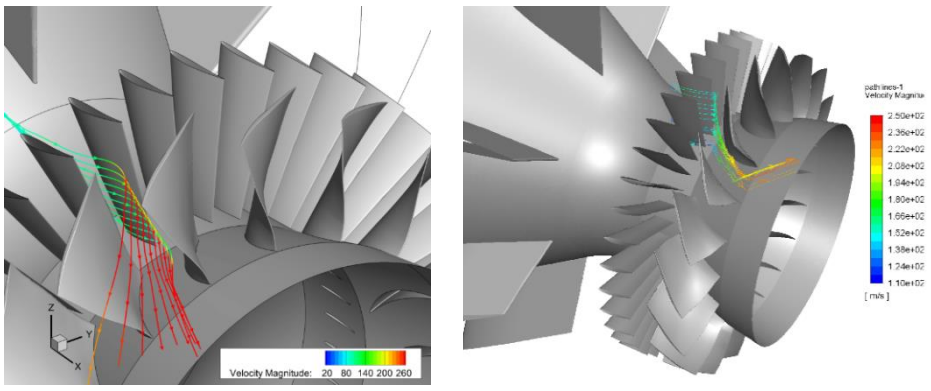

Figure 66. Streamlines crossing a rotor vain coloured with velocity magnitude in the non-rotating (left) and rotating (right) simulation. In the right figure, the relative velocity field was used to compute the fluid flow streamlines.

An overall view of the carrier phase field is shown in Figure 67 where the pressure and the velocity fields are plotted on two reference sections. For the non-rotating simulation (left), the pressure peak of 1.75 bar is in the inlet section and then it reduces up to the atmospheric pressure outlet

condition (1 bar). The fluid accelerates under the effect of the pressure gradient between the inlet and outlet sections and of the contraction of the flow passage area. For the rotating simulation (right), the inlet value of the pressure is similar to the exit value. The maximum pressure is obtained at the rotor exit section, close to the tip of the rotor blade pressure side. Focusing on the rotor, in Figure 68 contour plots of the velocity magnitude are shown on different streamwise surfaces representative of the IGV inlet as well as rotor inlet, middle and outlet sections. At the outlet of the rotor, in the non-rotating case, some low velocity zones are visible just after blades trailing edge, while high velocity regions characterize the fluid exiting rotor vanes, being maximum at the compressor hub. In the rotating simulation (right), the situation is, as expected, completely different. The velocity field follows the pressure change imposed by the rotor action: high pressure regions (not shown here) are found on the rotor blades pressure sides at the middle section, affecting the field also at the rotor inlet. The maximum pressure values are reached at the rotor exit at the tip of the blades pressure sides.

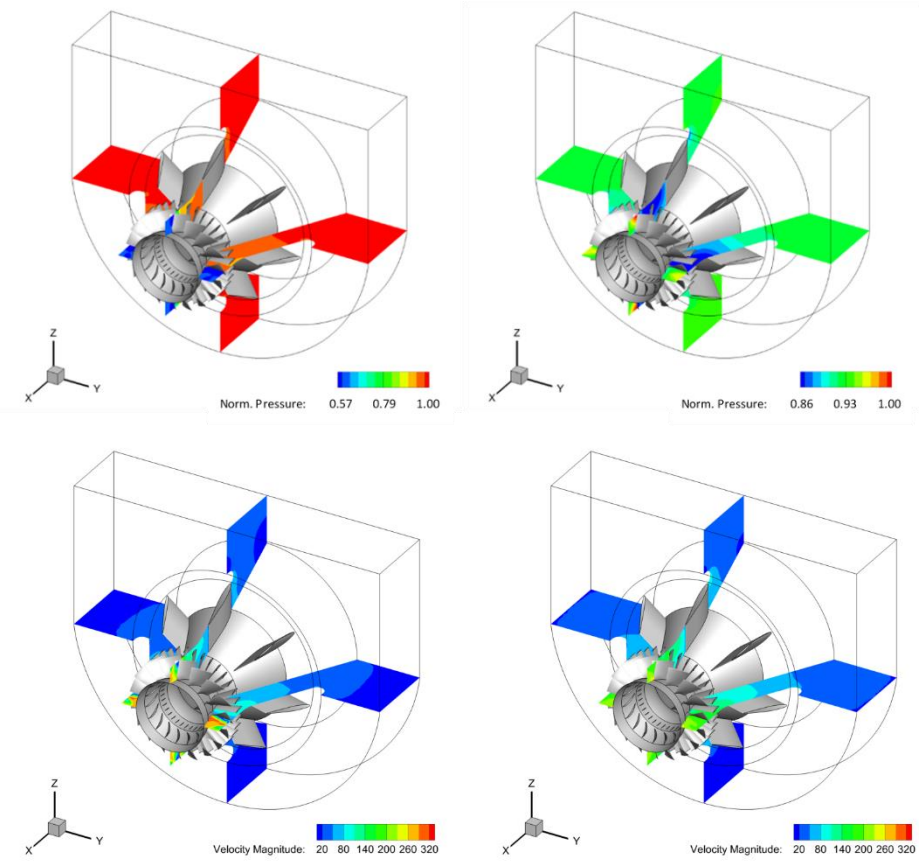

Figure 67 Pressure and velocity magnitude contour plots on the middle y- and z- sections for the static (left) and for the rotating simulation (right). Pressure values are normalized with the maximum value of each field.

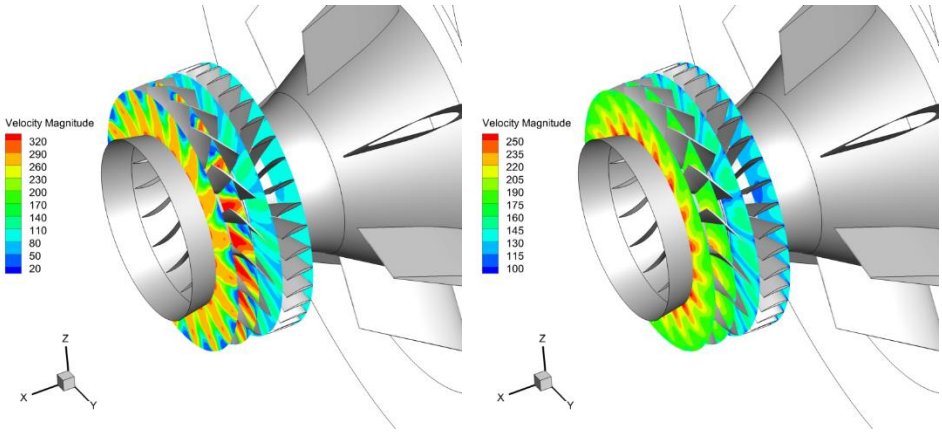

Figure 68 ***Streamwise sections at the IGV inlet, and rotor inlet, middle and outlet sections. On the left the figures refer to the static simulation while right figures refer to the rotating one.***

5.3.2. Droplet's washing behaviour

In Figure 69 the water mass accumulated on the domain walls is shown, normalized by its maximum to make this quantity independent from the specific simulation. In this test configuration, a large quantity of water is deposited on the conical surface at the inlet vain, just before the struts, and then before entering the IGV section. Part of the injected water reaches the IGV and rotor blades, which is the target of the washing system. A wide wetted region is also visible on the bottom part of the inlet vain. This is because the flow at the inlet separates in his passage around the cone where the struts are mounted, and the two streams merge at the bottom of the inlet, thus generating a region of recirculation. A small amount of water also impacts the struts, also exposing these components to the risk of erosion.

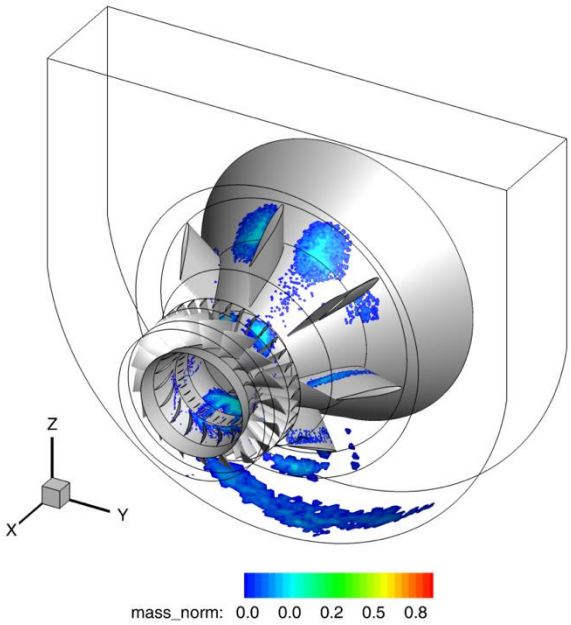

Figure 69. Wetted surfaces coloured with the normalized impacted water mass (rotating case).

On the upper part of inlet conical surface, the splashing phenomenon is also evident as shown in Figure 70 where the droplets are coloured according to their size. Droplets coming from the injectors (presenting sizes in the range from red to green) impact the surface and most of them splash generating secondary smaller droplets (with colours from light to dark blue in the figure). Therefore, part of the water mass is deposited on the impacted surface and the rest is dragged by the flow further downstream according to the adopted model previously discussed, where it may impact and splash again, or exit from the domain outlet.

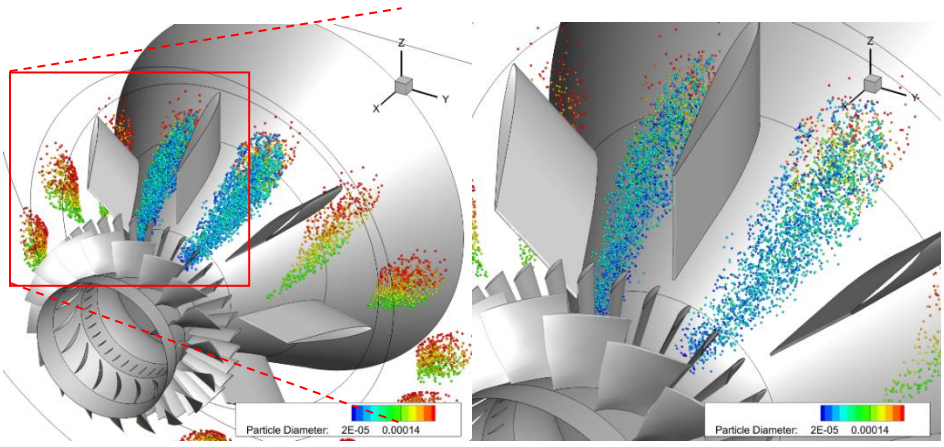

Figure 70. ***Splashing droplets on the conical surface at the inlet vain. Droplets are coloured by their diameter.***

5.3.3. Comparison of erosion in non-rotating and rotating cases

In the real computation it is not possible to consider a rotating mesh due to the large rotational velocity. Then, even if the velocity is computed in the relative frame of reference, the droplets motion cannot take in account the blade motion. Then, the water impact is concentrated only in some blades even if such impacts should be distributed around all the rotor blades. However, this circumstance allows to work in safe conditions as in the real case the number of impacts per blade will be surely reduced.

In Figure 71 and in Figure 72 droplets impacts on rot08 for non-rotating and rotating case are shown. It can be observed how the wetted pattern is different in the two cases: in the non-rotating case most of the impacts are concentrated in the suction side (SS), while in the rotating one in the pressure side (PS). This is due to the imposed rotation. Indeed, in the rotating case, once the droplets enter the rotor region, their dynamics is mainly governed by the high rotational speed of the blades, which move the droplets toward their pressure side. On the contrary, in the non-rotating case the wetted pattern is more dependent on the history of droplets dynamics, so they may impact other parts of a blade.

A large amount of water droplets impacting the same surface may provoke WDE. An indication of the risk of erosion is provided by the accumulated-to-incubation-energy ratio: in the non-rotating case the accumulated-to-incubation-energy ratio value is five orders of magnitude smaller than that in the rotating case. This indicates that, as expected, WDE risk is higher in on-line WW. A confirmation of this comes from the erosion patterns on the PS of blade rot08 reported in Figure 73. Here the erosion is normalized by its maximum to make the obtained value independent from the amount of injected water. As clear from the figure (left side), no erosion has been found in the non-rotating case, on both the PS and SS surfaces. On the contrary, in rotating case (Figure 73-right), WDE takes place, and the LE is the most exposed part of the blade. Even in this case no erosion has been found on the SS.

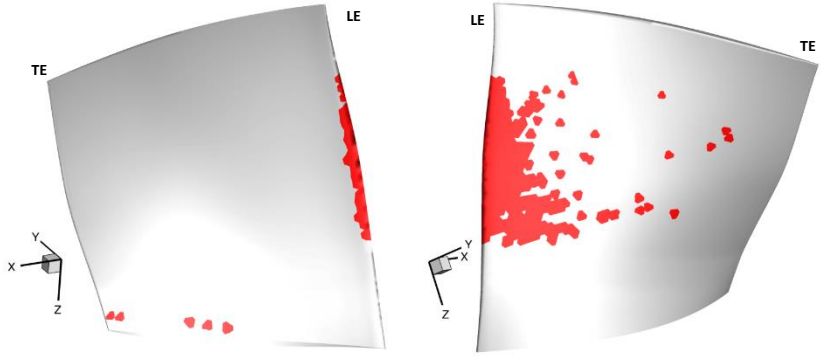

Figure 71. Surfaces affected by droplets of rotor blade no. 8 (rot08, non-rotating case). Pressure side (left), suction side (right); leading edge (LE), trailing edge (TE).

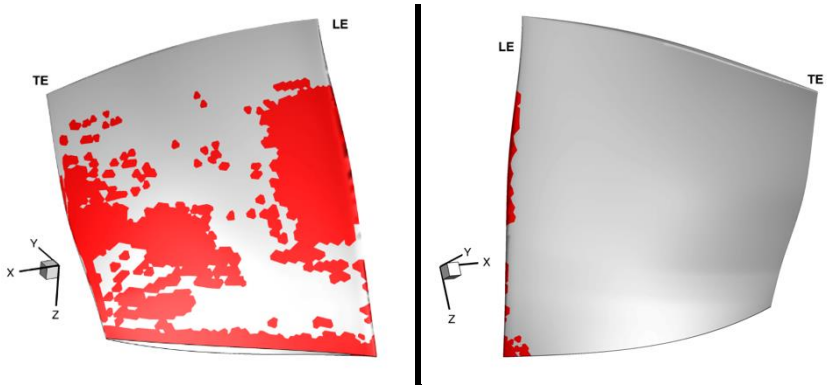

Figure 72. Surfaces affected by droplets of rotor blade no. 8 in the rotating simulation (rot08, rotating case): Pressure side (left); suction side (right).

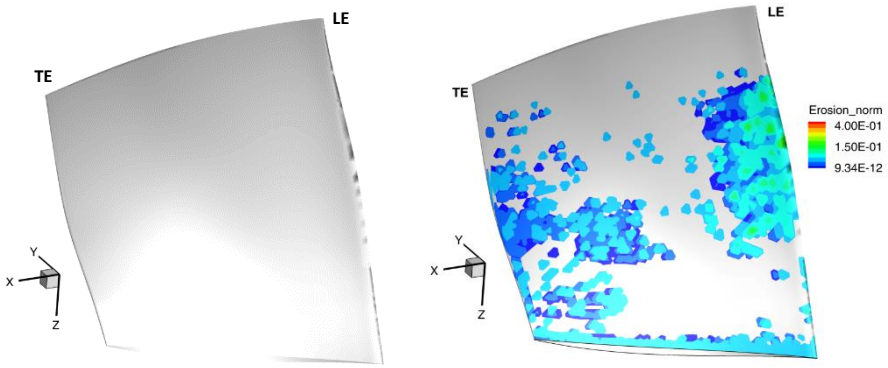

Figure 73. ***Normalized erosion on the PS of Rotor blade no. 8 (rot08); non-rotating case (left), rotating case (right).***

Another interesting aspect emerging by comparing Figure 73-right and Figure 73-left is that not the whole wetted surface is eroded. Indeed, erosion is a combination of several factors, such as the accumulated and incubation energies, the impact velocity and angle, and the properties of the involved material, thus a droplet impact not always results in material removal from the target. Due to the previous considerations, only rotating case has been considered in following chapters.

Chapter 6

Washing process efficiency evaluation indexes

Reproduced in part from: F. Di Gruttola, G. Agati, P. Venturini, D. Borello, F. Rispoli, S. Gabriele, D. Simone, *Numerical study of droplet erosion in the first-stage rotor of an axial flow compressor*, Turbo Expo 2021, paper no. GT2021-59661

In this chapter, the methodology defined in the previous chapter for the rotating case has been used to define the washing process efficiency by introducing suitable evaluation indexes.

6.1. Water washing indices

Water washing efficiency (WWE) is a quantity not uniquely defined since it depends on several factors. In fact, WWE depends on the capability of the injection system to reach the desired surfaces but also on the ability of water to dissolve dirt. The amount of water impacting a given surface and the impact conditions play a crucial role in removing the fouling. Despite it is very hard quantifying the WWE, some of the mentioned aspects can be represented by appropriate indices. The quantities used to compute the indices were calculated through the UDF developed by the authors.

Wet-to-total surface (WTS): this is the ratio between wet and total surfaces. It measures the fraction of a surface impacted by water droplets. A larger WTS may result in a higher WWE.

Impacted-to-Total water mass (ITM): this quantity represents the fraction of the total injected water that impacts a surface. It provides an indication of the quality of the injection system: the larger ITM the less water flow is needed to wash the compressor.

Local Impacted water fraction (LIF): this quantity represents the fraction of the total impacted water mass that impacts a specific surface. It provides an indication of the capability of the washing system to wash the compressor surfaces: the larger the LIF the larger WWE is supposed to be.

Non-dimensional impacted to total water mass per unit of wet to total surface (IMWS): this is the ratio between two non-dimensional quantities, the impacted to total water mass (ITM) and the wet to total surface (WTS). As reported in [15] the increase of the water wash rate results in a higher WWE that might reduce compressor aerodynamic performance. This means that,

keeping constant the other quantities, the larger the amount of water per unit surface, the better the system is supposed to wash.

It is worth noting that such indices can be global or local, meaning that they can be computed in the whole machine or locally in some of its parts, depending on the focus of the analysis.

Computational Domain

6.1.1. Computational Domain and Mesh

As already anticipated in previous chapters, the inlet section of a real axial compressor up to the first-stage rotor is considered to account for the asymmetrical distribution of the water injectors and the non-commensurable ratio among struts, IGV and rotor blades.

Because of the high rotational velocity of the rotor, the idea of considering a moving mesh approach is unrealistic. Then, a frozen rotor approach was selected to have the most accurate prediction. Unfortunately, such configuration can generate some uncertainty in the relative position of the rotor blades leading edges (compared with IGVs trailing edges). For this reason, two configurations were analysed consisting in two different positions of the rotor blades with respect to the IGVs, represented in Figure 74.

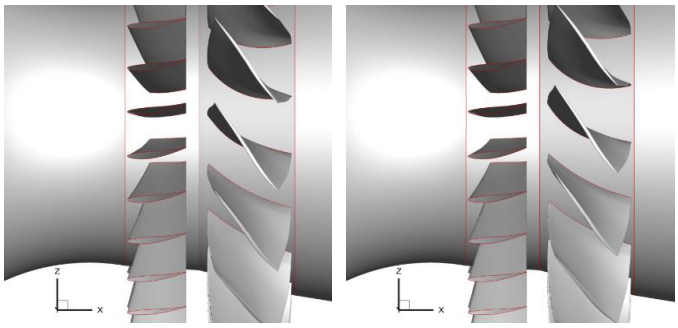

Figure 74. ***Different Rotor-IGVs Mutual Position Considered in the Study (Mesh1: Left; Mesh2: Right). © 2021 Baker Hughes Company - All rights reserved.***

The first configuration (Figure 74 left) represents the situation in which the rotor blade leading edges are aligned with IGVs trailing edges. In the following, this geometry will be called Mesh1. In the second configuration (Figure 74 right), the full rotor has been rotated to have rotor blades leading edges in the middle of the IGVs vanes. The simulations performed on this domain will be recalled in this study as the Mesh2 simulations. Considering both these configurations allows to simulate the opposite conditions that can be found in terms of WWE and erosion rate. Mesh1 reproduces the case when the rotor leading edges are in the wake of the IGVs and only a fraction of the droplets will impact on the leading edge; Mesh2, on the other hand, represents the configuration where the rotor is fully impacted by the water droplet. Long-term averaging of the washing process will return an intermediate behavior between the two conditions. This aspect will be analyzed in future works.

The meshes realized for the two computational domains are slightly different. Both are composed of tetrahedral cells, clustered in the wall regions to guarantee values of the y+ ranging between 20-300. Such range represents the interval of applicability of the standard wall function. Mesh1 is composed of 21 M tetrahedral cells while in the Mesh2 the discretization has been refined to range up to 25 M cells to guarantee the y+ in the rotor region. An overview of the computational domain is shown in Figure 75.

6.1.2. Fluid and Discrete Phase Boundary Conditions

The air flow enters the domain from the upper surface of the inlet compressor region and exits from the outlet section (blue and green surfaces in Figure 75). A mass flow boundary condition is used for the inlet. At the outlet, a pressure outlet BC is adopted. The value of the pressure at the outlet was obtained by calculating the Eulerian work exerted by the rotor to the fluid and compared with the industrial design value. All the other surfaces are treated as no slip adiabatic walls. As reported, a frozen rotor approach is adopted to model the rotation of the machine. For this purpose, a rotation ω=7800 rpm with respect of the negative x-axis was set for the rotor cell-zone. The rotating components (the rotor lower wall and the rotor blades) are set as rotating walls with null angular velocity in the relative frame of reference, while for the upper casing (not shown in Figure 75) a positive angular velocity ω=7800 rpm was imposed.

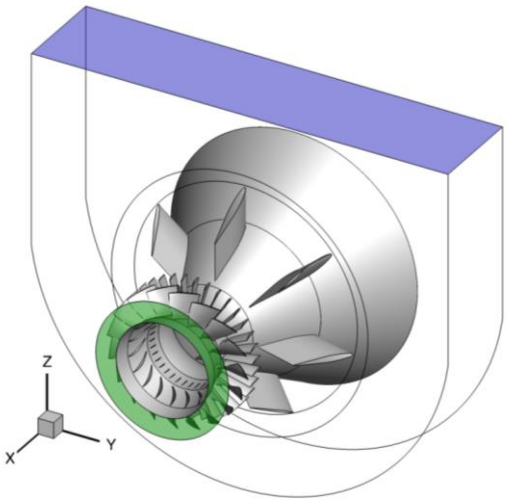

Figure 75.: ***Computational Domain (Top): Inlet (Blue) And Outlet (Green) Surfaces. © 2021 Baker Hughes Company - All rights reserved.***

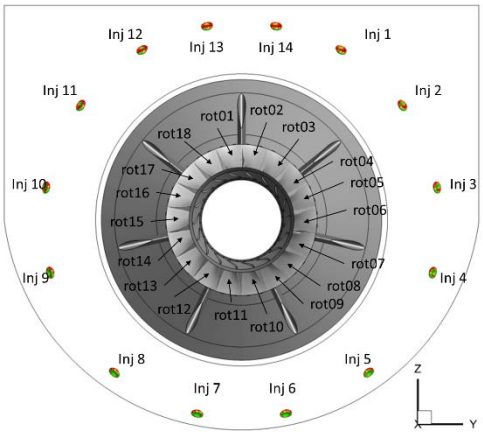

Figure 76*: Injectors and Rotor Blades Numbering as Adopted in The Text. © 2021 Baker Hughes Company - All rights reserved*

Regarding the discrete phase (water droplets), this is injected by 14 nozzles distributed circumferentially along the inlet section of the domain as illustrated in Figure 76. For this purpose, the cone injector model in Fluent [43] was selected as the most appropriate to reproduce real injection conditions. Two different spray nozzles were simulated by varying the water-to-air mass fraction (WAMF). The first one represents the baseline (that in the following will be indicated as A, WAMF=A), while the second one has a WAMF about three times larger. Given the mass flow rates and the nozzle diameter, one can compute the injection velocities needed to define the cone injector model. The analyzed nozzles, working with different operating pressures generate also different droplet size distributions that in the present work are assumed to follow a Rosin-Rammler distribution. A summary of the injection conditions is reported in Table 20.

Droplets may escape from the numerical domain through the outlet sections. However, if a droplet impacts a wall it may splash generating secondary smaller droplets according to [49] or deposit forming a liquid film on the impacted surface.

***Table 20: Tested Nozzles Characterization*.**

Nozzle Id	***WAMF***	***Spray Angle***	***Droplets (d_{min}–d_{max})***
1	A	53°	50 - 305 µm
2	3A	72.5°	40 - 250 µm

6.1.3. **Performed Simulations**

In the present study four different simulations are analyzed. The two nozzles described in Table 20 were tested on both the computational domains (Mesh1 and Mesh2). The set of performed simulations is reported in Table 21.

Table 21*: *Summary of The Performed Simulations

Simulation #	*Domain*	*Nozzle*
1	Mesh1	A
2	Mesh1	3A
3	Mesh2	A
4	Mesh2	3A

In the discussion of the obtained results, the performed simulations will be referred to by indicating the used computational domain (Mesh1 or Mesh2) and the WAMF characterizing the tested nozzle. It may be worth recalling that simulations on the two meshes can be considered as complementary. For every nozzle, results regarding droplets impact and erosion should be averaged between the rotor blades and between the two meshes to account for the component rotation. Nevertheless, by considering both the configurations, namely Mesh1 and Mesh2, it is possible to have an overall scenario on the impact behaviour of the injected droplets in the frozen rotor framework.

6.2. Results

The relevant outcomes of the present work are presented and discussed in the following subsections. After a description of the carrier phase main features, the risk of erosion and the evaluation of the washing efficiency will be analyzed by means of the newly defined indices.

6.2.1. Flow field

First of all, Figure 77 shows the streamlines released from the inlet section and colored by the normalized velocity magnitude for Mesh1.

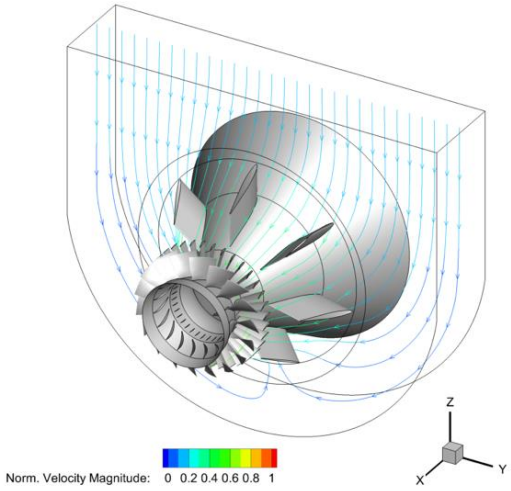

Figure 77*: Streamlines Coloured by the Velocity Magnitude Normalized by its Maximum for the Mesh1. © 2021 Baker Hughes Company - All rights reserved.*

The flow field appears symmetric in the inlet case, mixing in its bottom part where a recirculation region is created. The symmetry is broken when the IGVs are reached. It is worth to mention that the streamlines in Figure 77 are interrupted across the rotor blades since they are drawn in the absolute reference. Focusing on the rotor region, in Figure 78 the normalized values of velocity magnitude (a) and total pressure (b) are shown for rotor inlet, middle and outlet streamwise sections, as well as for the symmetry z-plane, for Mesh1 (a.1, b.1) and for the Mesh2 (a.2, b.2). In the two meshes, as expected, the average fluid flow is accelerated, and an increase of the total pressure is observed because of the work delivered to the fluid through the shaft rotation. The overall features of the flow field look similar but, as it will be shown later, the change of the mutual position between IGVs and rotor airfoils influences the impact dynamics of the droplets on the rotor blades.

In Figure 79-top, fluid streamlines in the relative reference frame crossing the rotor are presented. Streamlines are colored with the total pressure. As expected, the fluid flow is strongly deviated when entering the rotating volume and a large increase in the total pressure is observed because of the shaft rotation.

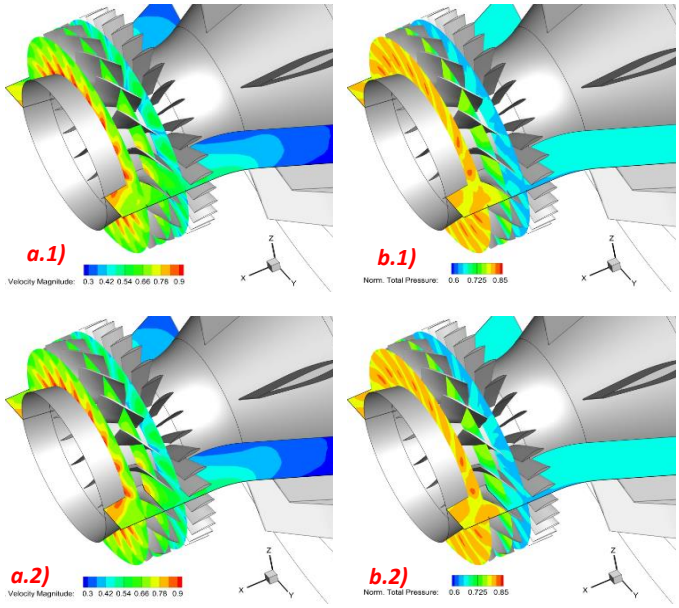

Figure 78: ***Normalized Velocity Magnitude (A) and Total Pressure (B) In the Rotor Region For Mesh1 (1) And Mesh2 (2). © 2021 Baker Hughes Company - All rights reserved.***

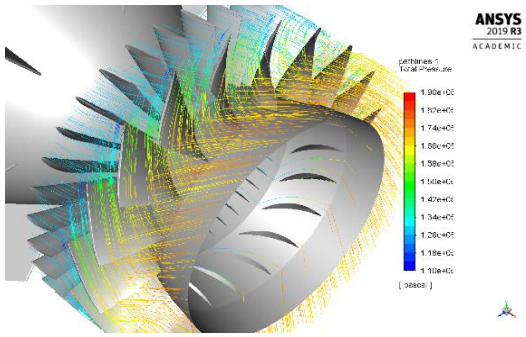

Figure 79: Streamlines Drawn in the Relative Reference of Frame and Coloured By the Fluid Total Pressure, in The Rotor of Mesh2. © 2021 Baker Hughes Company - All rights reserved.

6.2.2. Droplets: Wet Surface and Erosion

Despite the carrier phase has similar features between the performed simulations, droplets behavior strongly changes by varying the WAMF. In general, when entering the rotor zone the injected phase is accelerated and deviated towards blade pressure sides following the relative streamlines depicted in Figure 79. Droplets characterized by a larger inertia will also impact rotor suction sides. In Figure 80 the Wet Surface is presented by means of the accumulated energy calculated through the use of the UDF for the two WAMFs simulated in Mesh 1 (similar plots for Mesh 2 are not shown for the sake of brevity). For both the WAMFs, part of the droplets also impacts on the internal cone where struts and IGVs are mounted, eventually provoking the formation of a liquid film. Splashing phenomena (not shown here) are observed mostly on the upper part of the internal cone, where droplets impact with higher velocity. These phenomena are more evident when using a WAMF=3A because of the higher injection velocity which results in a stronger inertia of the dragged phase. By injecting the triple of the water mass flow rate, the wet surface reasonably increases in all the zones of the computational domain. In Figure 80 this is mostly evident in all the inlet region. In all the following contour plots, both the accumulated energy and the erosion have been normalized by the maximum of each simulation. The color scales have been adjusted in such a way to make clearer the quantity variation.

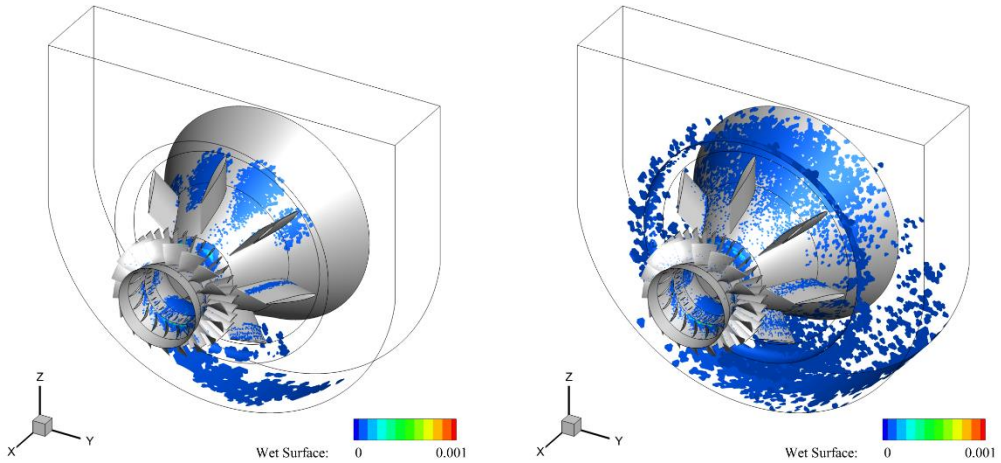

Figure 80*: Wet Surface for Mesh1 with WAMF=A (Left) and WAMF =3A (Right). © 2021 Baker Hughes Company - All Rights Reserved.*

Figure 81 and Figure 82 show the wet surface on the rotor blades for the simulation at WAMF=A and WAMF=3A, respectively. The front views (Figure 81-a.1, b.1) show the pressure sides of rotor blades, while Figure 81-a.2, b.2 depict a back view of the full rotor, i.e. the suction sides. Rotor blades impacted by the injected droplets are the same in Mesh 1 (figures a) and Mesh 2 (figures b), however, the wet surface region of each blade differs between the two domains. For both the WAMFs here investigated, rotor leading edges show larger wet regions in Mesh2 because of the alignment between IGVs and rotor blades as shown in Figure 74. In all the considered configurations, droplets mostly impact the blades in the lower region of the domain. This aspect will be further analyzed in the following paragraph. The different impact regions between Mesh1 and Mesh2 motivates the consideration of the configurations in the analysis.

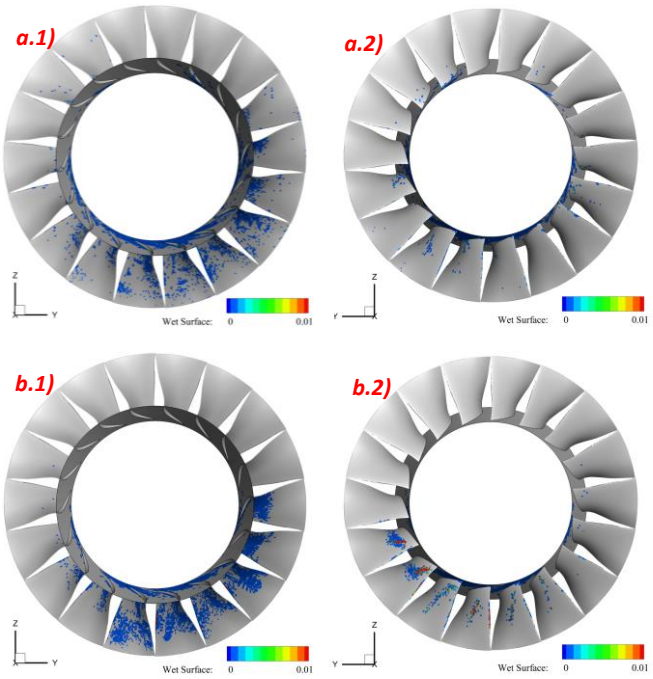

Figure 81: ***Wet Surface for Mesh1 (A) And Mesh2 (B) for WAMF=A. Rotor Blades: Pressure Side (1), Suction Side (2). © 2021 Baker Hughes Company - All Rights Reserved***.

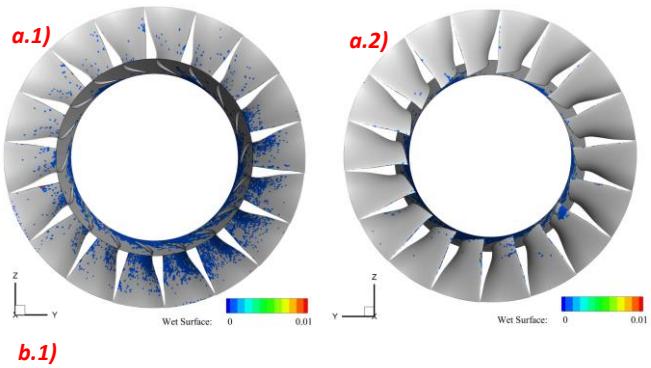

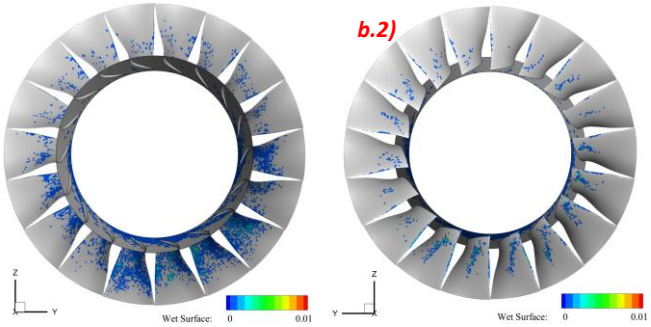

Figure 82*: Wet Surface for Mesh1 (A) and Mesh2 (B) for WAMF=A. Rotor Blades: Pressure Side (1), Suction Side (2).* ***© 2021 Baker Hughes Company - All rights reserved.***

When increasing the injection WAMF up to 3A, the injected droplets impact all the blades, even the lower ones remain the most affected (see Figure 82). In this case, stronger splashing phenomena occur. The higher injection velocity results in larger impact energy on the lower internal cone and a larger number of smaller secondary droplets is generated. Such smaller droplets have obviously lower inertia and this feature makes the droplets more prone to follow the carrier phase streamlines. Hence, the impacts are more evenly distributed on the whole rotor. In general, when the rotor leading edges are placed in the middle of the IGVs vanes (i.e. Mesh2 configuration), rotor blades result more wet.

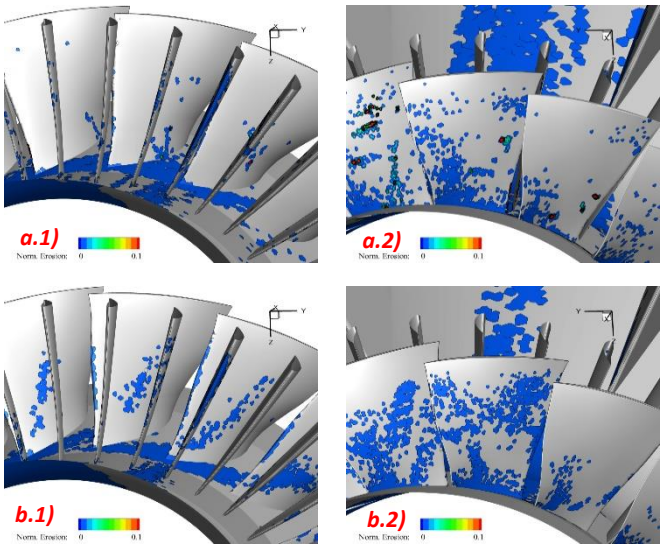

Figure 83: ***Normalized Erosion on Rotor Blades ROT11 – ROT5 (From Left to Right). Mesh1 (A) And Mesh2 (B) with WAMF=A; Suction Sides (1), Pressure Sides (2).*** ***© 2021 Baker Hughes Company - All rights reserved.***

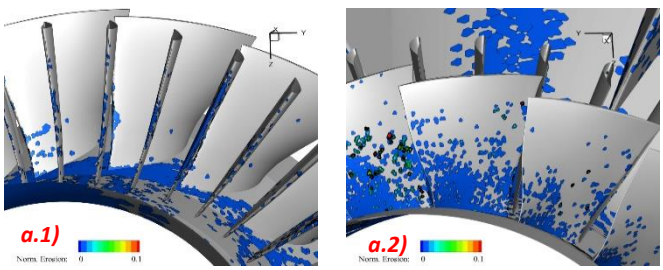

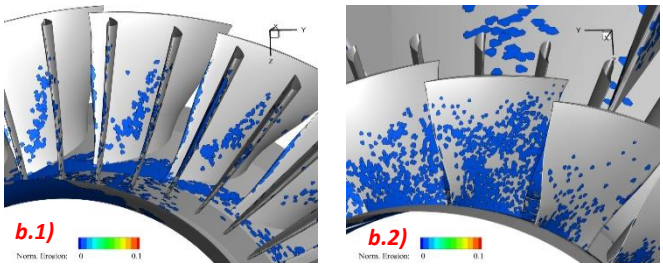

Figure 84: ***Normalized Erosion on Rotor Blades ROT11 – ROT5 (From Left To Right). Mesh1 (A) And Mesh2 (B) with WAMF=3a; Suction Sides (1), Pressure Sides (2).*** ***© 2021 Baker Hughes Company - All Rights Reserved***

The different impact behaviors among the analyzed simulations also generate different erosion patterns on the compressor components. Figure 83 and in Figure 84 depict erosion patterns on the inferior rotor blades in the case of WAMF=A and WAMF=3A, respectively. In Mesh1 some erosion peaks are observed in the rotor pressure side: droplets after exiting the IGV vanes are deviated and accelerated and the high impacts velocity result in a strong erosion of blades pressure sides. In Mesh 2 the highest values of erosion are found on blade leading edges. Similar erosion patterns are visible on the suction sides of Mesh2 (Figure 83-b.1 and Figure 84-b.1) for the two WAMFs that can be related to geometry issues. When increasing the WAMF, the more effective washing leads to larger eroded regions in the first-stage rotor. Material erosion is found in the lower part of the blades pressure sides for the whole set of simulations here considered (Figure 83-a.2, b.2, and Figure 84-a.2, b.2), while blades tip is not impacted neither eroded.

6.2.3. Washing efficiency evaluation

To quantify the effect of the two geometries and of the two WAMFs simulated on the WWE, the indices introduced are adopted.

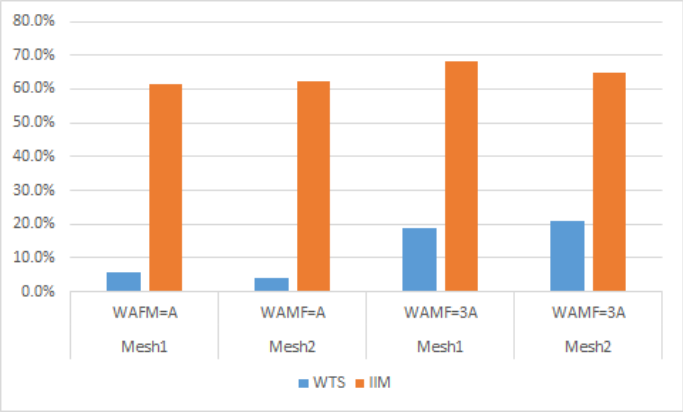

Figure 85*: Total WTS (blue) and ITM (orange) at WAMF=A and WAMF=3A, on Mesh1 and Mesh2.*

In Figure 85 global WTS and ITM are reported, while in Figure 86 global IMWS is shown. These indices are representative of the injection efficiency, namely the amount of water impacting a surface and how the water spreads. WTS is about 5.0 % in both the meshes, with only little difference ($\pm 0.7\%$) due to the relative position between IGVs and rotor blades in Mesh1 and

Mesh2. A larger variation is detected by increasing WAMF: in this case WTS mean value is about 20.0 %, still having a small difference between Mesh1 and Mesh2 ($\pm 1.0\%$). ITM trend is similar to WTS, but the difference between WAMF=A and WAMF=3A is smaller, with a gap of only about 7.0 %.

As for the global IMWS index (Figure 86), it is clear that it decreases when WAMF increases. This means that in the present configuration, the increase of water flow probably does not lead to an improvement of the WWE. However, to better understand and explain this behaviour, local indices are needed.

ITM in Figure 87 is related to the injectors, namely it reports, for each injector (see Figure 76for their positions), the percentage of the deposited water with respect to the whole amount of the injected one. As shown in the figure, not all the injectors have the same ITM, and this may give an indication on how to optimize their position. Looking at WAMF=A (Figure 87-top), it is clear that only Inj1 and Inj14 work at their best: each injector sprays 7.14% of the total injected water (1/14th of the total), thus ITM for each injector can reach a maximum of 7.14%, and this is about the situation of the two mentioned injectors. ITM of Inj6, Inj7 and Inj8 are a bit smaller; all the others show an even smaller index. Increasing WAMF (Figure 87-bottom), ITM becomes a slightly more uniform, meaning that the difference between the peaks and the throats are smaller than in the case of WAMF=A.

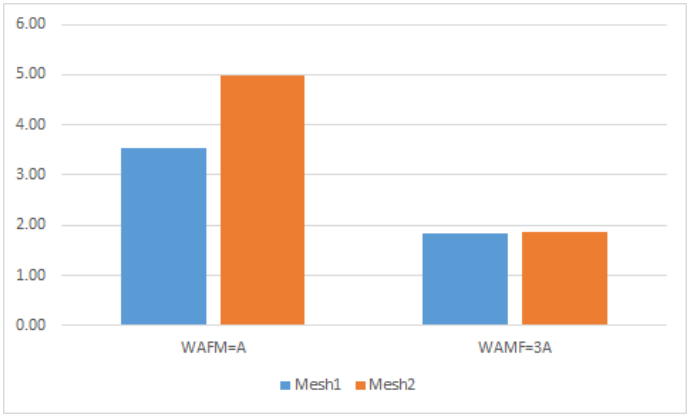

Figure 86*: Global IMWS at WAMF=A (left) and WAMF=3A (right), on Mesh1 (blue) and Mesh2 (orange).*

However, ITM indices are not sufficient to evaluate the efficiency of the washing system. Other parameters have to be considered. Numerical domain was divided into five parts (Figure 88): Inlet case, Struts & Cone, IGVs, Rotor, and Outlet. For each of them WTS, LIF, and IMWS have been computed. Figure 89 reports the wet surface percentage (WTS) of the domain regions, at WAMF=A and WAMF=3A for Mesh1 and Mesh2. Looking at WAMF=A, in both the domains (Mesh1: blue; Mesh2: orange) a very small fraction of each zone surface is impacted by water, with the maximum recorded in Struts & Cone (8.4 % in Mesh1). There are very small differences between the two meshes: the largest difference is in the Outlet region, but this is not relevant since in that region there are the stator blades, not included in present simulations. So, the maximum difference is in the Inlet case, but it is about 1.6%. The use of a larger WAMF results

in a similar trend but with some differences. In particular, the most relevant variation is measured in the Inlet case region: at WAMF=3A about 25% of the surface is wet (in Mesh1), while it is about 5% at WAMF=A. In Struts & Cone there is about the same wet surface as in the previous case (with about 2% increase); in IGVs and Rotor it can be observed the same trend as for WAMF=A, but with a larger wet surface, as expected.

Figure 87: ITM of each injector at WAMF=A (Top) and WAMF=3A (Bottom), in Mesh1 (Blue) and Mesh2 (Orange).

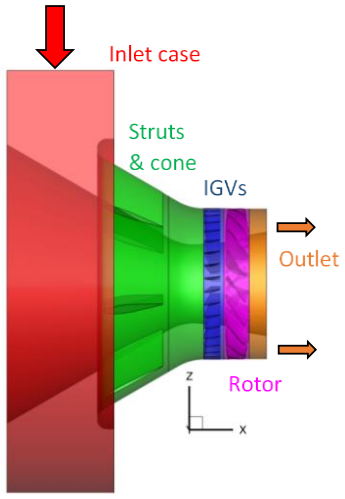

Figure 88: Zones of The Numerical Domains. © 2021 Baker Hughes Company - All rights reserved.

Some additional details come out from the analysis of LIF and LIF/WTS indices. Figure 90 shows LIF in the domain regions of both the meshes, and varying WAMF. Apart from few differences between Mesh1 and Mesh2 in Inlet case and Rotor, which can be ascribed to a certain degree of randomness of the injection and (for Rotor) to the relative position between IGVs and Rotor blades, some general trends can be put in evidence. Looking at the Inlet case region, it is clear that increasing WAMF the amount of water impacting its surfaces increases. The exact opposite trend is instead observed in the Struts & Cone area. Increasing WAMF means modifying the injection parameters, such as injection cone and droplet size and velocity. Therefore, at WAMF=3A a larger number of droplets impact the Inlet case (especially the conical surface) splashing and giving rise to a number of smaller droplets. Such small drops are more prone to follow the flow (they have a small inertia), and this may be the reason why in the Struts & Cone, downstream the Inlet case, the amount of water impacting a surface reduces rather than increases.

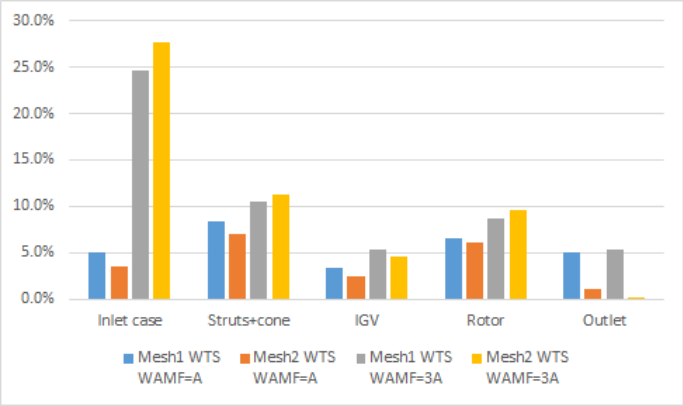

Figure 89: WTS in Mesh1 and Mesh2, AT WAMF=A and WAMF=3A.

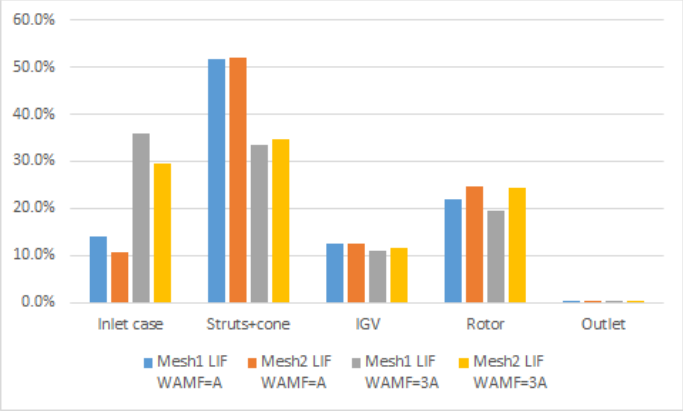

Figure 90: LIF in Mesh1 and Mesh2, at WAMF=A and WAMF=3A.

Coupling the LIF datum with the wet surface, an estimation of the amount of water impacted per unit surface can be inferred, which may be a good way of measuring the WWE (the larger is the

amount of water per unit surface, the more efficient the washing process is expected to be). To have an index independent from the amount of water injected in the simulation, IMWS (LIF/WTS) (Figure 91) has been computed. Increasing the WAMF does not result in an automatic increase of the amount of water deposited per unit surface. Analysing the Rotor region (the most relevant for the efficiency of the whole engine), it is clear that the higher WAMF provokes a reduction in the LIF/WTS index (in both the meshes analysed), which is not good for the washing efficiency. The same trend is noticed in all the domain regions. This means that an increase in WAMF affects more the wet surface than the amount of water impacting a surface.

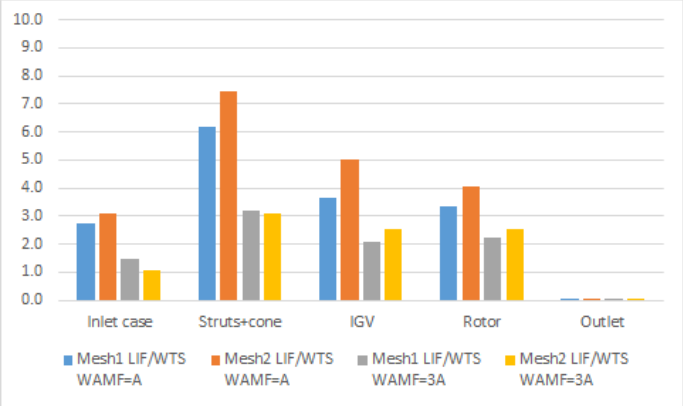

Figure 91: IMWS in Mesh and Mesh2, at WAMF=A and WAMF=3A.

A further analysis can be performed in the Rotor region to analyze the circumferential distribution of water. For the sake of brevity, such analysis is limited to Mesh2, at the two different WAMF (the trend in Mesh1 is similar). Figure 92 shows WTS index as distributed along the 18 rotor blades (see Figure 76). This would be the WTS in the case of steady blades; in the real application, since the blades rotate, WTS is the same in each blade, and this can be assumed to be the average value accounting for the contribution of water coming from each blade region. However, it is useful to study the circumferential distribution of water in the view of optimizing the injection system. As shown in figure 92, the configuration studied in this work concentrates the water in the lower part of the rotor, between rot06 and rot13. In the case of smaller WAMF no water reaches the upper region (rot01-rot04 and rot15-rot18). With WAMF=3A all the blade regions are impacted by water. However, the larger wet surface percentage remains in the lower rotor zone.

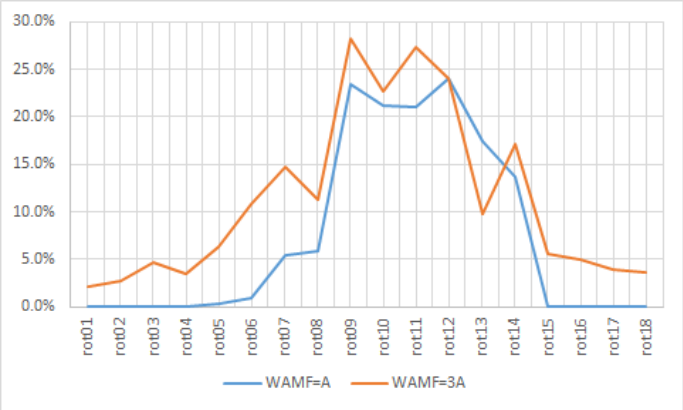

Figure 92: WTS in Mesh2 at WAMF=A and WAMF=3A.

A similar trend is detected by IMWS index (Figure 93), but in this case, the WAMF increase does not reflect an increase of the index. IMWS is a measure of the water per unit surface, and here increasing WAMF results in a smaller amount of water per unit surface (apart from the upper part of the rotor). This is connected to what said above commenting Figure 89. At WAMF=3A a larger number of droplets impact the Inlet case splashing and splitting into a number of smaller droplets. These small droplets have a small inertia; thus, it is more difficult for them to impact the rotor blades, and other obstacles in general. In this case, the increase of WAMF does not seem to lead to a higher WWE. It is then clear that the optimization of the washing system is the result of the combination of all parameters, and it is not possible to reach a good configuration acting on just one of these.

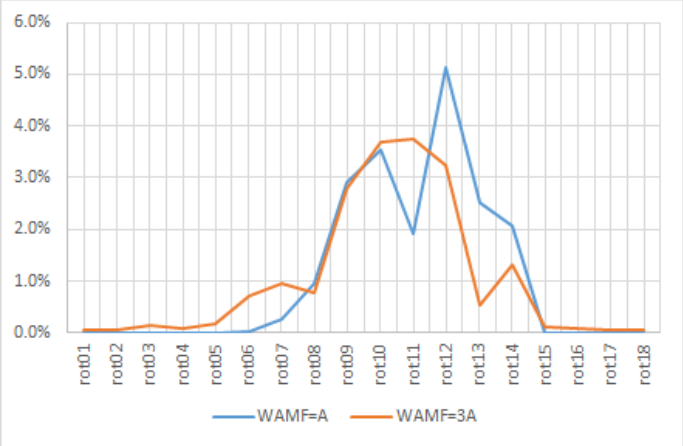

Figure 93: IMWS in Mesh2 at WAMF=A and WAMF=3A.

6.2.4. **Results Discussion**

Considering the results shown in previous paragraphs, some conclusions can be drawn:

a) The need to analyze the erosion mechanism across all the rotor with the frozen rotor approach requires to study at least two different configurations representing different relative position between IGVs and rotor blades.
b) Wet surface clearly increases by tripling the WAMF. All the rotor blades are impacted by the droplets when using a WAMF=3A. In addition to the augmentation of the injected mass, this can be related to stronger splashing phenomena that help in the spreading of the injected phase.
c) Erosion is observed on both the sides of the blades. In the configuration where rotor leading edges are in the wake of IGVs trailing edges, maximum values of erosion are found on rotor blades pressure sides, while, when changing rotor relative position with the IGVs, the highest erosion is found on rotor blades leading edges.
d) To evaluate the Water Washing Efficiency and the ensuing blade erosion, specific parameters are introduced aiming at evaluating the relative extension of the wet surface, the fraction of water effectively used and their ratio. Two different water injection regimes were considered. The results were analysed at global, region and single blade level.
e) The availability of the specific functions here considered represents a very useful prediction tool for assessing the water washing procedure in terms of number of injectors, water mass flow rate, in order to exploit washing capability as well as erosion growth rate.
f) The proposed indices provide relevant information about the washing system. Such indices can be used to optimize the injection system and the washing parameters to improve the Water Washing Efficiency.

Chapter 7

Evaluation of water washing efficiency and erosion risk in LT16 AXCO for different water injection conditions

Reproduced in part from: G. Agati, F. Di Gruttola, S. Gabriele, D. Simone, P. Venturini, D. Borello, *Evaluation of water washing efficiency and erosion risk in an axial compressor for different water injection conditions,* ATI, 2021.

In this Chapter, the on-line water washing process under six different water injection conditions has been reproduced based on the computational domain ad the flow field discussed in previous Chapters. Results have been analysed comparing the effects of the different configurations.

7.1. Computational details

The numerical domain adopted to perform the numerical simulations has been already described in Chapters 5 and 6, Figure 94.

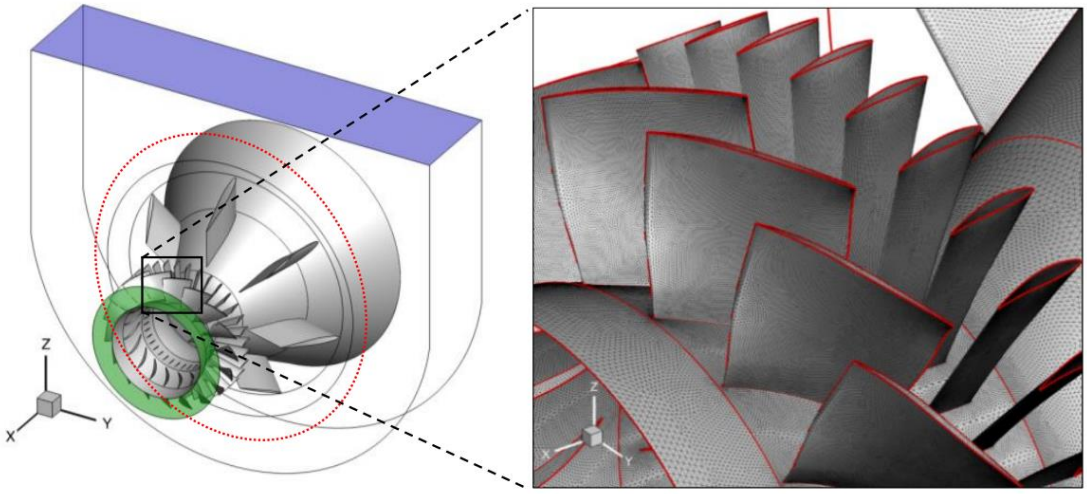

Figure 94. Numerical domain (left) and zoom-in of the first-stage rotor (right); red dotted line: line of injector positions [21,23]. © 2021 Baker Hughes Company - All rights reserved.

For data confidentiality reasons, the water mass flow used has been normalized (NWF); the whole range (0.25-1.0) is covered using two type of nozzles, namely N1 and N2, the former ranging between 0.25 and 0.50 NWF, the latter between 0.625 and 1.0.
Table 22 reports the NWFs analysed in the present work and the respective nozzle name, together with the injection angles and droplet size ranges. For each NWF the respective size range is divided into six classes, covering about 80% of the total injected mass, in order to have reliable results.

Table 22. Injector name, NWF, injection angle and droplet size range

Nozzle	NWF	Injection angle (°)	Droplet size range (μm)
N1	0.250	53.0	50-305
	0.375	71.5	45-277
	0.500	72.5	40-250
N2	0.625	84.5	35-305
	0.750	84.5	35-281
	1.000	87.5	35-242

7.2. Results and Discussions

In the following section the main results in terms of erosion damage and water washing efficiency are reported using the flow field described in Chapters 5, 6 and the indices introduced in paragraph 6.1.

7.2.1. Washing efficiency

Figure 95 reports WTS and ITM indices for the machine regions (namely Inlet case, Struts & Cone, IGV and Rotor) composing the considered domain. It is evident (Figure 95 -top) that the region showing the most variable WTS index with NWF is the Inlet case. It shows a continuous increase of that index as the NWF increases, starting with WTS about 15 % in the case of NWF=0.25 and reaching more than 55 % in the case of NWF=1.0. WTS variations in the other regions are less pronounced. The rotor region in particular, shows an asymptotic trend: using NWF>0.625 does not provoke any relevant variation in the wet-surface index, which stabilizes around 24%. The situation is similar for ITM index (Figure 95 -bottom) but with some differences. The Inlet cone is still the region most sensitive to NWF variations, showing an increase of ITM index but in this case the variation is less evident (about 20%). The ITM in the Struts and Cone region, on the contrary, decreases with the increase of NWF, going from about 39% for NWF=0.25 to about 28% for the case at NWF=1.0. This can be related to what happens in the Inlet case region: the larger mass impacting the Inlet region observed by increasing the NWF results in a minor number of droplets' impacts on the rest of the domain. In the rotor region a decreasing asymptotic trend of the ITM index with NWF is detected: by injecting with NWF>0.5 the ITM index stabilizes around a value of 25%. The normalized impacting water mass per unit surface (IMWS) is reported in Figure 96. In all the domain regions there is an increase of IMWS with NWF. This could appear to be in contrast with the ITM trend. However, ITM represents the percentage of the impacted water impacting a specific surface, but it is not related to the amount of water impacting a

surface. Increasing the water mass impacting a unit surface on the one hand could result in a larger washing efficiency, but on the other hand it increases the risk of erosion. Within this framework, in the present geometry IGV and Rotor regions are the most exposed to erosion risk.

Figure 95. WTS (top) and ITM (bottom) in the domain regions

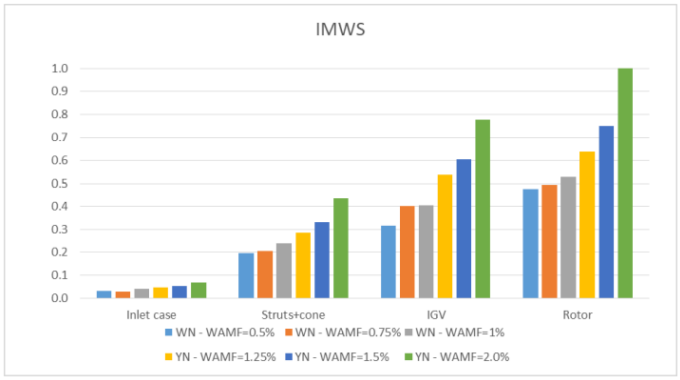

Figure 96. IMWS in the domain regions

Since the most mechanically stressed and critical part of the machine is the rotor, that region has been carefully analyzed. Figure 97 recalls the injectors and blades names. Figure 98 reports the WTS index of the rotor blades as a function of NWF. When the nozzle N1 is used (Figure 98-left) the rotor is much more sensitive to the injection conditions variations. Indeed, apart from some blades in the bottom part of the rotor (rot09-rot14) showing small WTS variations (maximum 5.0%) with NWF, the other blades (rot01-rot08 and rot15-rot18) show more pronounced differences. This is due to the droplet dynamics in the considered configuration: most of the droplets injected are dragged toward the bottom part of the inlet case where much of them are

trapped; the few rest impact the top part of the inlet cone, eventually splash and then continue their path toward the rotor. Increasing the water flow rate results in a major number of splashed droplets on the top part of the cone (since the impact energy will be higher), leading to an increase of small droplets impacting the rotor blades. WTS in the top rotor region, therefore, sensitively increases with NWF. On the contrary, droplets concentrating in the bottom part of the casing undergoes less splashes, which means that their dynamic (and hence the WTS index for the bottom rotor blades) is less affected by the increase of the water flow rate. The relative velocity of the rotor makes the WTS distribution make asymmetrical along the rotor blades. To further increase the water mass flow rate, nozzle N2 should be adopted. As said, N2 presents a different injection cone, inlet velocity and droplets size distribution (resulting in a globally larger droplet inertia), and this leads to a less variable WTS behavior (Figure 98-right).

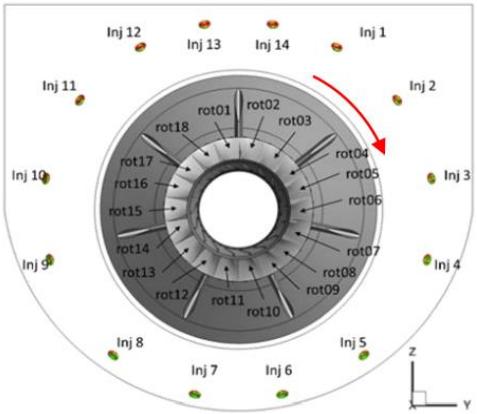

Figure 97. Reference names and potions of injectors and rotor blades [
[53]***. © 2021 Baker Hughes Company - All rights reserved***

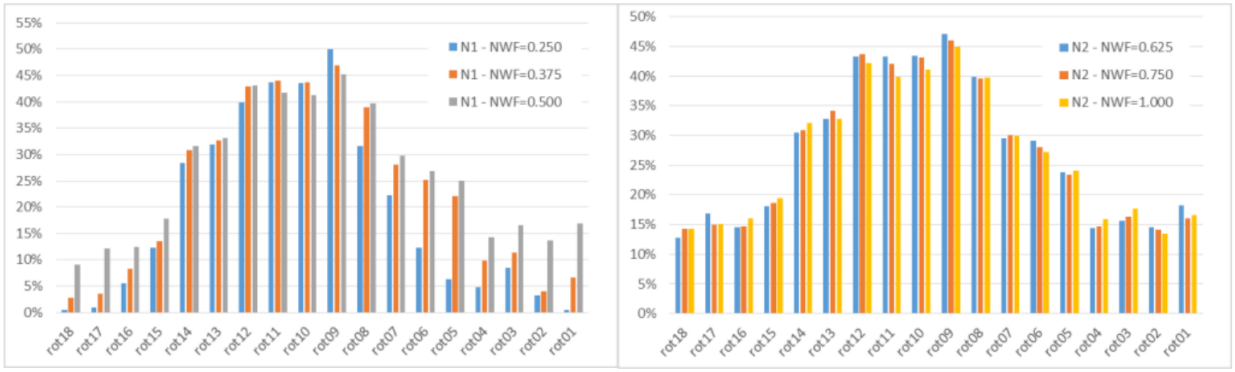

Figure 98. WTS of the rotor blades as a function of NWF. Left: nozzle N1; right: nozzle N2

It is worth noting that the different WTS values along the rotor blades are due to the frozen rotor approach adopted for the present case. Since the rotation speed of the rotor is very high (more than 7000 rpm), it is impossible to simulate the considered domain adopting a rotating mesh. For this reason, the frozen rotor approach was selected as the most appropriate for the present case. It follows that in real compressors, all rotor blades will have the same wetted surface, here assumed to be the maximum predicted by the simulations. Figure 99 shows the maximum WTS value as a function of NWF, predicted at blade rot09. What comes out from the figure is that the maximum of WTS decreases as NWF increases, even if passing from nozzle N1 to nozzle N2 the

variation range becomes less pronounced (from about 5% for N1 to about 2% for N2). This result seems in contradiction with what seen in Figure 95-top. However, Figure 95-top represents the whole rotor wet surface computed as sum of the wet surfaces of each blade, not considering that for some of the blades the wet surface could be the same.

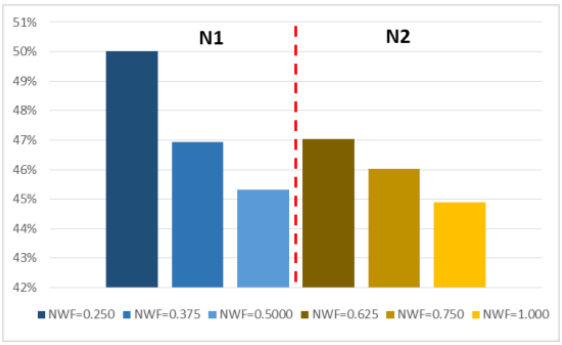

Figure 99. Maximum of WTS on rot09 as a function of NWF. Blue-scale bars: nozzle N1; Yellow-scale bars: nozzle N2

Figure 100 reports ITM and IMWS on the rotor blades for nozzles N1 an N2. ITM for nozzle N2 does not vary significantly as the NWF increases. On the contrary, N1 nozzle shows some more evident variations, especially for blades rot11-rot14 and rot08. IMWS variations are evident in both the nozzles: in N1 nozzle, variations are concentrated on blades rot08-rot10, showing a strong increase of the IMWS index with NWF. Using N2 nozzle results in some slightly larger variations in a wider range of blades (namely rot08-rot12).

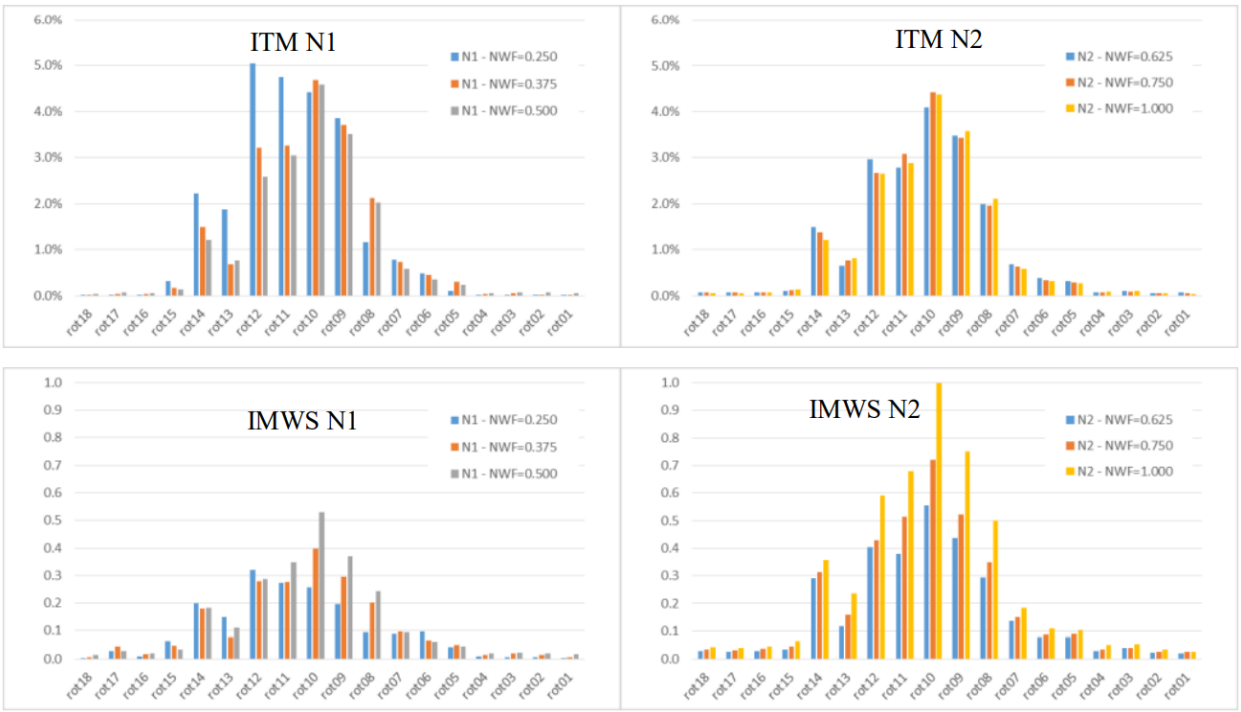

Figure 100. ITM (top) and IMWS (bottom) of the rotor blades as a function of NWF. Left: nozzle N1; right: nozzle N2

In Figure 98 and Figure 101 it is worth noticing that for all the NWF values maximum of WTS is predicted on blade rot09, while maximum of ITM and IMWS are always on rot10 (apart from

NWF=0.250, for which the maxima are on rot12). Anyway, as a general trend in the present configuration the bottom part of the rotor is the most critical from the erosion risk point of view but also the mostly washed. Figure 101 shows ITM and IMWS on rot10, where their maxima are predicted. ITM index (Figure 101-left) shows a very weak decrease as NWF increases, so that it can be considered constant with NWF. On the contrary, IMWS shows a larger variation and a clear trend, continuously increasing with NWF from 0.3 to 1.0.

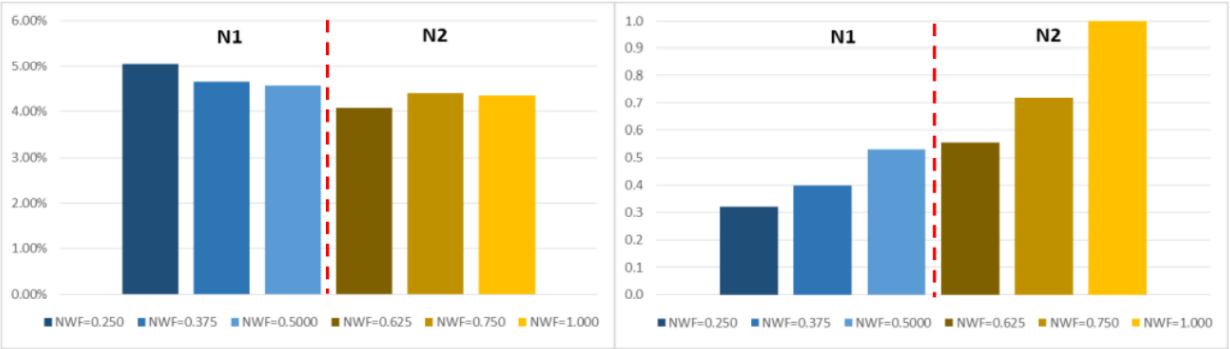

Figure 101. Maximum of ITM (left) and IMWS (right) on rot10 as a function of NWF. Blue-scale bars: nozzle N1; Yellow-scale bars: nozzle N2

7.2.2. Erosion prediction

What was extendedly discussed in the previous paragraph by analyzing water washing indices, can be now visually seen in the contour plots here presented.

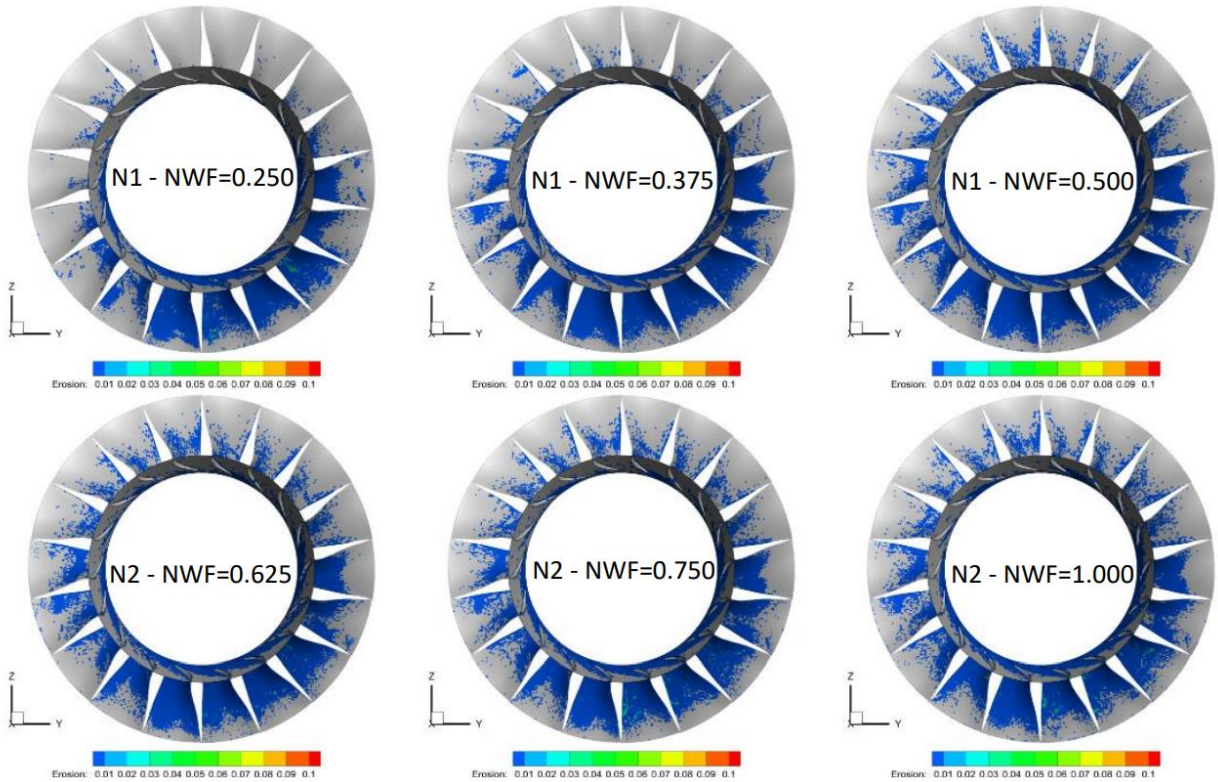

Figure 102. Erosion profiles predicted on the rotor blades pressure sides for the set of simulations here analysed. The values of erosion are normalized by the maximum recorded for every case, but the legend contour varies between 0 and 0.1 to make the levels differences more evident. © 2021 Baker Hughes Company - All rights reserved

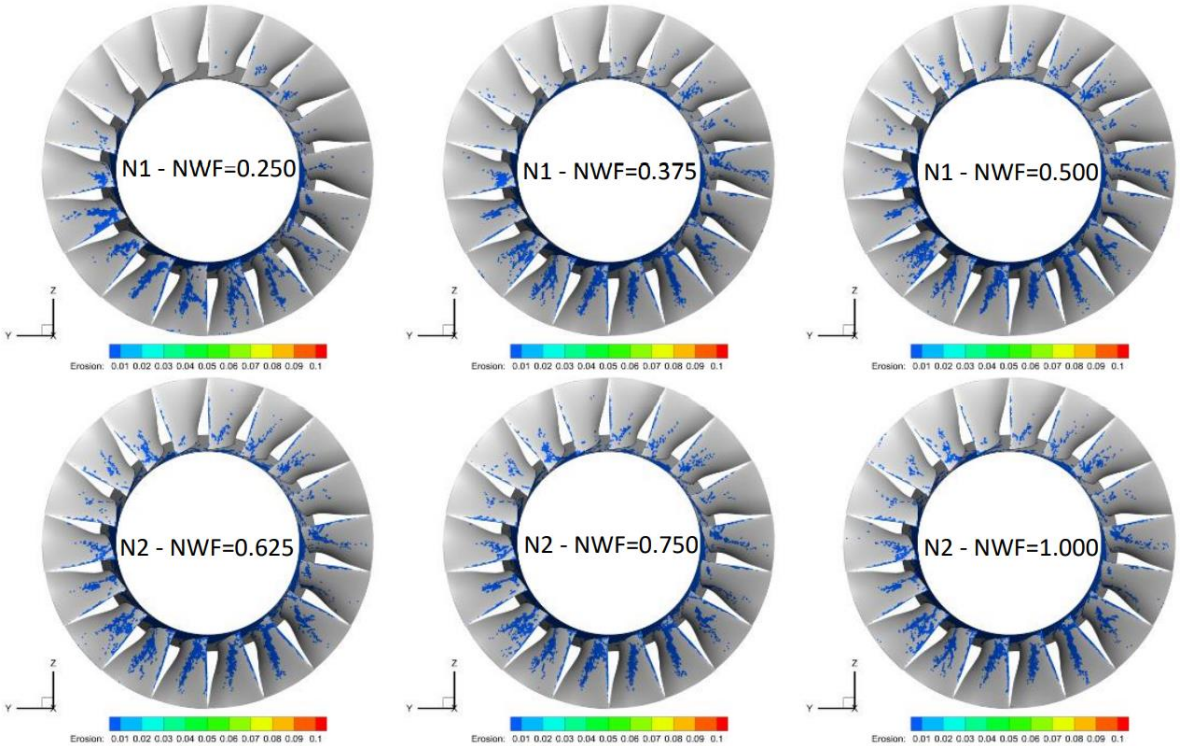

Figure 103. Erosion profiles predicted on the rotor blades suction sides for the set of simulations here analysed. The same procedure to normalize the erosion explained in Fig. 12 is here adopted. © 2021 Baker Hughes Company - All rights reserved

In Figure 102 and in Figure 103 the erosion profiles on the rotor are shown for blades pressure and suction sides, respectively. For both the sides of the blades, more evident differences can be observed in the erosion profiles when increasing the NWF in the N1 nozzle. Focusing on the erosion profiles reported on the pressure sides (Figure 102), the low-right blades (from rot06 to rot12) present very similar erosion distributions from a qualitative point of view. All the other blades show always larger eroded regions on the pressure side by increasing the NWF. It is worth noticing that, for the set of simulations here analyzed, the tip of the blades remains not eroded since most of the droplets impacts occur in the lower part of the blades. The blades suction sides (Figure 103) are in general less affected than the pressure sides. This is also due to the rotational effect, which pushes the droplets entering the rotor towards the blades pressure sides. Only the droplets with higher inertia will maintain their relative motion towards the blades suction sides. On these blade sides, some strips in the erosion contour are evident for the whole set of simulations here assessed. This might be due to the position coupling between the IGVs and the rotor blades. In most of the configurations analyzed in the present work, the rot09 is found to be the blade where the erosion peak was detected. For this reason, in Figure 104, the erosion profiles on the pressure sides of this blade are shown by varying the NWF. Most of the rot09 pressure side is subject to erosion for all the NWF here assessed. For the last two simulations (NWF=0.750 and NWF=1.000), more pronounced material removal is observed around the blade mid-span region. In Figure 104, the erosion contour has been normalized by the maximum erosion value found in the whole domain of each simulation. Hence, not quantitative comparison can be made by watching uniquely at the contour plots. For this reason, in Table 23 the values of

the erosion peaks detected for each configuration is reported. The values have been normalized with respect to the maximum of erosion found in the whole set of simulation that resulted to be, as expected, in the case where the larger quantity of mass was injected, i.e. NWF=1.000. This is the worst configuration from the erosion risk point of view. By recalling Table 22 where the main features of each injection were summarized, one could point out that the flow rate per nozzle and the injection velocity (which are the highest in the configuration at NWF=1.000) play a major role in the erosion phenomenon in comparison with the spray angle and the droplets size. In fact the larger the spray angle, the higher will be the dispersion of the injected droplets that will impact in wider regions, resulting in an erosion more widespread but with lower peaks. Indeed, for each nozzle by increasing the NWF, the larger droplets dimension diminishes which should result in less erosive impacts. Nevertheless, data reported in Table 23 suggests that the erosion peak increases with the NWF. It is also worth observing that the trend of the erosion peaks with the NWF is similar to the IMWS index reported in (Figure 101-right) which is confirmed to be a useful parameter to evaluate the erosion risk associated to water washing systems.

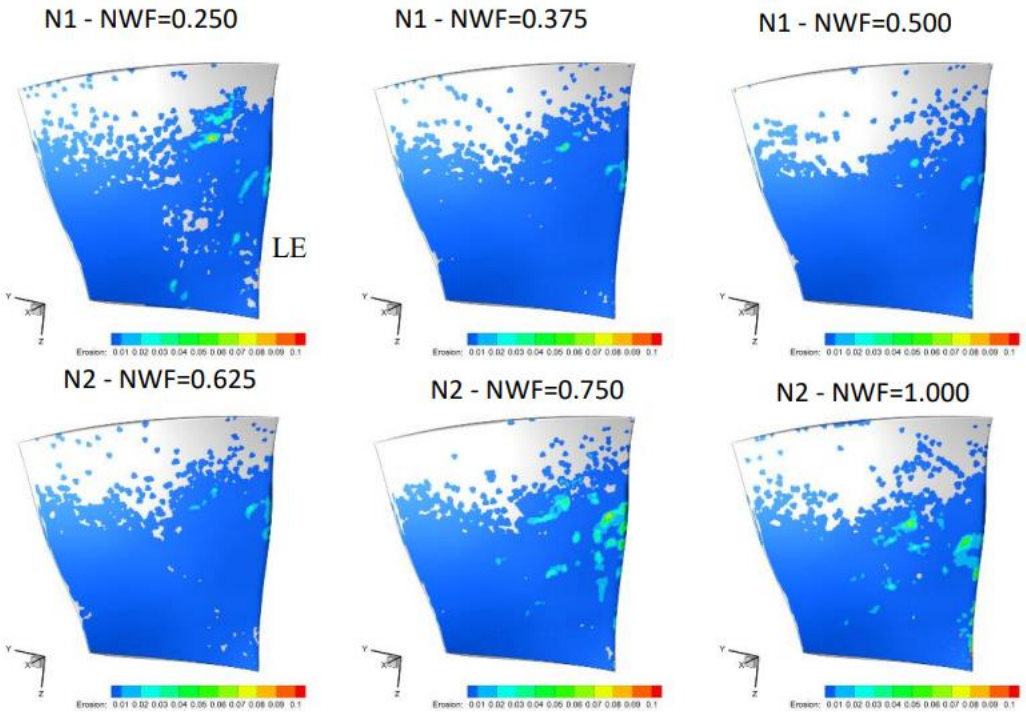

Figure 104. Erosion profiles predicted on rot08 pressure sides for the set of simulations here analysed. © 2021 Baker Hughes Company - All rights reserved

Table 23. Normalized Erosion Peak

Nozzle	**N1**			**N2**		
NWF	0.250	0.375	0.500	0.625	0.750	1.000
Erosion Peak	0.28	0.36	0.38	0.51	0.75	1.00

However, the presence of an erosion peak on a blade does not mean that it is the most eroded. Considering the volume of removed material (Figure 105), computed as integral over the blade surface of the erosion thickness, it comes out that rot10 (and not rot09) is the one having a larger

material removal for all the NWFs apart from NWF=0.250. In this latter case, the most eroded blade is rot09. This is a further confirmation of the capability of the considered indices to predict the erosion risk due to a given configuration.

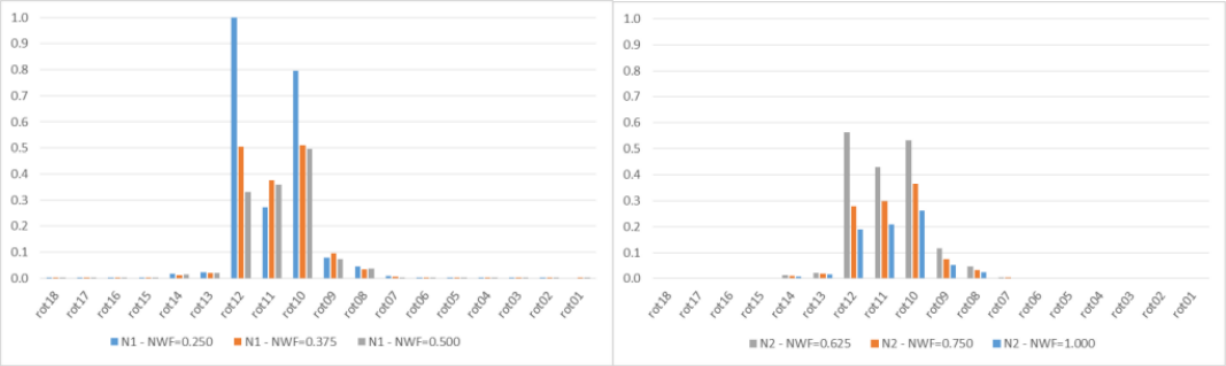

Figure 105. Normalized volume removed from the blades as a function of NWF. Nozzle N1: left; nozzle N2: right

In conclusion, in Table 24 the correlations between the indices considered and the main erosion-related quantities are summarized. It is evident that the proposed indices can predict the erosion risk of different water washing configurations. In particular, the WTS index and the Erosion peak seem to have a correlation that will be further explored in the future. An even stronger correlation is found between the mass indices ITM-IMWS and the eroded volume. In this case, in fact, the blades containing the maximum values of ITM and IMWS are the same (apart from one) of those having the larger eroded volume. Therefore, the use of such indices can be considered as a valid tool not only to estimate the water washing efficiency but also to compare the erosion risk of different configurations.

Table 24. Rotor blades containing the maximum values of the water washing efficiency indices and the main erosion quantities as a function of the NWF

Nozzle	NWF	WTS	ITM	IMWS	Erosion peak	Eroded volume
N1	0.250	Rot09	Rot12	Rot12	Rot08	Rot12
	0.375	Rot09	Rot10	Rot10	Rot09	Rot10
	0.500	Rot09	Rot10	Rot10	Rot09	Rot10
N2	0.625	Rot09	Rot10	Rot10	Rot09	Rot12
	0.750	Rot09	Rot10	Rot10	Rot08	Rot10
	1.000	Rot09	Rot10	Rot10	Rot09	Rot10

Chapter 8

Comparative life cycle assessment of different gas turbine axial compressor water washing systems

Reproduced in part from: I. Dominizi, S. Gabriele, A. Serra, D. Borello, 2020, *Comparative Life Cycle Assessment of different Gas Turbine Axial Compressor Water Washing Systems*, Proceedings of the ASME Turbo Expo 2020, paper no. GT2020-15206

In this Chapter an Environmental Life Cycle Assessment (ELCA) is performed to evaluate the environmental impact of an improved cleaning efficiency system. Based on actual field data, the GT performances are evaluated before and after the introduction of the on-line washing system and the effects on the carbon footprint have been assessed.

8.1. Off-line water wash procedure

The most common approach to the gas turbine axial compressor cleaning is the so-called “off-line water wash”. Through this process, most of the fouling deposited on the compressor vanes is removed while the machine is running in crank. Although safe and effective, the process needs up to 24 hours of gas turbine downtime, with consequent production losses.
One off-line cleaning cycle requires a solution composed by 1/3 of cleaning solution and 2/3 of rinsing water. The cleaning solution is injected for a suitable time suggested by the manufacturer. After that period, the engine is rinsed to remove cleaning solution residues. It is generally suggested to wash and rinse the compressor twice. The temperature of the injected water is recommended to be from 38°C to 65°C [12], if ambient temperature is lower than 10°C, an antifreeze solution is needed [12].

8.2. On-line water wash procedure

With respect to the off-line water wash, the on-line water wash is activated while machine is operating at base load with no needed to shut-off the engine. Two different options of on-line water washing are available: the standard “low flow” and the innovative “high flow” here proposed.
One on-line cleaning cycle requires a certain amount of water injected for a suitable period specified by manufactured. The temperature of the injected water is from 60°C to 65°C and even in this case, if the ambient temperature is lower than 10°C, an antifreeze solution is required [12].

The high flow on-line water washing system is a new methodology for axial compressor cleaning. It has been tested for offshore/marine applications, where the large part of fouling deposits consists of salt. It can be operated every day for a few minutes. Tests performed on GT engines show that by increasing the on-line water flow rate, the power recovered after fouling and cleaning the axial compressor is above 90% [15] [5] [54] .

8.3. Effectiveness of the water washing procedures

Considering the Remote Monitoring Data (RMD) of a medium size Gas Turbine (GT) operated at base load, the load percentage over the fired hours is shown in red (Figure 106). As shown in Figure 106, after 2000 hours of operation, the compressor performance is strongly reduced, heavily affecting the overall GT performance. Performing the off-line washing, the percentage of load recovered (blue line) can reach up to ˜6% with a very small reduction with respect to the initial efficiency. However, between two successive off-line washings, the fuel consumption increases as well as the emissions [55] [56].
To maintain the compressor efficiency as high as possible, aiming at following the green lines in Figure 106, the new high flow on-line water washing system is repeatedly activated daily. The green lines represent the efficiency curves that are expected by assuming an on-line water wash increasing effectiveness of 90%, 95%, 100%. The green continuous line (100%) indicates the no recoverable part of the losses due to other aging effects (e.g. erosion leading to profile losses). With an 100% effective high flow on-line washing, there would be no further benefit given by off-line washings.

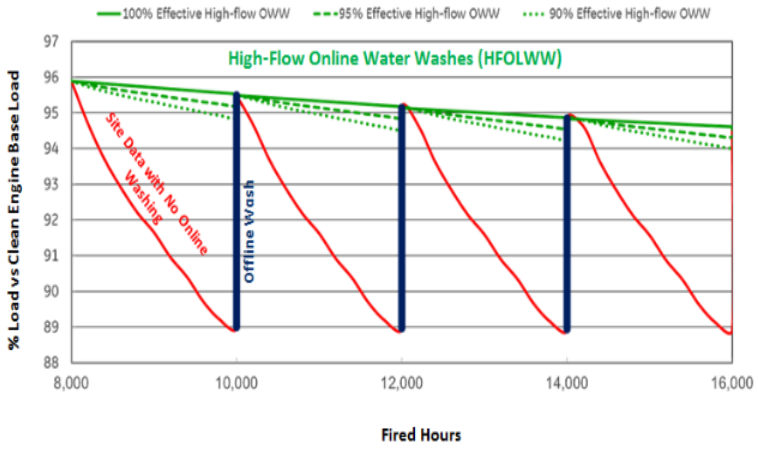

Figure 106: GT Degradation Curve. *[12]* **© 2020 Baker Hughes Company - All rights reserved.**

8.4. Description of the Life Cycle Assessment Analyses

In this chapter, the assessment of CO_2 emissions and environmental issues related to water washing procedures is presented. To this end, it is needed to perform Life Cycle Assessment focusing on the two kind of water washing systems here considered: Off-line (OWW) and High Flow On-line (HFOLWW) Water Washing. Analysis refers to an offshore plant that can work in both configurations. Real data received have been compared before and after the installation of the new HFOLWW skid, to evaluate the CO_2 emission due the type of water washing used. The time frame considered ranges about 3 months, which is the period from two consecutive OWWs. In

the first 3 months interval, only OWW process was available, while in the second interval both OWW and HFOLWW systems were carried out.
The LCA analysis [57] was split up in two parts: the first refers to water washing systems operation itself, and the second to its influence on the gas turbine operation. In the first part of the study, SimaPro software has been used to analyse the OWW and HFOLWW skids operation by evaluating the water and energy consumed in the given time frame. In the second part, in the same time frame, the gas turbine operation has been analysed with reference to:

- Field data collection before and after the introduction of the HFOLWW system
- Data filtering and calculation of CO2 emission by the evaluation of the amount of fuel used
- Data filtered refer to a specific GT operating condition to have data comparable

8.5. Life Cycle Assessment

In recent years, sustainability issues are becoming a relevant part of the design of new products. Life Cycle Assessment is a quantitative tool widely used to determine the environmental benefits and potential impacts of a given product or technology.
In 2012, Sloan reported a survey among of several managers declaring that 70% of them state that sustainability is an argument present in the agenda of their corporation [58]. Then sustainability is imposing itself as a resource for innovation and increase competitiveness rather than a tool for cost shrinking.
An LCA perspective considers the entire life cycle of a product, from raw material extraction and acquisition, to material processing and product manufacturing, distribution, use and end of life treatment. Through this global vision, a potential environmental load can be shift from one phase of the life cycle to another, or it can be shift from a process to another.

Figure 107: Life Cycle *[59]*

The steps of LCA include:

- **Raw Material Extraction Phase**: raw materials are extracted from their environment
- **Raw Material Processing Phase**: extracted raw materials are processed into other used to produce products
- **Product Manufacturing Phase**: products are manufactured and/or assembled
- **Distribution Phase**: products are packaged and transported
- **Use Phase**: products are used consuming other materials (paper, electricity, water, etc.)
- **End of Life Phase**: products are disposed (recycling, landfill, incineration, etc.)

The International Organization for Standardization (ISO) provides guidelines for conducting an LCA within the series ISO 14040 (Principles and Frameworks [60] and 14044 (Requirements and Guidelines [59]).
The most important aspect of an ISO standard is the need for careful documentation to avoid interpretation problems. There is no single way to perform an LCA analysis, the important aspect is to carefully document the entire procedure.

The LCA procedure includes the following four steps:

- Definition of the goal and scope of the study
- Inventory analysis, making a model of the process life cycle with all the necessary inputs and outputs
- Impact assessment, understanding the environmental relevance of all the inputs and outputs
- Analysis and interpretation of the study

The LCA is based on process/technology modelling. A specific challenge of such activity is to be able to develop a model in close agreement with the reality.

8.6. Methodology

Scope of this work is the application of LCA methodology to the two above mentioned water washing axial compressor systems of an industrial gas turbine. GT are typically used for generator drive in industrial power generation and for mechanical drive for production units. Comparison of different water washing processes will be presented to draw conclusion. The impact of OWW will be compared with a new type of water washing system (HFOLWW) in terms of process optimization and environmental impact assessment.
In SimaPro there are several impact assessment methods.

All the methods have the same structure:

1. **Characterization**: the substances that are part of an impact category are multiplied by a characterization factor that expresses the relative contribution of the substance.
2. **Damage assessment**: all the impact category indicators are combined into a damage category. The impact category indicators with a common unit can be added. For example, all impact categories that refer to human health are expressed in DALY (disability adjusted life years). All the substances that could cause disability, are added into category Human Health.
3. **Normalization**: the impact category is divided by the reference. A kind of reference could be the average yearly environmental load in a country or continent, divided by the number of inhabitants. The choice of reference is free. It can be useful to communicate the results obtained to non-expert people of LCA. In SimaPro there are a set of references available. After normalization all the impact category indicators have the same unit, which makes it easier to compare them.

4. **Weighting**: not all the methods have this step. The results of the previous step are multiplied by the weighting factors and are added together to create single score. Also, in this case, in SimaPro there are a set of weighting factor available.

The inputs that have been considered in the present LCA analysis are:

- Amount of water
- Energy used for auxiliaries skid (e.g. pump drive)
- Energy consumption heaters, because the water must reach a temperature of 65°C [12]
- Detergent solution for Off-line water wash

Two method have been used: ReCiPe2016 and IPCC2013.

8.6.1. ReCiPe2016

In ReCiPe 2016 there are both midpoint (problem oriented) and endpoint (damage oriented) impact categories, available for three different perspectives (individualist (I), hierarchist (H), and egalitarian (E)). There are a sets of impact category with sets of characterization factors. At the midpoint level, 18 impact categories are addressed [61]. Summary of the midpoint impact categories is reported in Figure 108.

At the endpoint level, every of these impact categories are multiplied by a damage factor (specific for each categories) and added up in three endpoints:

- Human Health
- Ecosystems
- Resources scarcity

These last categories are strictly linked to the three pillars of sustainability: environmental, economic and social pillars [61], [62].

Environmental mechanisms and damage models have uncertainty, modelling has a certain level of incompleteness and uncertainty. In ReCiPe 2016 it was decided to group different sources of uncertainty and different (value) choices into a limited number of perspectives or scenarios, according to the “Cultural Theory” by Thompson 1990V [63].

There are three different perspective:

- **Individualist** (I): it is based on short-term interest and the most popular types of impact;
- **Hierarchist** (H): it is based on the most common political principles regarding timing and other issues.
- **Egalitarian** (E): is the most precautionary perspective, takes into consideration the longest time interval, types of impact not yet fully established but with some indications.

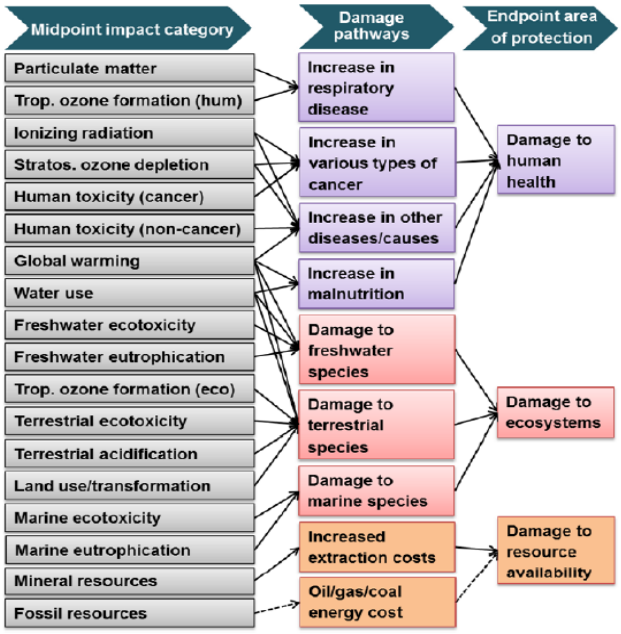

Figure 108: Relations Between the Impact Categories Midpoint and The Areas of Protection (Endpoint) [62].

These perspectives are used to group similar types of hypotheses and choices. The endpoint characterization factors used in ReCiPe can be described as follows [64]:

- **Human Health**: it is expressed as the number of year life lost and the number of years lived with disability. These years are added up in Disability Adjusted Life Years (DALYs). The unit is years
- **Ecosystems**: expressed as the loss of species over a certain area, during a certain time. The unit is species.yr
- **Resources**: expressed as the surplus costs of future resource production over an infinitive timeframe (assuming constant annual production), considering a 3% discount rate. The unit is USD2013. Mind that fossil resource scarcity does not have constant mid-to-endpoint factor but individual factors for each substance [62].

In the last step, all the values are summarized in the Single Score, that is the output of this method, a universal measure unit (Pt) that permit to compare different SimaPro practitioners' analyses.

8.6.2. Carbon footprint IPCC2013

IPCC is another SimaPro method, developed by the Intergovernmental Panel on Climate Change and permits to evaluate the airborne emission [65]. It is related only to emissions of greenhouse gases to air and consider the global warming potential of each of it. The main GHG in atmosphere are listed below:

- Water vapor (H_2O)
- Carbon dioxide (CO_2)
- Methane (CH_4)
- Nitrous oxide (N_2O)
- Ozone (O_3)

The result of this kind of analysis is expressed in kilograms of carbon dioxide equivalent $kgCO_2eq$. Every GHG is compared to CO_2 emission, in one value all the GHG air emission contribution [66] can be found. Climate change can have negative effects on human health, the ecosystem and resources. Factors are expressed as Global Warming Potential for time horizon 100 years (GWP100), in kg carbon dioxide/kg emission. The geographic scope of this indicator is at global scale. IPCC 2013 is an update of the method IPCC 2007 developed by the International Panel on Climate Change. This method lists the climate change factors of IPCC with a timeframe of 20 and 100 years [66]. In the CO2eq are added all the contribution of greenhouse gas, with some exceptions:

- Exclusion of the formation of dinitrogen monoxide from nitrogen emissions
- Exclusion of the radiative forcing due to water, sulphate, NOx, etc. in the lower stratosphere and upper troposphere
- Exclusion of the formation of CO2 from CO emissions

It is a widely used indicator for the evaluation of the carbon footprint.

8.7. Operation analysis

To quantify the benefits gained from the use of the high flow on-line water washing, data of water washing skids and GT operation have been analysed before and after the introduction of the HFOLWW system. A summary of the LCA drivers is reported below and shown in Table 25:

- Water washing system operation. Main parameters for the LCA are the utilities necessary to the water washing skids: the amount of demineralized water and detergent needed per washing cycle, as well as the energy needed to activate auxiliaries per washing cycle (i.e. pump and heaters). Analysis has been performed adopting ReCiPe2016 and IPCC2013 methods
- Gas turbine operation. The main parameter for the LCA has been identified in GT fuel demand before and after the HFOLWW system introduction. To assess comparable gas turbine operating conditions, test data have been selected at the same GT power output, the same ambient conditions and the same Power Turbine speed
- As the CO_2 emissions are directly linked to fuel demand, the IPCC is the most immediate method for the LCA

***Table 25*: Drivers of LCA© 2020 Baker Hughes Company - All rights reserved.**

Water Washing System Operation LCA		
Drivers	**Before HFOLWW**	**After HFOLWW**
Demi Water	800L	c.a. 20000L in 3 months
Detergent	200L	200L (only for off-line)
Energy	~ 50kWh per cycle	~ 50kWh per cycle
Frequency in 3 months	1 off-line cycle	1off-line cycle + 92 HF cycles
Gas Turbine Operation LCA		
Drivers	**Before HFOLWW**	**After HFOLWW**
Fuel Composition	Natural Gas	Natural Gas
Fuel Demand	Measured Data	Measured Data

All the assessments have been carried out in the period between two consecutive off-line washings, that approximately correspond to three months of engine operation, considering the same value of axial compressor efficiency as starting point. In this time frame, 1 cycle of off-line water washing has been considered for the first assessment, 1 cycle of off-line wash + daily high flow on-line water wash has been considered for the second assessment.

Two methods have been used for the system operation's life cycle assessment, the ReCiPe2016 and IPCC2013, while only the IPCC method has been used to analyze the environmental impact of a gas turbine operation.

As mentioned before (Figure 108), IPCC characterizes the climate change factor category by evaluating airborne emissions only. This category is one of the different midpoint characterization factors in the ReCiPe method.

When considering a carbon dioxide intensive system like a Gas turbine, the airborne emissions are dominant with respect to the other ReCiPe midpoints. For this reason, in this case the two methods show comparable results and thus only one can been selected.

8.7.1. Water Washing System Operation: ReCiPe2016

In the characterization phase, namely the first step of the ReCiPe analysis, the impact categories at the midpoint level are evaluated for both the off-line and the high flow on-line water washing processes.

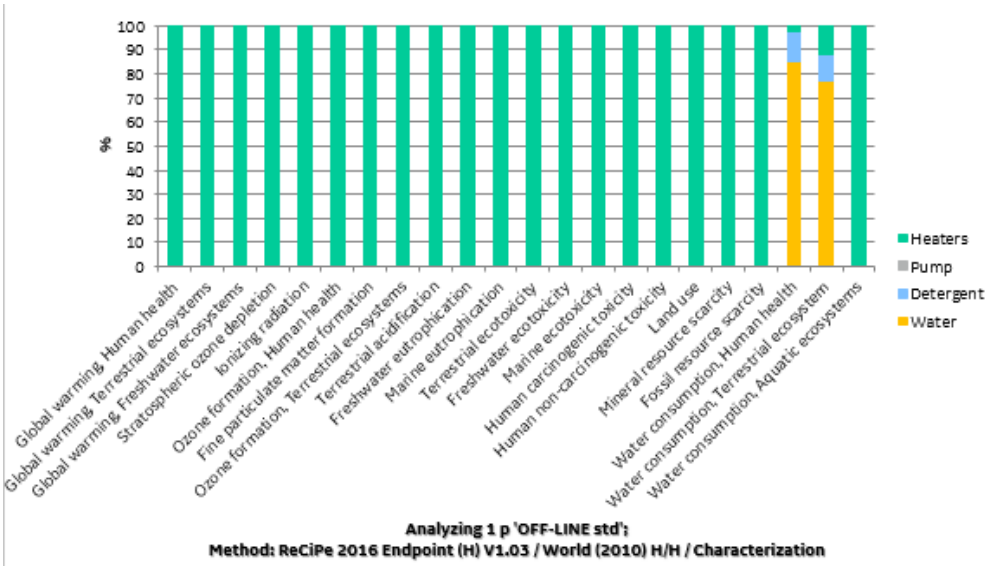

Figure 109: Midpoint Impact Category, OWW. ***© 2020 Baker Hughes Company - All rights reserved.***

In Figure 109 the result for the off-line water washing is shown. In most of the categories, the major impact on the environment is caused by the energy required to heat water tanks and to maintain water temperature. In addition, the impact of water heating is amplified as the source of energy is supplied by gas turbines and thus produced through fossil fuels. However, in two categories most of the effects are related to water and detergent consumption due to their impact on the human and ecosystems health.

Similar qualitative results are obtained when considering the HFOLWW process (Figure 110). As in the previous analysis, also in this case heating has the highest impact on most of the categories. The main difference between the two washing approaches lies in the larger use of utilities (mainly washing water) observed for the HFOLWW. This result is expected since the HFOLWW is performed daily in the reference period. The relative impacts of the water consumption are increased by almost 10% with respect to the off-line case. It is worth to notice that with HFOLWW no detergent is needed.

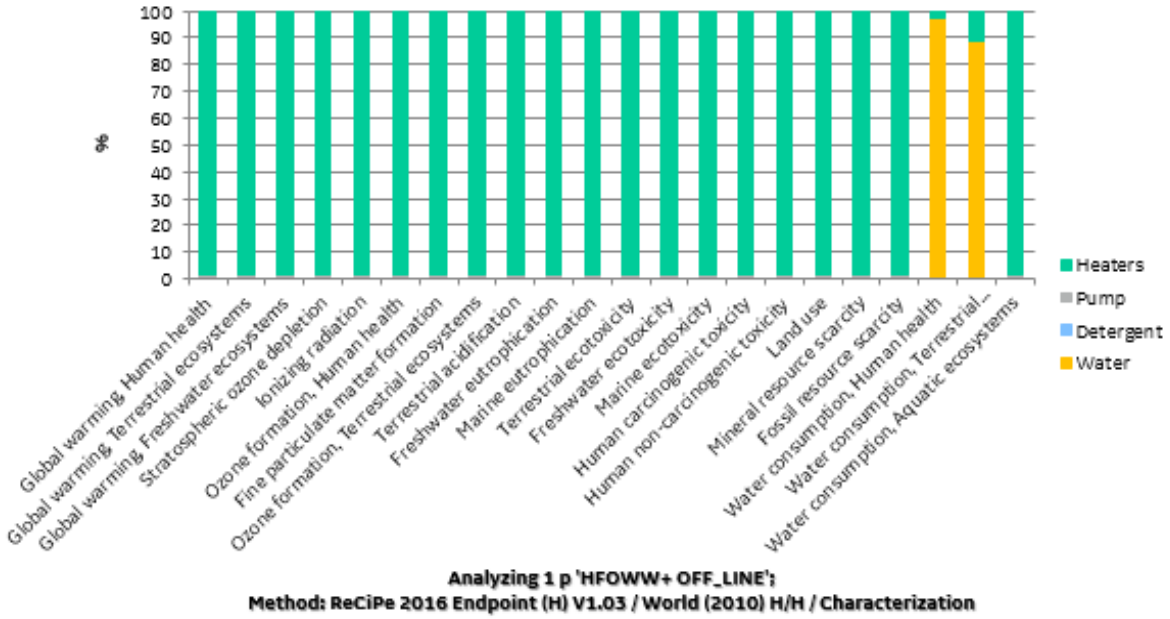

Figure 110: Midpoint Impact Category, HFOLWW Data. ***© 2020 Baker Hughes Company - All rights reserved.***

After the characterization phase, the damage assessment is performed. In this analysis the midpoint categories are converted into endpoint factors. Data are normalized and weighed, transformed into SimaPro units and added to the Single Score.

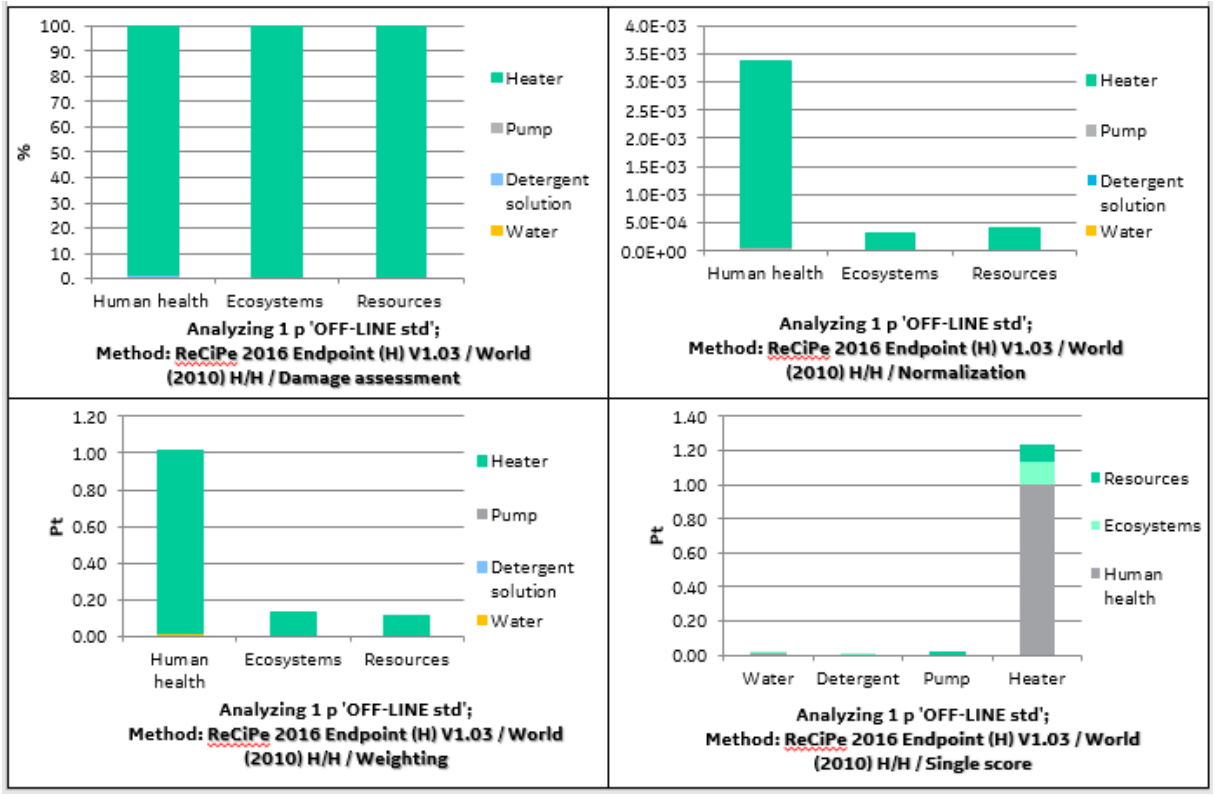

Figure 111: From Midpoint to Endpoint. Off-Line WW Data ***© 2020 Baker Hughes Company - All rights reserved***

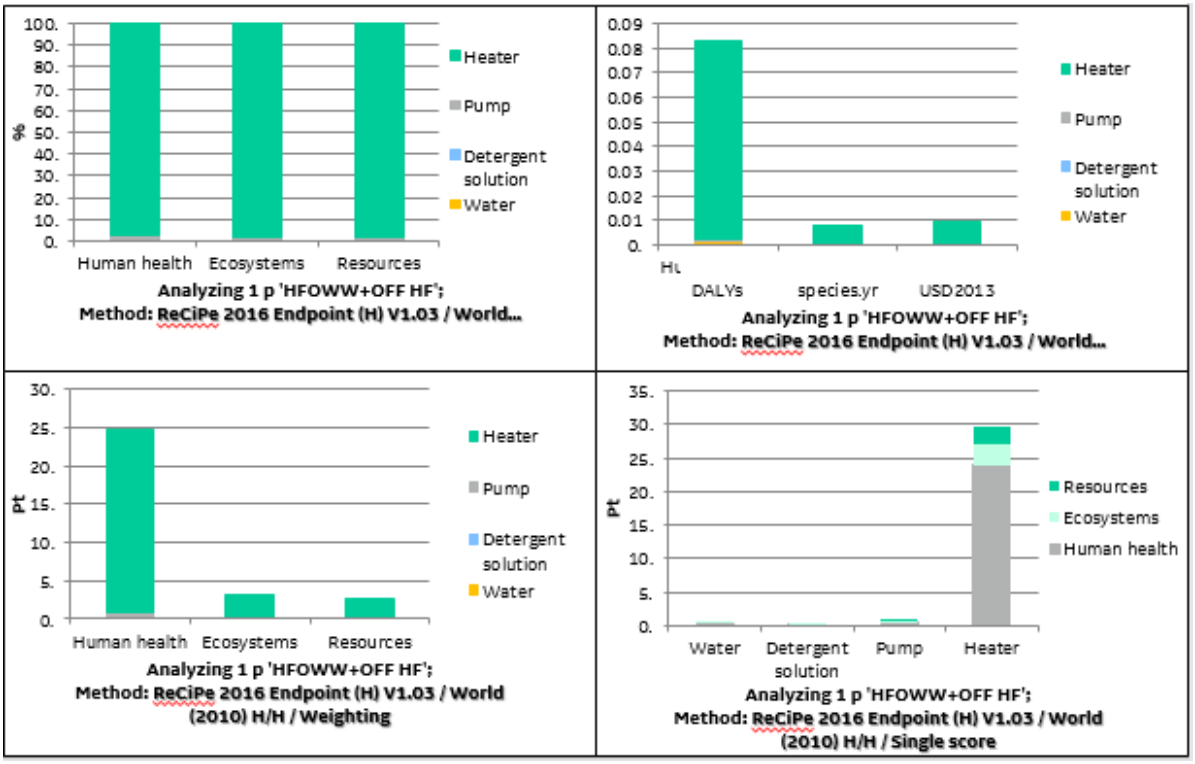

Figure 112: From Midpoint to Endpoint. HFOLWW Data. ***© 2020 Baker Hughes Company - All rights reserved***

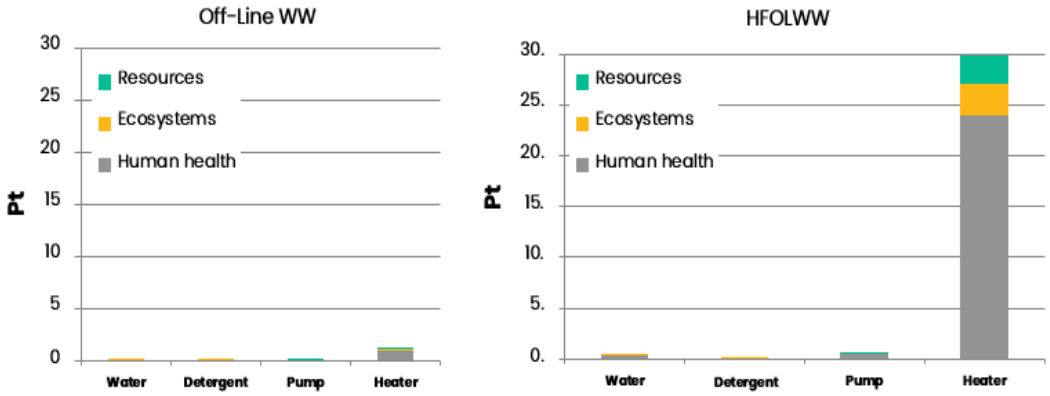

Figure 113: Single Score OFF-LINE VS HFOLWW. ***© 2020 Baker Hughes Company - All rights reserved***

To assess the system operation in the reference period, the Single Scores of OWW and HFOLWW are compared. The environmental impact is roughly 10 times higher when using the HFOLWW with respect to the OWW due to the larger amount of energy used for the water heating. The impacts are mostly affecting the human health (24pts) with more contained effects on the resources (3pts) and ecosystems (3pts).

8.7.2. Water Washing Systems Operation: Carbon footprint IPCC

The carbon footprint related to the water washing systems operation is shown in Figure 114:

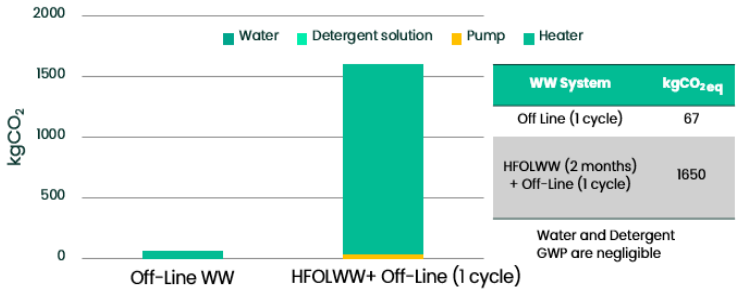

Figure 114: CO_2 Emissions Off-Line WW VS HFOLWW ***© 2020 Baker Hughes Company - All rights reserved.***

As expected, in the reference period, the CO2 emissions of the daily HFOLWW operation are larger with respect to a single cycle of OWW. In particular, the two systems emitted 1650kg of equivalent CO2 and ˜67kg of equivalent CO2, respectively. In agreement with the results of the ReCiPe, also the IPCC shows that the heaters have the largest impact.

8.7.3. Gas Turbine Operation: Carbon footprint IPCC

The two water washing systems may have a different impact on the gas turbine operation. From the literature the fuel mass flow consumption for a gas turbine is given by:

$$\dot{m} = \frac{P}{LHV * \eta}$$

where:
$\dot{m}$ = fuel mass flow
P = shaft power
LHV = Lower Heating Value
η = global efficiency

From eq. (1), if the output power and fuel (LHV) are fixed, an increment of global efficiency yields to a reduction of fuel mass flow and a consequent reduction of the CO2 emissions. For a given operating condition, the global efficiency of the gas turbine is strongly dependent on the axial compressor efficiency. Since the water washing acts by restoring the efficiency of a fouled axial compressor, its effects can be clearly measured through the reduction of fuel consumption (for a fixed output power).
To validate and compare the effectiveness of the two washing systems, the operation of a medium size gas turbine has been recorded for a period of 6 months. In the first 3 months the OWW has been tested then, in the following three months, the HFOLWW has been tested. Data have been filtered to have comparable operating condition before and after the introduction of the HFOLWW system. For the same machine, in the same application and same operating conditions (full speed full load), filters have been applied on shaft power, GT inlet temperature and on power turbine speed. About 450 samples have been considered to cover an operation period of 58days. The actual composition of the fuel gas burned in the GT has been considered in a combustion reaction model to determine the quantity of CO_2 emitted by the machine. Any misleading data has been removed to ensure that the CO_2 emissions reduction are attribute to the different washing systems, only. In Figure 115 the impact of the GT operation on CO_2 emissions is shown.

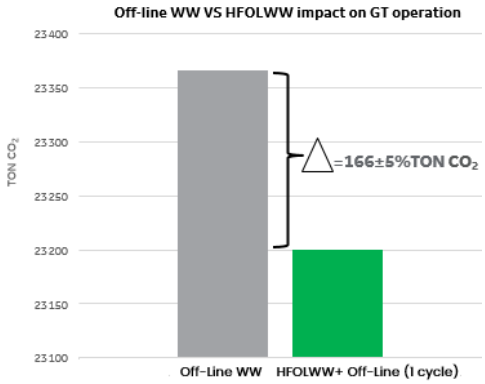

Figure 115: Normalized CO2 Gas Turbine Emissions. ***© 2020 Baker Hughes Company - All rights reserved.***

The reduction in fuel consumption yields to a reduction of about 166TON on CO_2 emissions in 58 days when using the HFOLWW system. Based on the measured data, it is possible to identify also the economic benefit associated to the use of the HFOLWW. Considering countries where a carbon tax is applied, the reduction of greenhouse gas emissions yields to an economic return. In this case, the 166 TON of pure CO_2 saved in 58 days correspond to about 190 TON of equivalent CO_2 saved in the same period; extending to 1 year of GT operation this leads to 1050 TON of pure CO_2 and 1200 TON of equivalent CO_2 saved. Considering an average carbon tax of 40€ for each TON of CO_2 emitted, the tax reduction associated to the emission reduction is evident. Moreover, the fuel saved becomes available for sale on market, bringing a double benefit.

8.8. Discussion

An innovative HFOLWW methodology was proposed and compared with standard configuration trough LCA.
When the behaviour of the whole gas turbine is analysed by summing up all the contributions for the two processes, it is observed that the new washing system gives clear benefits in terms of CO_2 emissions, although in the analysis of the system operation the impact of the HFOLWW is higher (Figure 115).
Giving a closer look to the results, it can be observed that:

- As can also be seen from the results of the analysis of the washing system, LCA shows that the highest impact is always attributed to the heaters, because these are powered by electricity produced on the offshore platform by GT. Then, as the HFOLWW uses much more water, the environmental performance is much worse than OWW. As a matter of fact, Recipe and IPCC gave comparable results, in both HFOLWW has a greater impact. Furthermore, in the Recipe it is observed that this impact weighs more on human health.
- In the second part (the whole GT operation analyses) the data analysis shows that the introduction of the HFOLWW, led to a reduction in fuel consumption and consequently a reduction of CO2 emission in atmosphere. The latest results show that HFOLWW permits to decrease airborne emission. The impact of CO2 emissions reduction (in HFOLWW) is so high that system analysis is overshadowed. Therefore, the information obtained with IPCC can also be extended to the Recipe.

The comprehensive life cycle assessment of HFOLWW put in evidence the environmental and economic benefits of the procedure, allowing to quantify the impact in terms of costs and potential new incomes. This proves that LCA can be a proper tool for guiding the development of innovative design procedures and to support decision process in the management of the existing technologies.

Chapter 9

Conclusions

In this work, the water injection process in the AXial COmpressor (AXCO) of industrial Gas Turbines (GT) has been analysed to identify the benefits on the GT operation and the associated risks for GT and AXCO mechanical integrity.

The leading design parameters of the water injection system have been identified providing a design guideline for the optimized design and optimized operation of the water washing devices. The effects of the water washing have also been assessed in terms of carbon footprint reduction of a typical industrial GT.

To identify the effects of the water injection on the GT AXCO, a dedicated Water Droplets Erosion (WDE) model has been developed and assessed against the available models. The new model has been derived by analysing semi-empirical and experimental studies available in literature and defining the underpinning physical phenomena to be addressed for a comprehensive approach to WDE modelling. The new model keeps into account all the main relevant quantities affecting erosion process. In particular, it considers the impact angle, the impact velocity, the droplet size, and the initial surface roughness and hardness. Thanks to its experimental development and calibration, the predicted incubation period seems to be accurately estimated.

Considering the specific AXCO application, the development of the present WDE shows some clear advantages compared to the development of either the Springer's model and the Tabakoff's models. Springer's model does not account for surface roughness and hardness and it was developed for the erosion due to very large droplets impacting on non-metallic materials. Tabakoff's was developed for the prediction of solid particle erosion and not for liquid droplet erosion. By contrast the present model has been specifically developed for the prediction of liquid droplets erosion in turbomachines by using several sets of experimental data and a physical modelling based on the estimation of the energy transferred to the material during the impact. The new WDE demonstrated the ability to consider properly a wide class of droplets diameter and the roughness and the hardness of the blade surface, improving the accuracy with respect to the baseline models. Moreover a specific set of gas turbine AXCO materials have been considered, creating a physical based framework specifically tailored for this application.

In order to verify the accuracy of erosion prediction, the novel WDE has been used against the Springer model and the Tabakoff's model on a benchmark case of the water droplet erosion on the blade of a compressor cascade. The analyses have shown that both the Springer's and Tabakoff's models tend to overpredict the erosion. The main reasons for this behaviour may be ascribed to the different development of the two models: the former model was developed for large droplets (of the order of few mm), and wind turbine blades (usually made of epoxy resin);

the latter model was developed for solid particle erosion whose physics is different from that of liquid droplet erosions. Indeed, it was expected that the application of those models out of the range for which they were developed would result in an overestimation of the predicted erosion. Moreover, while the tested models provided a correct information about impact sites and accumulated energy, the estimation of the eroded material was very different, leading to significantly different results. This analysis has also highlighted how the water droplet erosion process depends on several factors, such as impact velocity and angle, droplet material, material of target surface (i.e., hardness and roughness), droplet size, position of nozzles, water to air mass fraction, thus it is extremely important consider all these aspects when simulating the process. The application of an accurate prediction model has also highlighted specific quantities related to the droplets erosion process like the zone of a surface more exposed to droplet impacts, the accumulated energy and the zones that may be more affected by erosion.

In order to reduce the number of variables to be considered in the performance and design space definition, a sensitivity analysis on the WDE leading parameters has been performed on simplified GT geometries through means of CFD simulations. The analysis performed consisted in a series of simulation where the expected leading parameters have ben varied. In order to quantify and measure the washing efficiency, in each series the accumulated energy, the wetted surface, and the capture efficiency have been quantified. Moreover the water droplet erosion, measured as the thickness of eroded material, has been quantified in order to evaluate the erosion risk of each operating condition.

From the simulations it emerged that the injection time, injection angle and injection velocity are the parameters leading the washing efficiency. The injector position can be optimized to better distribute the water droplets on the blade surface, while the droplet size distribution produced by the injection system affects the region of the blade reached by the water, thus it may increase the overall washing efficiency. To enhance the washing efficiency reducing the compressor performance detriment without exposing the blade to an excessive risk of erosion due to droplet impacts, the definition of a balance between all the injection parameters is of paramount importance.

Based on the results of the sensitivity analyses, the novel WDE has been applied on a real case where the complete geometry of a real GT has been considered form the inlet plenum up to the outlet of the first AXCO rotor.

Two different operative conditions, namely the off-line and on-line WW have been considered. The simulation results show that the injected droplets partially mix with the main flow, never reaching an homogeneous distribution upstream of the IGV. This indicates that the numerical analyses of the water washing effectiveness requires the simulation of the whole geometry without considering symmetry or periodicity assumptions. In the actual configuration, many of the injected particles impact on casing and inlet region, eventually generating liquid films that must be properly considered to avoid risks of water accumulation. The effect of droplet splashing has been shown to affect the droplet distribution prescribed when designing the injector, leading to a smaller average diameter of the droplets.

The rotor blades most exposed to droplets have been highlighted in the rotating case showing impacts only on the pressure side. By contrast, in the non-rotating case, the pressure side of the blades seems not to be the most affected by droplets impacts. From the washing efficiency prospective, this means that the on-line washing effectiveness is higher on the pressure side of the blades, covering about 20% of it, and depositing the highest amount of water among all the rotor blades. On the contrary, the erosion risk for this blade, evaluated by the accumulated to incubation energy ratio, is not the highest, therefore erosion is not expected to be extremely severe.

To quantify the efficiency of the water washing a set of parameters have been defined to evaluate the results of the simulations. The proposed indices were found to provide relevant information about the washing system and represents an useful prediction tool for assessing the water washing procedure in terms of number of injectors, water mass flow rate, to exploit washing capability as well as erosion growth rate. The following indices have been introduced: the Wet to Total Surface (WTS), defined as the percentage of a surface impacted by water droplets; the Impacted to Total water Mass (ITM), defined as the percentage of the impacted mass impacting a specific surface; the Impacted water Mass per unit of Wet Surface (IMWS), defined as the ratio between impact water mass and wet surface.

Based on the design and operations space highlighted through the simplified geometry analyses and based on the experimental verification of the model, a complete mapping of the water washing design and operation has been created using WTS, ITM and IMWS as means for the quantitative analyses. The main outcomes of the analysis are reported below:

- By increasing the Nozzle Water Flow rate (NWF) WTS always increases at the inlet of the domain while in the rotor it shows an asymptotic trend. NWF > 0.625 does not result in any relevant variation in the wet-surface index. By focusing on the impacted mass, in the rotor region a decreasing asymptotic trend of the ITM index with NWF is detected: by injecting with NWF>0.5 the ITM index stabilizes around a value of 25%. On the other side, on the rotor blades the normalized impacting water mass per unit surface (IMWS) constantly increases with NWF.
- Different patterns of wet surface are found for every single blade because of the use of the frozen rotor approach. The lower blades are in general the most affected by droplets impact but when using nozzle N1 the rotor is much more sensitive to the injection conditions variations which are found mainly on the top blades. These variations are associated to the splashing phenomenon which mainly occurs on the top part of the internal cone.
- When concentrating to the maximum WTS detected between the rotor blades (which is assumed to reproduce all the rotor blades behaviour in the real rotating situation) the WTS decreases as NWF increases. Even if the overall WTS increases along the full rotor surface, the larger spread of the water results in a lower WTS maximum.
- All the blades but the low-right ones show larger eroded regions on the pressure side by increasing the NWF. The tip of the blades remains not eroded since most of the droplet's impacts occur in the lower part of the blades. The blades suction sides are in general less affected by droplets impacts and by erosion phenomena.

- The cases where the larger quantity of mass was injected (i.e. NWF=1.000) were found to be those with higher erosion risk. The flow rate per nozzle and the injection velocity seem to play a major role in the erosion phenomenon in comparison with the spray angle and the droplets size. The increasing trend of the erosion peaks with the NWF is similar to the IMWS index which is confirmed to be a useful parameter to evaluate the erosion risk associated to water washing systems.

Together with the mapping of indices that define the water washing efficiency, the actual environmental impact and benefit of two practical water washing techniques have been assessed through an LCA analyses with Recipe and IPCC techniques. The High Flow On-Line Water Washing (HFOLWW) methodology has been evaluated in comparison with standard Off-line Water Washing (OWW) configuration. Considering the whole gas turbine by summing all the contributions for the two processes, it is observed that the new washing system gives clear benefits in terms of CO2 emissions, although in the analysis of the system operation the impact of the HFOLWW is higher. It can be observed that washing system, LCA shows that the highest impact is always attributed to the heaters, because these are powered by electricity produced on the offshore platform by GT. Then, as the HFOLWW uses much more water, the environmental performance is much worse than (OWW). As a matter of fact, Recipe and IPCC gave comparable results showing a greater impact for the HFOLWW. Furthermore, in the Recipe it is observed that this impact weighs more on human health. Considering the whole GT operation analyses, the data analysis shows that the introduction of the HFOLWW led to a reduction in fuel consumption and consequently a reduction of CO2 emission in atmosphere. The latest results show that HFOLWW permits to decrease airborne emission. The impact of CO2 emissions reduction (in HFOLWW) is so high that system analysis is overshadowed. Therefore, the information obtained with IPCC can also be extended to the Recipe.

The results mapping result of this work is currently being used to create a design tool for the design optimization of the water washing devices and a monitoring and diagnostic analytic to provide indications on the optimum settings of the water washing during operation. This analytic, will be able to provide real time guidance on the optimum water washing cycles, predicting GT efficiency recovery, highlighting mechanical integrity risks and, thanks to the LCA analyses and mapping, providing information on the resulting carbon footprint of the GT.

Appendix A.

Structural analysis of a gas turbine axial compressor blade eroded by online water washing

Reproduced in part from: R. Cinelli, G. Maggiani, S. Gabriele, A. Castorrini, G. Agati, F. Rispoli, 2020, *Structural analysis of a gas turbine axial compressor blade eroded by online water washing,* Proceedings of the ASME Turbo Expo 2020, paper no. GT2020-152

A.1. Introduction

Compressor fouling is the main cause of deterioration of GT performance [67]. The coupling of an adequate air filtering system and appropriate on-line and off-line washing regime is the most effective way of controlling and slowing down this deterioration. The off-line procedure involves shutting down the machine, leading to a production failure, and it is carried out while the compressor rotates at crank speed. The disadvantage here is the decommissioning of the machine. However, the washing efficiency is very high, and the power recovery is close to the original level. On the contrary, the online water washing (OLWW) takes place during the normal operation of the machine and is essential to keep the performance as constant as possible. Plus, this allows to extend the intervals between the stops necessary for offline washing and maintenance. However, with the online procedure the increase in performance decreases at each washing, and that is why both washing techniques are usually paired [55]. Nevertheless, one of the main problems due to OLWW is related to the long-term erosion of the first stage blades of the axial compressor, caused by the washing water droplets impacting the airfoil surface of the rotating compressor. The phenomenon of erosion leads to a deterioration of the blades, causing a reduction of the aerodynamic cord and fluid dynamic efficiency; from the mechanical point of view, the removal of material and the generation of cracks implies a decrease of the component fatigue resistance. Our goal is to qualitatively evaluate the role of erosion over the stresses and blade vibration, especially in the first stage of the compressor since it is the most impacted one.
It was decided to evaluate a high erosion depth to verify if the latter somehow affects the fatigue resistance of the structure. Moreover, the aim is to analyse the damaged component by means of the structural profile, and to evaluate the fatigue life at the end of its first operating cycle (Maintenance), to verify if the component would undergo any structural damage.
The analysis has been divided into the following steps:

1. Eroded geometry creation: starting from the results of the CFD simulations, the profile of the blade eroded by the impact of washing droplets is modelled through CAD Unigraphics NX.
2. Static structural analysis: evaluate the Von-Mises stress enforced onto the blade, caused by the external centrifugal and fluid-dynamic load and the corresponding deformations.
3. Modal analysis: evaluate the cyclic stresses due to the vibrations of the component during operation, when subjected to cyclic loads.
4. Fatigue analysis: assess fatigue strength and more solicited points, to check if there is a reduction in the mechanical properties of the eroded profiles by means of the Goodman diagram.

The creation of the eroded geometry requires the description of the eroded area on the blade surface. The numerical prediction of the erosion damage has been provided to us by the Sapienza University group, by carrying out the computational fluid dynamic (CFD) simulations using Fluent Ansys.
To develop a reliable fluid dynamic simulation and account for the erosion phenomenon, the water droplet erosion (WDE) model suitable for inox steel was implemented. The latter considers the droplet speed and diameter, impact angle, surface roughness and hardness influence over erosion. The new model [39] relates to the erosion phenomenon of Fig. 1, based on the experiments from Kirols [23]and Seleznev et al [25]. Different behaviours are identified, according to [23] and [25] an erosion curve is characterized by three zones:

I. An incubation period where surface roughness increases with no material loss (generation of micro-cracks)
II. A transitional period in which erosion rate increases reaching its maximum
III. A steady state period where there is a linear erosion trend and constant erosion rate

The erosion model implemented for the simulation, have been presented in Chapter 2.
The droplets were projected onto the mid-span of the blade surface, according to the CFD simulations it was suggested that erosion events concern the leading edge (LE) only. The simulation was carried out considering only the impact with water droplets, neglecting the contribution of solid particles and pitting corrosion phenomena. The simulation details are described in detail in [30]. The CFD run simulates the high flow online water washing HFOLWW, assuming it takes place once every day by injecting 200 liters of water. This washing protocol is the standard provided to our customers. The CFD simulation was carried out by injecting fluid from a single nozzle, however the results are reported below in terms of water injected globally on all the blades of the first stage rotor. The droplet size is a key parameter of the erosion phenomenon. Under the same water quantity injected the damage is enhanced by the droplet dimension, although the washing efficiency is increased. As usual in the engineering field this scenario requires a compromise between technological and economic considerations. In this analysis a washing characterized by a droplet diameter of 100μm has been simulated. An initial roughness of the surface to Ra=0.2μm and hardness to 336 HV have been set. Another

assumption is made on water, uniformly placed on the surface of the blade and not dispersing in the AXCO [25].

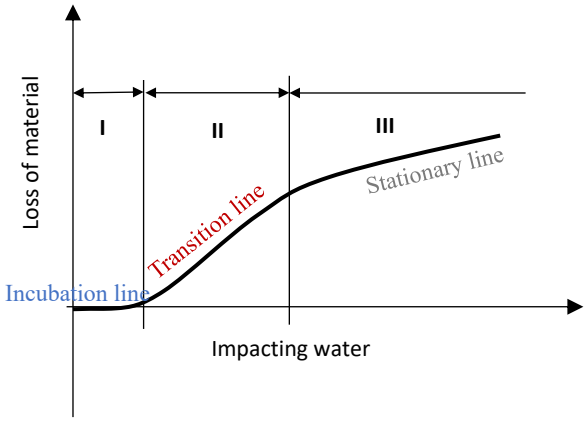

Figure 116. Erosion curve: incubation period (I), transition period (II), stationary period (III) [23].

A.2. Hypotheses and modelling

Aiming at evaluating a X mm erosion and the final value occurring after maintenance operation, starting from the single simulation data, it was deemed necessary to make use of some fluid-dynamic hypothesis. In fact, this work aims to develop exclusively a preliminary analysis by qualitatively evaluating the mechanical effect of erosion of the blades. The flow field and particle impact locations are supposed to change during the washing cycles, because of a variation in the eroded blade geometry.

In this case, the procedure for the creation of the eroded geometries requires a modelling according to the CFD outcome, recursively removing material. Hence a new CFD run must be performed, considering the new eroded points at each iteration, a new geometry is outlined and so on, in a recursive-wise procedure. The hours and erosion depth should be obtained through this step-by-step procedure. Rather than following this approach a conservative analysis has been performed, exploiting fluid dynamic hypotheses. The approximation could lead to over-estimated results. To produce a more complete analysis of the structural damage caused by the HFOLWW system it is our intention to design further experimental works to obtain better data to feed to the CFD simulations. Starting from the results of a single CFD performed, and wanting to evaluate the eroded profile at X mm and the eroded profile that one would have at the maintenance, the following fluid dynamic hypotheses were included:

1. During the simulation Zone III of Figure 116 where erosion is linear has been considered. This allows the erosion to be scaled with a chosen scale factor.
2. The subsequent cumulative washes are supposed to rely onto the baseline model. In this way the fluid dynamic field does not change, and the position of the eroded points always remains the one obtained from the simulation CFD.
3. The eroded points continue to lie exclusively on the LE, during the subsequent cumulated washings. Erosion occurs when the accumulated impact energy exceeds the incubation

energy (entering zone II of Figure 116). In all the remaining points outside the leading edge the accumulated impact energy is much lower compared to the incubation energy. It is hypothesized that this large gap remains the same for the subsequent cumulative washes. This strengthens the previous hypothesis 2: the eroded points remain the same.

Considering the eroded points on the LE obtained from the CFD simulation and increasing the erosion with a scaling factor, the accumulated washing hours and the erosion extent are highlighted in Table 26, in light of the two main objectives mentioned above. The single blade will undergo X mm of maximum depth of erosion after about 530 washing cycles by injecting globally more than 100,000 litres of water. This result, if the washing is carried out once a day, is reached after about a year and a half of operation. While up to the moment of maintenance, a maximum erosion of 2X mm corresponds, injecting about 200,000 litres of water into the complex, carrying out more than 1000 washing cycles. The washing and operational hours were computed with respect to the X mm of maximum erosion considered; reversing such a procedure the erosion extent of 2X mm was computed from the maintenance hours of operation.

This conjectural analysis concerning the washing fluid dynamic, frequency and time span must be thought of as a qualitative/predictive a priori step. The model referring to X mm of maximum erosion is named model 1, while the geometry referring to 2X mm of erosion is named model 2.

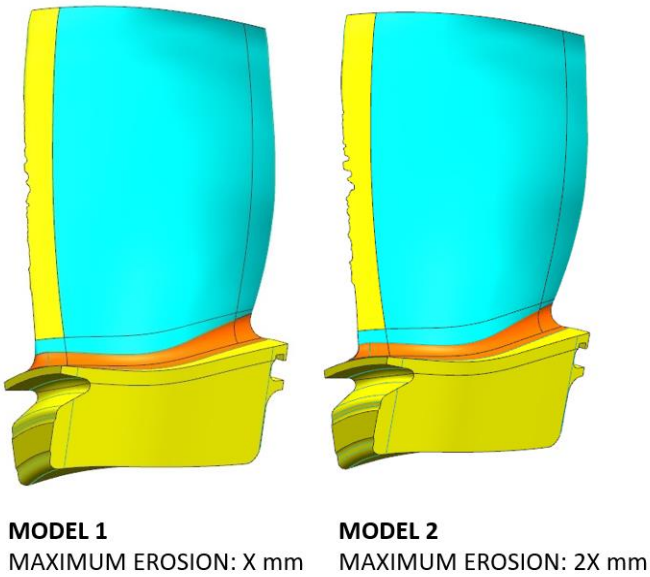

MODEL 1
MAXIMUM EROSION: X mm

MODEL 2
MAXIMUM EROSION: 2X mm

Figure 117. Eroded 3D profiles of the first stage rotor blade.
© 2020 Baker Hughes Company - All rights reserved.

Table 26. Results from the erosion data. © 2020 Baker Hughes Company - All rights reserved

Model	Maximum erosion	Liters of washing	Number of washes	Hours of operation
Model 1	X mm	100,000 L	530	12500 h
Model 2	2X mm	200,000 L	1018	Maintenance hours

A.3. Eroded geometry creation

Starting from the scaled trend of eroded points, shown in Figure 117, it has been proceeded with creation of the eroded geometry. Since in the CFD simulation the droplets have been launched only in the central part of the air foil the erosion is present between the 17% and 75% of the radial span and the maximum value around the 40%, as per Fig. 2 where the erosion values have been normalized as a function of the maximum value of the erosion depth shown in model 2, more eroded Field data, on blades subject to HFOLWW, showed a slight erosion even at the TIP and HUB of the leading edge, this is shown with a dotted line in the Figure 117. Field data have been combined with the eroded points obtained by the CFD. In this way the present erosion occurs along the whole radial span also including the fillet radius. The procedure for modelling eroded geometry involves the scale factor (SF) appraisal, and the scaling of the points in the normal direction to the surface on which they lie. In fact, the radial value is given by the extrapolation of the maximum erosion value of the LE, calculated in the CFD, and scaled by the SF [68]. These points are scaled in the normal direction to the surface on which they lie. Only the most eroded point is considered for each vertical profile and the selected points are connected through a spline that simulates the erosion envelope. This polyline has been transformed into a solid of revolution rotating around the axis of the blade in the range +/- 20°, with respect to the direction that connects axis and polyline, which enabled the eroded material to be cut and removed. Using this method, a smooth eroded profile has been obtained. Below are the two eroded models obtained, in Figure 118.

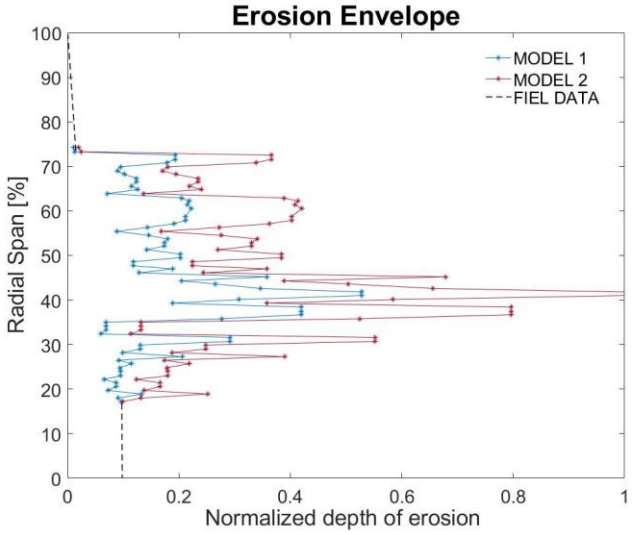

Figure 118. Erosion envelope: the points eroded in the function of the radial span of the LE and the selected mm are shown. The two models

report the same points eroded but scaled with different scaling factors (SF). © 2020 Baker Hughes Company - All rights reserved

A.4. Model development

To have a reference of comparison a clean baseline model has been analysed at first, then a structural FEM analysis on the eroded geometries has been performed. These analyses have been carried out using the ANSYS v.19.2 software. The first rotor wheel can be simplified by inserting the cyclic symmetry and considering only a single sector. To simplify further, the front and rear flanges are eliminated, through the evaluation of the cross section these have been replaced with the static constraints imposed at the base of the blade (see the Figure 119). The results obtained will be valid for the entire circular component.

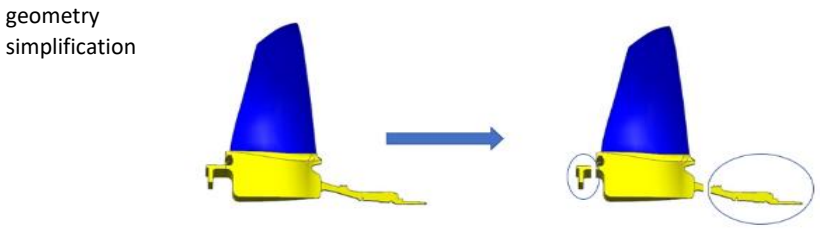

Figure 119. Geometry simplification procedure to reduce computational time: evaluating a single sector and eliminating the flanges. © 2020 Baker Hughes Company - All rights reserved

The blades of the axial compressor under analysis are made of austenitic inox steel, highly resistant to corrosion. Here, the main mechanical proprieties at ISO condition are listed: density 7897.4 $\mathrm{kg/m^3}$, tensile Yield strength 834.54 MPa, thermal expansion coefficient 1.54E-05C^{-1} Young strength193 GPa. The latter has then been replaced with its dynamic value, according to cyclic dynamic experiments, so to achieve a better accuracy in the frequency response computation.

Pre-processing in static analysis requires the application of external loads acting on the blade; both the fluid-dynamic loads of temperature and pressure and the centrifugal load have been evaluated. The latter was inserted by administering the velocity through the cylindrical coordinates on the Z axis counter- clockwise. The evaluation was repeated throughout the machine speed range. Analysing the first rotor stage the temperature and pressure resulted very close to standards values, therefore the main load is the centrifugal one, caused by rotation. The only area of the blade undergoing erosion is the airfoil; here the values show a variation. For this reason, the results of the analysis will be reported exclusively for the airfoil, which is the target of our comparison. Using an FEM analysis, it is necessary to create a mesh, the accuracy of the results analysis will be strongly linked to this procedure. To obtain high precision in the calculation of the stresses on the blade a very dense mesh is required. However, this leads to an increase in the analysis duration. So, it is essential to find a compromise between the accuracy of the solution

and the computational time. To build a mesh that meets both requirements it was necessary to decompose the blade into two bodies: Airfoil and Dovetail. The two bodies were then joined together in pre-processing, in order to create a single body through bonded contact. In an attempt to minimize the calculation time, it was decided to create a very dense mesh on the airfoil but less dense on the dovetail, see Figure 120.

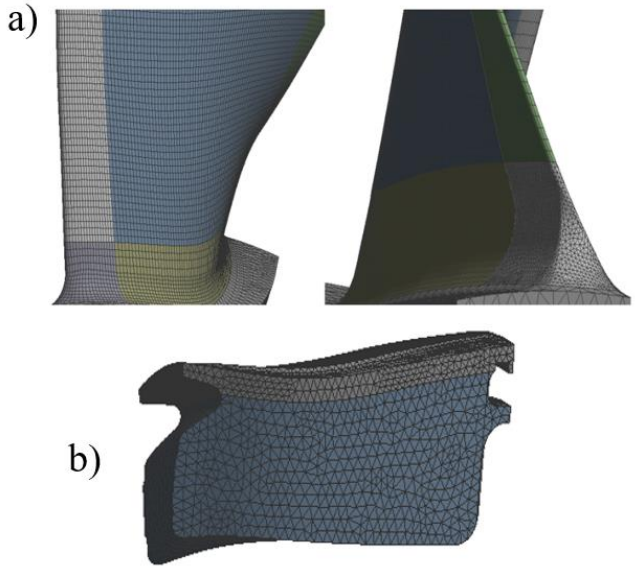

Figure 120 a) Airfoil mesh; b) Dovetail mesh. Hexahedral elements were used, except on the Leading Edge fillet radius and on the dovetail where the elements are tetrahedral. © 2020 Baker Hughes Company - All rights reserved.

This is due to the marginal role that the base plays in comparative analysis. Furthermore, the airfoil has been split into six bodies, to create preferential paths on which precise sizing has been applied, allowing one to select the number and size of the finite elements making up the mesh. The obtained mesh is shown in Figure 120a. This figure shows that two types of elements were chosen for the airfoil, hexahedral and tetrahedral, this is due to the curved geometry of the fillet radius of the leading edge, which is ill-suited to hexahedral elements and which would have led to quality parameters of the bad meshes.
The construction of the mesh of the two eroded models was carried out following the same indications followed in the baseline model. Due to the removal of material, however, the number of nodes and elements of the mesh varies, Table 27 shows the comparison between the three models.

Table 27. Number of nodes and elements of the complete mesh of the three profiles © 2020 Baker Hughes Company - All rights reserved.

	Nodes	Elements
Base-line Model	345620	143044
Model 1	247441	85668
Model 2	245263	86284

A.5. Results and discussion

The results of the static analysis were found in terms of Von-Mises equivalent stress and Table 27 reports a comparison on static stresses distribution between three models. In all three geometries, the Leading Edge fillet radius is the most stressed area considering static loads, and the maximum value is lower compared to the yield limit, therefore the deformations remain within the elastic field.

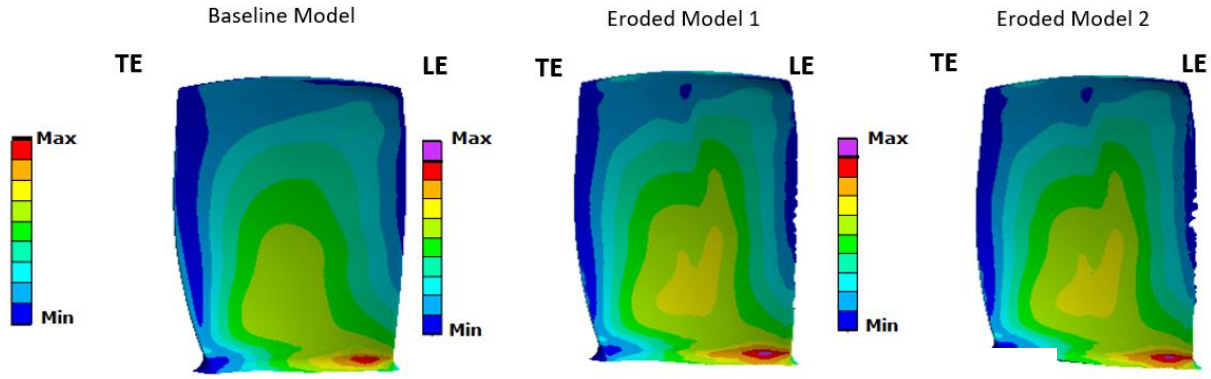

Figure 121. Static analysis comparison: equivalent Von-Mises stresses distribution from FEM ana results refer to the nominal rotation speed. The blade reported in figure has been flipped, the leading edge LE is t side whereas the trailing edge TE is on the left side. © 2020 Baker Hughes Company - All rights reserved.

Due to the material removal, the resistant section decreases, which generates ease in static stresses of the eroded models. Contrary to expectations, the eroded le dge remains unstressed. Although deformations remain within the elastic range, the str approaches the yield strength, so as the erosion rate increases the percentage variation between the maximum stress value and the yield strength is diminished. In the baseline model this percentage variation is 13%, in model 1 it decreases to 9% and in model it is 6%. The decrease in the resistant section slightly changes the stress map, as reported in Figure 121 and produces a redistribution of the latter: the knee in the centre of the tension map of the eroded geometries is due to a peak in stresses at the maximum erosion (40% of the radial span, see Figure 117). After having evaluated static stress, the modal analysis has been assessed. Coupling the modal module to the static one in Ansys workbench, the vibration analysis has been carried on considering a pre-stressed blade. The analysis of the baseline model natural frequencies has been performed according to the rotation speed within the machine operating range. These frequencies turned out to be almost constant with respect to the rotation speed, that's why in Figure 122 they are represented referring to the nominal speed V_n of the machine [69]. Evaluating the natural frequencies, the mode shape has been obtained, focusing on the first five modes highlighted in the Campbell diagram; as those are easily excited. Then the external exciting sources have been considered. The rotor wheels are vibrating because of the interaction of the fluid with the stator wheel. Plus, EO 1 to 4 have been evaluated, which can be induced by inlet distortion and stator

asymmetry. As a matter of fact, those are possible sources of excitation as confirmed by our previous on-field experience.

The natural frequencies of the new geometries don't differ significatively from the ones of original structure. The natural frequencies of the eroded geometries undergo a 1% maximum variation with respect to the baseline model. The blades at first stage are robust enough not to be affected by a variation of mass and stiffness caused by erosion. The variations in natural frequencies are negligible. Hence, the Campbell diagram has been considered as the baseline model for the eroded geometries too. There isn't any new crossing point arising in the Campbell diagram, Figure 122, and the 1 Flexural mode shape alone is excited by EO3 and EO4 in the operating range (highlighted in yellow).

In closing, the considerations on the fatigue comparison are reported. For this analysis Goodman's curves have been used, and these have been studied at the points of intersection highlighted in Campbell, where a component of the vibrating alternating stress arises. The experimental Goodman's curve, referred to 10^7 life cycles, was provided by fatigue tests in the laboratory on standard samples. The area subtended between the experimental curve and axes is the area of survival in HCF. The nearest point to the curve is the most stressed one, because it lies at the limit of survival. Both in the baseline model and in the two eroded models it was found that the radius of connection of the anterior border is the critical position about the HCF.

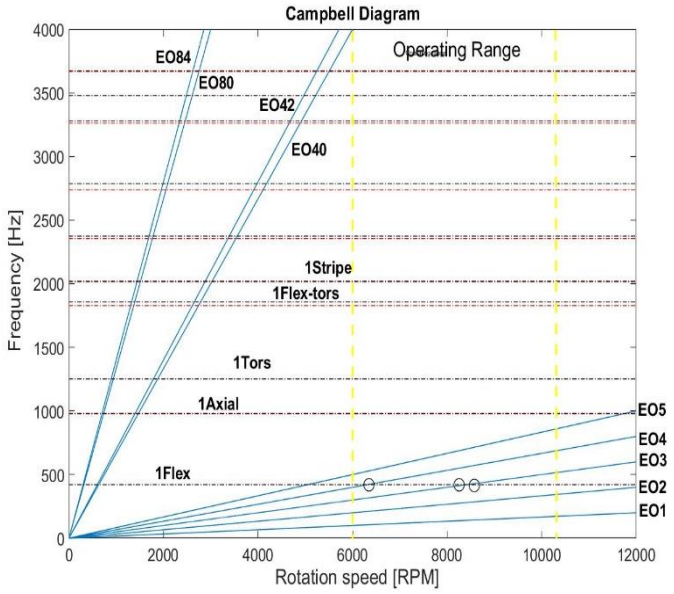

***Figure 122*. Campbell diagram shows the natural frequencies and the external exciting frequencies in terms of the speed of rotation of the machine, and the critical points at risk resonance are marked. © 2020 Baker Hughes Company - All rights reserved**

Furthermore, due to damage and cracks the fatigue strength decreases and the experimental Goodman curve moves downwards considering the decrease in the material capability. Since fatigue tests were not available for the material used, the curves of another material were used, and the two materials have similar mechanical characteristics and grain size. The proportions read between the baseline curve and the eroded curve of the reference material have been applied to the used material. This lowers the analysis accuracy but has been accepted to give the idea of a narrowing capability in HCF. Figure 123 shows Goodman's experimental diagram of the material used where the read proportions were applied, and the survival area decreased. The values of Figure 123 were normalized with respect to the static tension maximum value. Thus, there is a 60 % reduction in the survival area of the eroded component, caused by a decrease in fatigue resistance.

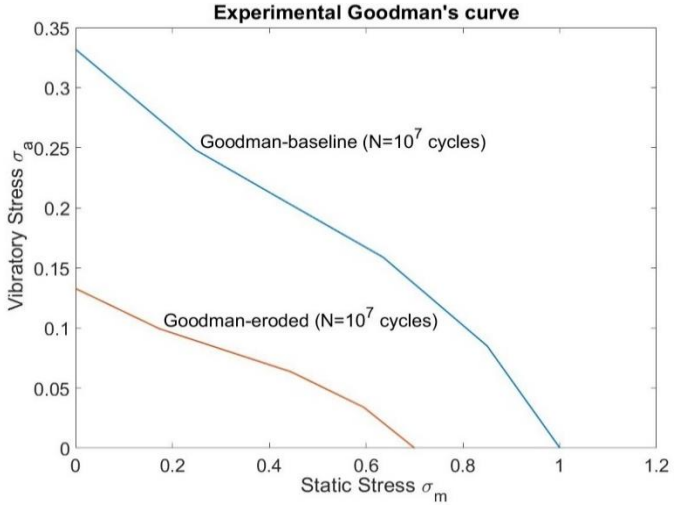

Figure 123. Experimental Goodman's curve of the used material. At the top the curve referred to the baseline model while at the bottom the scaled curve referred to the eroded models with less survival area. © 2020 Baker Hughes Company - All rights reserved

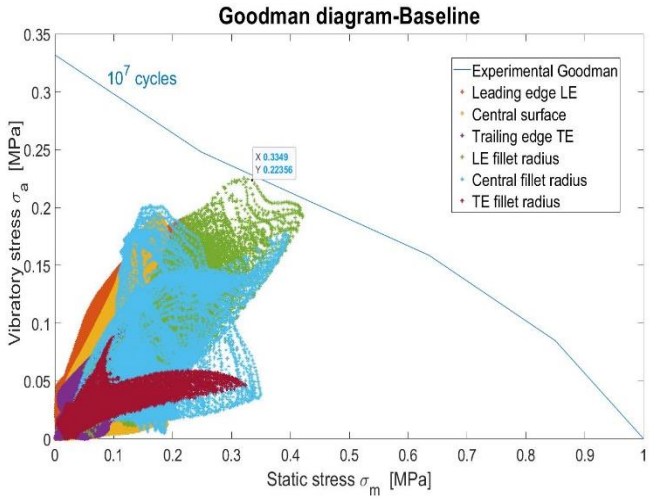

***Figure 124*. Goodman diagram of baseline geometries. © 2020 Baker Hughes Company - All rights reserved.**

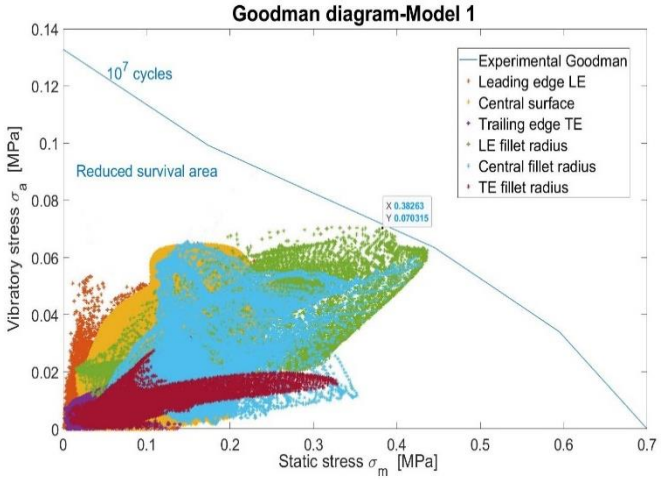

Figure 125. Goodman diagram of model 1. The leading edge continues to be the most fatigue stressed point, due to the removal of material and erosion, the survival area is reduced. © 2020 Baker Hughes Company - All rights reserved

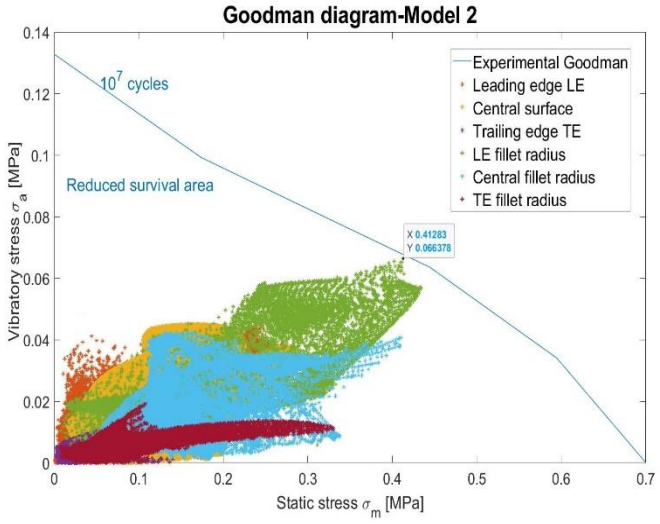

Figure 126. Goodman diagram of model 2. Due to increased static stress agents, it can withstand lower vibratory stresses. © 2020 Baker Hughes Company - All rights reserved

The Goodman are compared for the three geometries analysed, see Figure 124, Figure 125, Figure 126, by way of example the 1Flex mode shape and EO3 is shown. The stress values are shown in the graphs, the baseline model refers to 100% of the material capability, while the eroded geometries refer to the entire survival area corresponding to the area reduced by the damage. The closest point to the experimental curve is the most fatigue stressed one. Both in the baseline model and in the two eroded models it was found that the Fillet radius of leading edge is the critical position with regard to the HCF. The graphs show a squashing of the stress map on the abscissa axis, this is due to an increase in static stress which causes, at the same number of cycles (10^7), a decrease in vibratory stresses. Therefore, the decrease of the material capability means that, if the component design has been projected to endure certain stress values with difficulty, the design of the eroded component, being subjected to higher static stresses, supports lower vibratory stress.

A.5.1. Fracture Mechanics

Fatigue analysis can also be studied through Fracture Mechanics, thus analyzing the surroundings of the defect and its propagation.
It must be verified that the defects, caused by erosion, do not propagate if subjected to the static stress of the start and stop procedure. The machine as a whole is subject to 2500 cycles. The crack is hypothesized at the most stressed point: the leading edge fillet radius. The Opening Mode (MODE I tensile) and tensile stress normal to the plane of the crack are considered.
The propagation of the semi-elliptic crack on the baseline LE fillet radius was analyzed, through two analytical methods: British standard [70] and law of Paris [71] and the stress intensification factor K_I is used to study propagation. Once exceeded the threshold value (K_{th}), the crack

propagation progresses whereas if the factor exceeds a critical (K_c) value collapse occurs. In both analyses it is required to determine the size and shape of the initial crack, present at the beginning of the erosive phenomenon, during the incubation phase I (see Figure 116). The roughness arising at the beginning of the erosive phenomenon are points of amplification of the stress and potential trigger points of micro-cracks. The defects that were found at the beginning of the erosive phenomenon are semi-elliptical, characterized by depths in the range span of 100-200 μm and width 200-2,000 μm. Figure 127 shows the topography of defects in the early washing stages, obtained in the laboratory exploiting an atomic force microscopy (AFM). Hence, a semi-elliptic crack can be assumed [72].

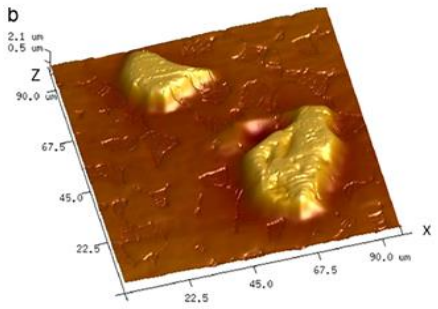

Figure 127. Topography of cracks at the beginning of the erosion phenomenon (AFM) © 2020 Baker Hughes Company - All rights reserved.

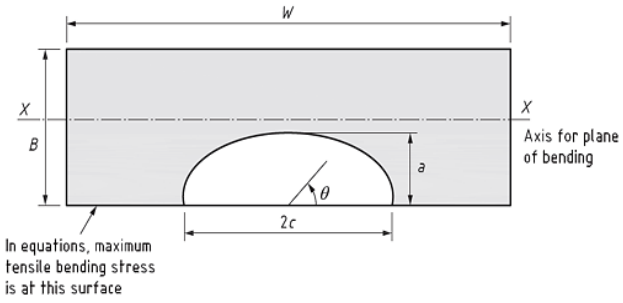

***Figure 128.* Geometric parameters of the semi-elliptic crack; © 2020 Baker Hughes Company - All rights reserved.**

The BS analytical method assumes the crack to lie on a rectangular plate, in Figure 128 the geometric parameters of the hypothesized semi-elliptical crack are shown. The geometric values of the crack initial depth (a) and width (2c) considered are respectively 200 μm and 2000 μm.

Below are the fundamental equations used in this analytical method BS [2], considering the ratio $a/2c < 500\ \mu m$:

$$\Delta K = (Y\Delta\sigma)\sqrt{a\pi} \qquad (1)$$

$$(Y\Delta\sigma) = Mf_w \left\{ \begin{matrix} k_{tm}M_{km}M_m\Delta\sigma_m + \\ \\ +k_{tb}M_{kb}M_b[\Delta\sigma_b + (k_m - 1)\Delta\sigma_m] \end{matrix} \right\} \qquad (2)$$

$$f_w = \left\{ \sec\left[\left(\frac{\pi c}{W}\right)\left(\frac{a}{B}\right) \right]^{0.5} \right\}^{0.5} \qquad (3)$$

$$M_m = \left[M_1 + M_2\left(\frac{a}{B}\right)^2 + M_3\left(\frac{a}{B}\right)^4\right]\frac{gf_\vartheta}{\Phi} \quad (4)$$

$$M_1 = 1.13 - 0.09\left(\frac{a}{c}\right) \quad (5)$$

$$M_2 = \left[\frac{0.89}{0.2 + (a/c)}\right] - 0.54 \quad (6)$$

$$M_3 = 0.5 - \frac{1}{0.65 + \frac{a}{c}} + 14\left(1 - \frac{a}{c}\right)^{24} \quad (7)$$

$$g = 1 + \left[0.1 + 0.35\left(\frac{a}{B}\right)^2\right](1 - \sin\vartheta) \quad (8)$$

$$f_\vartheta = \left[\left(\frac{a}{c}\right)^2 \cos^2\vartheta + \sin^2\vartheta\right]^{0.25} \quad (9)$$

$$\Phi = \left[1 + 1.464\left(\frac{a}{c}\right)^{1.65}\right]^{0.5} \quad (10)$$

$$M_b = M_m H \quad (11)$$

$$H = 1 + G_1\left(\frac{a}{B}\right) + G_2\left(\frac{a}{B}\right)^2 \quad (12)$$

$$G_1 = -1.22 - 0.12\left(\frac{a}{c}\right) \quad (13)$$

$$G_2 = 0.55 - 1.05\left(\frac{a}{c}\right)^{0.75} + 0.47\left(\frac{a}{c}\right)^{1.5} \quad (14)$$

$$(\Delta\sigma)_m = \frac{\sigma_{max} + \sigma_{min}}{2} \quad (15)$$

$$(\Delta\sigma)_b = \frac{\sigma_{max} - \sigma_{min}}{2} \quad (16)$$

The $k_{tm}, k_m, M_{km}, M_{kb}, M_m, M_b$ coefficients are multiplicative factors that indicate the intensification of stress around the crack, Y is geometric factor, σ the stress that would be present in the absence of defects whereas σ_{max}, σ_{min} represent respectively the static stress when turning the machine on and off, in absence of defects. Furthermore, σ_m and σ_b refer to the membrane and bending stress.

The multiplication coefficients and the geometric factor are function of the dimensions crack, depth (a), crack width (2c) and characteristic dimensions of the airfoil where the crack lies: thickness (B) and width (W). Starting from the initial geometry of the crack and according to the equations from (1) to (16), the collapse is reached at a depth of 6 mm, after 6,000 start and stop cycles.
The results obtained through the BS standards are compared with the values expected by applying the Paris law. In this case as well, the propagation analysis starts from an initial crack depth of 200 μm. Since the width of the airfoil W is known, the geometric factor Y exploiting Eqn 17 has been computed.

$$Y = 1.12 - \left(0.23 * \frac{a}{W}\right) + \left(10.6 * \frac{a}{W}^2\right) - \qquad (17) - \left(21.7 * \frac{a}{W}^3\right) + \left(30.4 * \frac{a}{W}^4\right)$$

Eqn 18 and 19 were used to calculate the stress intensification factor K_I and the crack propagation speed $\frac{da}{dN}$. Using an iterative process, the collapse depth of the crack obtained in correspondence of the critical factor K_c has been reached.

$$\Delta K = (Y\Delta\sigma)\sqrt{a\pi} \qquad (18)$$

$$\frac{da}{dN} = C(\Delta K)^m \qquad (19)$$

This procedure leads to a crack depth of 4.5 mm, which occurs after about 5,000 cycles. The number of cycles necessary to cause collapse, in both analytical methods, is greater than the 2500 start and stop cycles. Therefore, collapse does not take place and does not lead to any concern. The propagation analysis was carried out again also on the eroded geometries, this time hypothesizing of cracks not only at the root, but along the whole radial span of the leading edge, see Figure 129.

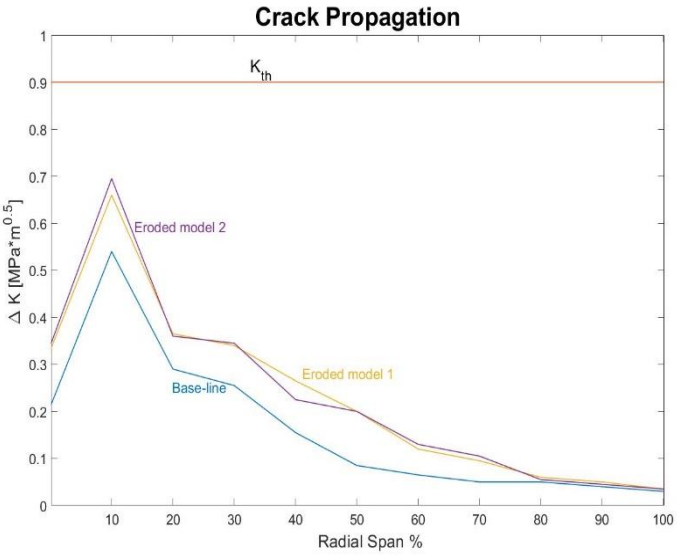

Figure 129. **Stress intensification factor profile as a function of radial span, length of the leading edge, referred to normalized values, in the three models evaluated.**
© 2020 Baker Hughes Company - All rights reserved

The graph shows the maximum peak at 10% of the radial span, at the fillet radius of the leading edge, where the major static stresses act. As one proceeds towards the TIP of the airfoil the stresses decrease, therefore the factor of intensification of the stresses K decreases. For all three models the K factor is lower than the threshold value by not showing propagation over the entire radial span.

A.6. Conclusion and future developments

The removal of matter slightly modifies the stress field and leads to an increase in static stress values, although worsening the criticality of the leading edge fillet radius, the stress values remain lower than the yield limit, with deformations in the elastic field. The latter does not introduce new crossings of resonant frequencies and does not change the shape modes of the blade. Therefore, the created damage does not raise concerns in terms of mechanical properties, both static and dynamic criteria remain satisfied. The phenomenon of damage is not compromising the operation within the period of the maintenance and the limits imposed to erosion do not derive from structural considerations but rather from fluid-dynamic variations (reduction of the aerodynamic cord and fluid-dynamic efficiency). The structural analysis confirms the design of the blade, which although damaged, allows for and strengthens the use and investigation of on-line water washing. This work stands as an intermediate step, leaving some open points to further investigate. It will be necessary to evaluate: perform fatigue tests on eroded specimens of the material considered, in order to obtain the Goodman curve referred to the eroded material.

Furthermore, it is advised to optimize the creation of the eroded geometry exploiting field data and producing more CFD simulations, following the step-by-step procedure. In closing, it will be interesting to evaluate a forced response analysis to verify a matching with the results presented in this work.

Appendix B.

Preliminary study of Erosion prediction of GT AXCO Blades Subjected to Water Injection (Springer's Model)

Reproduced in part from*:* A. Chiariotti, et al.,2018, *"Erosion Prediction of Gas Turbine Compressor Blades Subjected to Water Washing Process."* Asia Turbomachinery and Pump Symposia. 2018 Proceedings. Turbomachinery Laboratory, Texas Engineering Experiment Station.

Here, the adoption of the model developed by Springer et al., (1974) [21] has been considered as a possible approach for studying the effect of WDE on compressor blade during the water-washing process. The model was implemented in the well validated P-Track code developed by some of the authors at Sapienza University of Rome (i.e., Borello *et al*., 2012 [32], 2013 [73]; Venturini *et al.*, 2012 [74]; Rispoli *et al.*, 2015 [75]; Cardillo *et al.*, 2014 [76], Castorrini *et al.*, 2016 [77]). P-Track was properly developed for analyzing: a) two-phase flows using Lagrangian approach, b) impact of particles/droplets over solid surfaces. Here, the code capabilities are demonstrated in a turbomachinery application. In the following paragraphs, the adopted erosion model is described. Then, the carrier flow field is briefly sketched together with the results of the erosion model. Results of numerical simulations are then presented and discussed. Some concluding remarks close this study.

B.1. Water droplet erosion model

A Lagrangian droplet tracking model should firstly track the droplets trajectories from the injection nozzle to the impact on the solid wall, and then estimate the erosion due to the impact of the droplets. Both the aspects are accounted for in P-Track adopting a one-way coupling approach, meaning that droplets motion is affected by the flow but not vice-versa (Sommerfeld *et al.*, 2009 [33]).

Despite some WDE models have been proposed even in recent years (see for instance, Lee *et al.*, 2003 [26], Liu *et al.*, 2015 [40]), one of the most general and used is the model proposed by Springer *et al.*, (1974 [21]). The erosion rate (that is, the amount of eroded mass per impacting

droplets) is expressed as a function of the main characteristics of droplets and target material, together with the impact velocity and angle. The model also takes into account the incubation period: the erosion process occurs only after a threshold number of impacts n_i below which no erosion damage takes place. After n_i the erosion process linearly increases with the number of impacts. As a second threshold number of impacts n_f is reached, the erosion process tends to be independent from the successive droplet impacts (Figure 130).

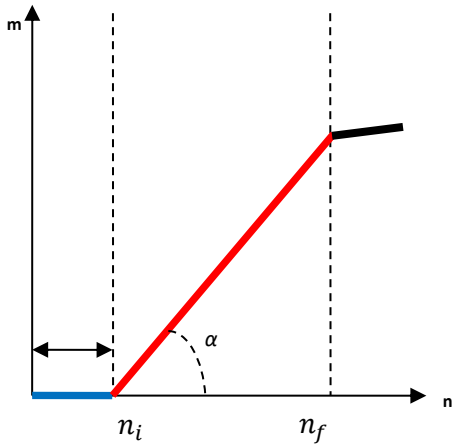

Figure 130. Eroded material as a function of the number of impacted droplets

The model writes as

$$\begin{cases} m = 0, & if \;\; n < n_i \\ m = \alpha\left(n - n_i\right), & if \;\; n < n_i \\ m = const, & if \;\; n > n_f \end{cases} \qquad (1)$$

being m the eroded mass per number of impacts, and n the number of impacts. The total eroded metal is then given by $\int_{n_i}^{n} m dn$. The value of n_i is a function of the pressure caused by the impact of a droplet on the target material, and the properties of that material. Such value is called water-hammer pressure P:

$$P = \frac{z_R v_{imp} \sin\beta}{1 + z_R / z_C} \qquad (2)$$

In eq. (2), v_{imp} is the impact velocity, β is the impact angle, z is the impedance and subscripts C and R refers to coating and substrate materials, respectively (Springer assumes that the blade is formed of a coating layer and a substrate).
The slope α in eq. (1) is related to n_i by an empirical correlation

$$\alpha = \alpha^* \pi \rho_w \, d^3 / 6 \qquad (3)$$

where

$$\alpha^* = 0.023 \left(\frac{1}{n_i^*} \right)^{0.7}$$

$$n_i^* = 7.0 \cdot 10^{-6} \frac{S_{eff}}{\bar{\sigma}_0} = n_i \frac{\pi d^2}{4}$$

ρ_w is the droplet density (here assumed to be water), S_{eff} is a quantity accounting for the properties of the target material, $\bar{\sigma}_0$ is the mean stress at the impact point, and *d* is the droplet diameter. For further details see Springer et al., (1974) [21].

B.2. Prediction of erosion

The first step to quantify erosion on GT compressor blades caused by water injection was the CFD prediction of carrier air flow through the compressor from the bell-mouth to the compressor first stage. The droplets trajectories were computed from the spray injection location and then analyzing their spreading and their impact against the first compressor rotor. It must be stressed that the droplets are released from nozzles located in the bell-mouth, then they cross the inlet section and the inlet guide vanes (22 blades) before reaching the compressor first rotor (16 blades). A number of complex circumstances must be addressed in the numerical model. Two of them have been mentioned: a) the ratio between the blades number in the IGV and the compressor first stage is incommensurable, then all the stator and rotor blades (plus inlet section) should be meshed (or at least half of them considering 11 and 8 blades respectively); b) the compressor first stage is rotating and then a proper stator/rotor meshing should be considered. To face these problems, a mixing plane approach has been used. A time-average flow solution can be obtained by solving for a time-independent solution and averaging the fluxes in circumferential direction on the interface surface.

B.2.1. Model set up

The adoption of the mixing plane approach allowed to simplify, the creation of the compressor geometry. The computational domain was divided in four parts from the engine inlet to the first compressor rotor. Regions have been sorted as follows: GT inlet, inlet extension, IGV, compressor first stage of an LM2500+(Blisk), see Figure 131. In the figure, the location of the injection nozzle

is also indicated. Struts geometry has been ignored as its contribution can be considered negligible to the scope of the analysis.

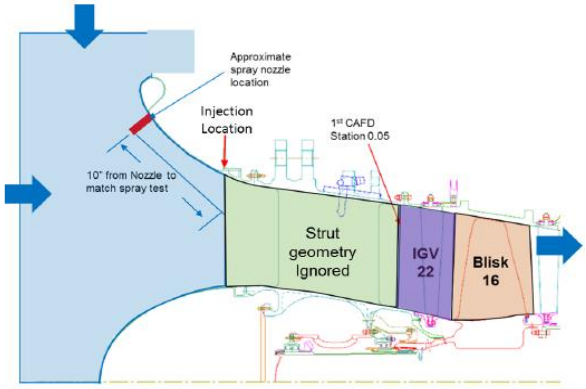

Figure 131. Model Geometry

The domain was discretized by using an unstructured grid (Figure 132): tetrahedral cells were used in all the domain except close to the solid walls are prismatic cells were used to improve the prediction of the boundary layer. Wall function was used to model the near-wall boundary layer. The prisms layer was properly adjusted to have a non-dimensional distance of the first cells row 30<y+< 200. Other grid refinements were introduced to ensure the proper resolution of the vane and blade leading and trailing edge curvature, as well as refinements for fillets at the inner or outer Diameter. The total nodes and cells numbers were equal to 10.4M and 3.7M respectively. The flow field was solved by using ANSYS CFXv16.2. The turbulent flow governing equations, (continuity, momentum and energy conservation) were solved using Reynolds Averaged Navier Stokes (RANS) closure. Here, the well-established SST Turbulence model (Menter, 2009) was adopted.

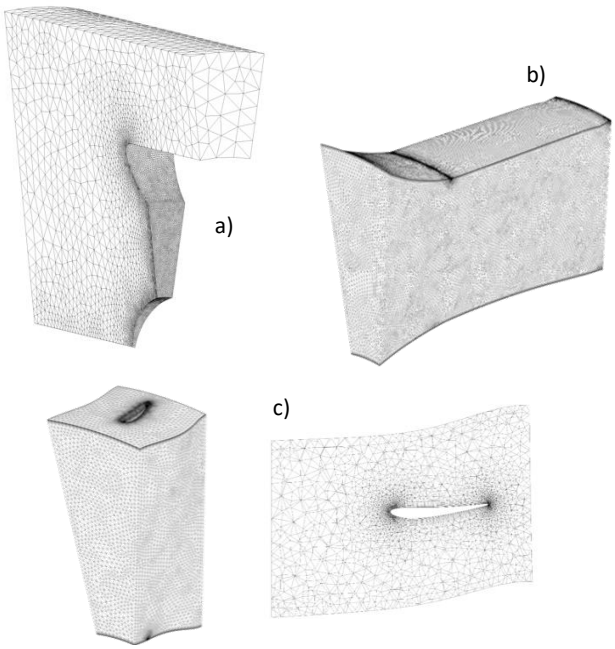

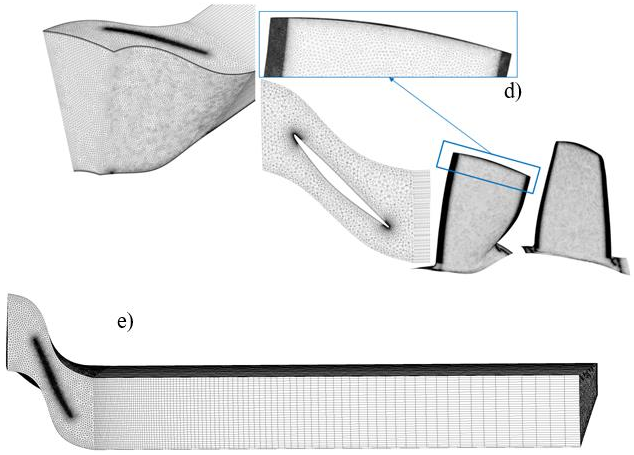

Figure 132. Mesh details: a) Inlet section; b) Bell-mouth and straight duct; c) IGV; d) Compressor first stage; e) Outlet section

B.2.2. Boundary conditions

Total temperature and pressure were fixed at inlet, automatic wall functions were adopted on the solid walls, and outflow boundary conditions where set at the end of the rotor. To avoid unphysical pressure condition at the outlet, a straight outlet section, 5 hydraulic diameters long, was inserted downstream from the compressor first stage outlet (Figure 132.e). As told before, mixing plane was inserted to model the interaction between the IGV and the compressor first stage regions. It is important to recall that the domain extension in tangential direction is different between stator and rotor. In fact, the stationary portion has an angular extension of about 16°, while the rotating part has an angular extension of 22.5°. The turbulent flow governing equations, (continuity, momentum and energy conservation) were solved using Reynolds Averaged Navier Stokes (RANS) closure. Here, the well-established SST Turbulence model (Menter, 2009) [31] was adopted. As the volume of water with respect to air is very small, when modeling the droplet tracking, a one-way coupled approach was assumed.

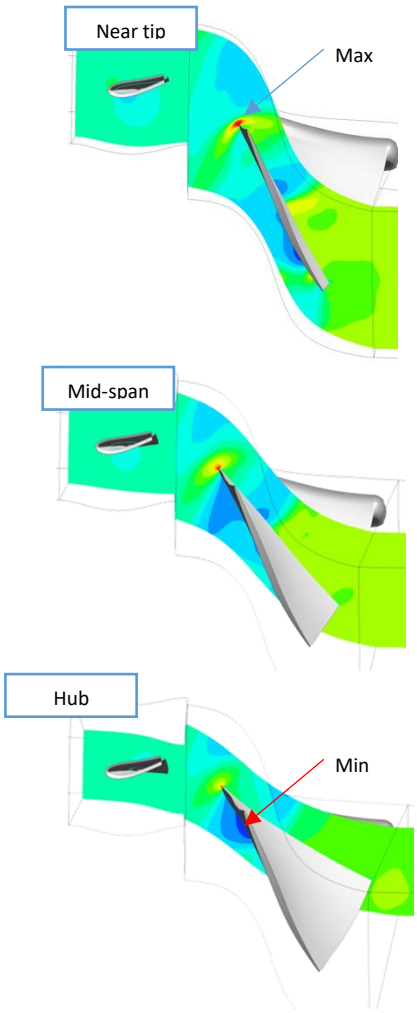

Figure 133. Pressure field at three different span positions

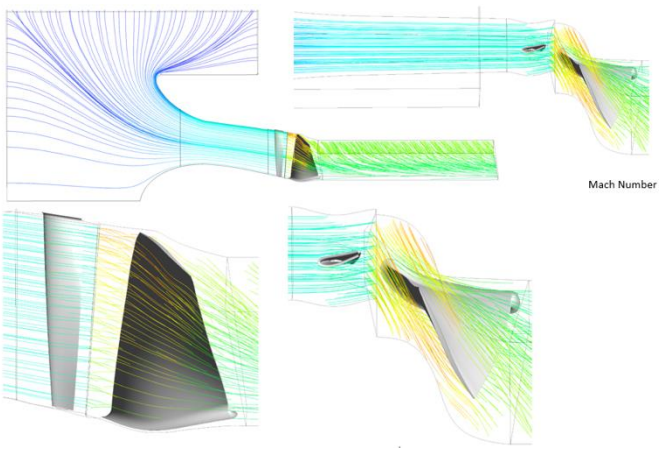

Figure 134. Multi-Stage Model: Flow Field Visualization

B.2.3. Multi-Stage Model Flow Field Result

Results of simulation are shown in Figure 133 Figure 134 Figure 135 Figure 136. At the inlet, stagnant fluid is assumed. When flowing inside the bell-mouth and the IGV region, the maximum Mach number (Ma) increases from about 0 at ambient to about 0.4 at the mixing plane. In the rotating domain, the Ma strongly increases up to a max of about 1.3 that was predicted near the tip of the suction side of the compressor first stage (Figure 134).

In Figure 133, the pressure field at three different span positions, near the tip, near the hub and at mid span, is shown. The coupling between the IGV and compressor first stage required the application of mixing plane. Focusing on the compressor first stage, in all the planes, the maximum pressure value is measured at the leading edge where static pressure is close to the stagnation one. Maximum value is reached close to the tip where the tangential velocity is maximum. The minimum pressure value is predicted close to the hub where a strong flow acceleration is present.

In Figure 135, the pressure distribution on the compressor first stage blade is shown. As discussed before, the maximum pressure is predicted along the leading edge. On the pressure side, the streamlines are almost parallel. This suggests that secondary motion is almost negligible, except close to the tip, where the streamlines deviation indicates the development of tip-leakage flow. On the suction side, the fluid velocity is generally higher. The flow is subjected to stronger deviation, thus leading to a large flow separation developing close to the hub when moving towards the trailing edge (Borello et al., 2009 [78]). It is arguable that on the suction side the flow acceleration and deviation leads to very low number of impacting droplets on the suction side, while the maximum erosion rate should be obtained on the pressure side.

In Figure 136, the turbulent kinetic energy (k) plot is shown. On the suction side, k distribution indicates several phenomena. First, the region of high k close to the leading edge accounts for the rapid acceleration of the flow downstream from the leading edge. Furthermore, close to the tip and mid-chord, the high k value indicates the presence of the tip leakage vortex generated by the pressure difference across the tip gap (Borello et al., 2007 [79]). Finally, starting from a region placed around mid-chord and close to the hub, the low turbulence region extending up to the trailing edge and to about mid-span indicated the presence of the large corner separation vortex (Borello et al., 2010 [42]). On the pressure side, the k values are generally lower, due to the lower strain associated to a generally slower flow. The only peak is located in the position where the fluid starts to cross the tip gap driven by the pressure difference between pressure and suction surface (tip leakage flow).

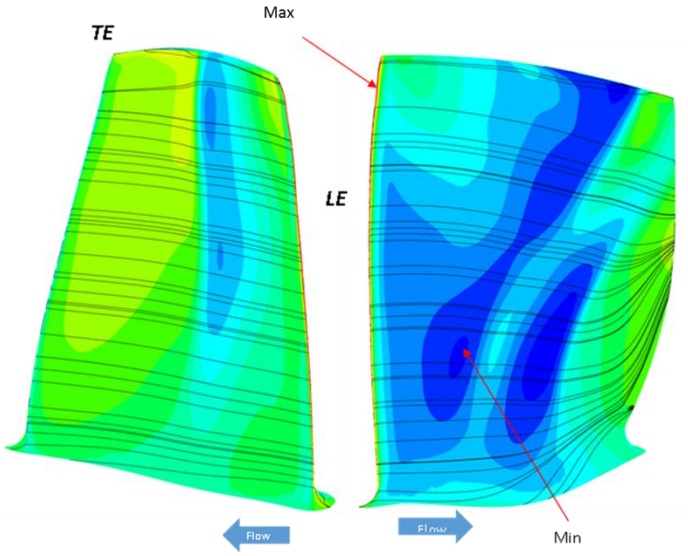

Figure 135. Pressure field in the pressure and the suction side

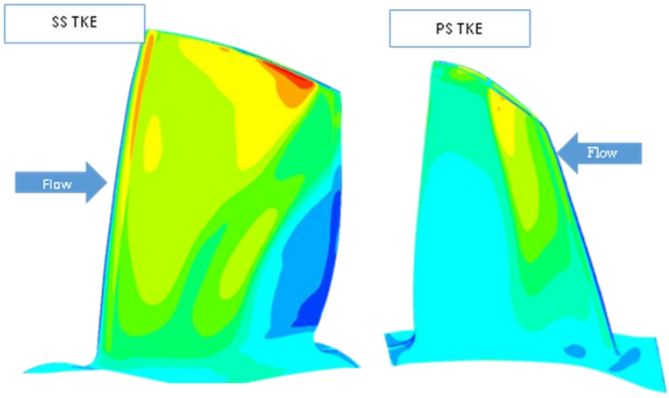

Figure 136. Multi-Stage Model: turbulence kinetic energy

B.3. Erosion

To reduce the computational time, a preliminary simulation was performed to individuate the region of the blisk inlet surface where droplets are concentrated. To this end, several droplets were injected from the nozzles mounted on the bell mouth (see Figure 131) and tracked until they reached the blisk inlet surface (Figure 137, red lines). This information to simulate WDE on the compressor blade has been used: a large number of water droplets were then released from that region with the same flow velocity. This means that only the central portion of the blade is invested by droplets, as in the actual case. Moreover, in real application droplets size distribution ranges between about 10 and 300µm, with a maximum injected mass between 90 and 110 µm. Two droplets size classes have been simulated, namely 25 and 100µm: the latter represents the most relevant size class; the former is chosen in order to study the effect of droplet inertia on erosion patterns. Indeed, despite the Stokes numbers are larger than unity (Stk=4 for 25 µm droplets, Stk=66 for 100µm ones), and then inertia is the dominating effect, they differ of about

one order of magnitude, thus erosion patterns are expected to show some differences. In Table 28 main characteristics of the simulated droplets are summed up.

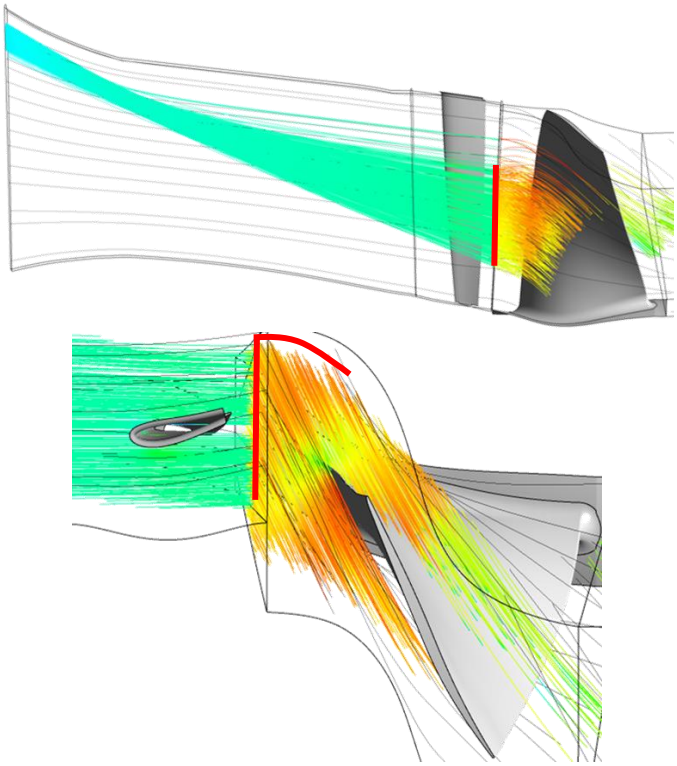

Figure 137. Preliminary simulation: trajectories of the released droplets and droplet inlet region (red lines) in blisk domain for WDE simulation

Table 28. Main characteristics of the simulated droplets

Size	Inlet vel.	Material	Stk	Simulated
25µm	Flow	Water	4	>100000
100µm	Flow	Water	66	>100000

Figure 138 and Figure 139 show the impact positions (colored with impact angle) of both the droplet size classes on pressure and suction sides of the blade. According to what has been found in the preliminary simulation, droplets mostly impact the blade on the suction side (see also Figure 137). Only a limited number of impacts are found on the suction side, and all of them are within a narrow region close to the leading edge (Figure 139). Since the Stk number is larger than one for both size classes, droplets have a ballistic behavior, hence their impact angles (Figure 138 and Figure 139) follow the blade swirl. The only difference is at the leading edge, where droplets impact the blade with an angle ranging from 50° to 90°, and this will affect the erosion patterns, as shown further on.

Figure 140 represents the droplets impact points on pressure side colored with impact velocity. As shown in figure (bottom), the 100 µm droplets impact velocities are divided into clear regions, with the higher velocities located after the mid span.

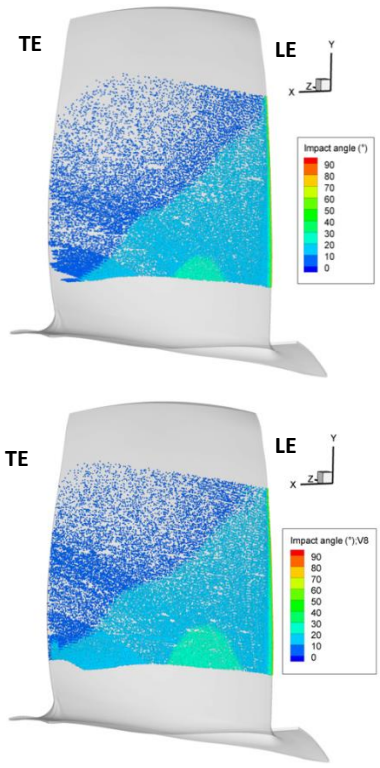

Figure 138. 25 (top) and 100 (bottom) µm droplets impact points on pressure side colored with impact angle (LE: leading edge; TE: Trailing edge)

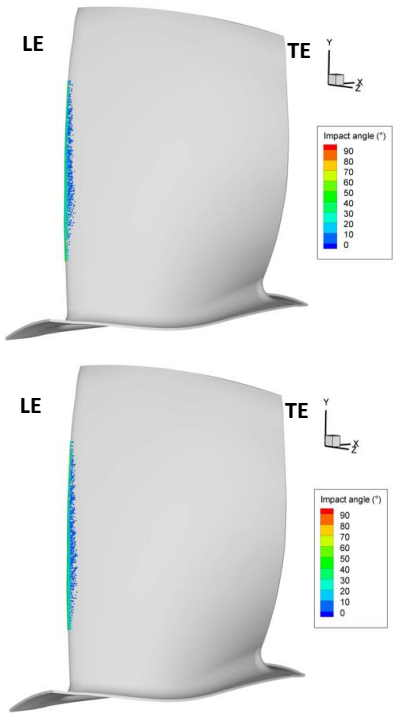

Figure 139. 25 (top) and 100 (bottom) µm droplets impact points on suction side colored with impact angle (LE: leading edge; TE: Trailing edge)

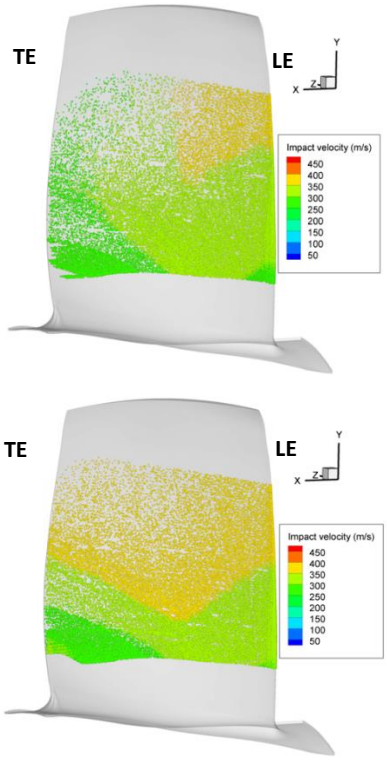

Figure 140. 25 (top) and 100 (bottom) µm droplets impact points on pressure side colored with impact velocity (LE: leading edge; TE: Trailing edge)

A slightly different behavior is found for smaller droplets. Even in this case indeed, the impact velocities are larger after the mid span, but there are divided into less defined regions (Figure 140, top) and having a different spread on the blade. This effect is again due to the different inertia: smaller particles are more reactive to flow variations, and this affects the impact velocity. Since erosion rate depends on the number of simulated droplets, to have results independent from this quantity the normalized erosion rate per unit surface has been computed. It has been used two different normalizations: in the first the actual erosion rate is normalized with the simulation maximum value (ER-l), and with the maximum of both simulations (ER-n) in the second one. While ER-l can be used to compare the erosion patterns due to different droplets size classes, ER-n allows to compare their erosive capacity, therefore individuating the most dangerous size range. These two simple quantities are very useful: they can be used in the design process in order to optimize the blade profile, and in the management of water washing operations avoiding the usage droplets in the most erosive size and helping to plan a proper maintenance.

Figure 141 shows ER-l for both size classes; only pressure side is reported because on the suction side, as already seen, there is no erosion except for the narrow stripe close to the leading edge. As shown, the erosion patterns are very similar. Three main erosion regions can be identified in both cases: one at the leading edge, showing the largest erosion (A) and involving a narrow stripe also on the suction side (A'); another (B) after the leading edge region, toward the trailing edge,

in which the erosion rate is smaller than in A; the last region (C) is at the bottom of the blade close to the trailing edge, where a recirculation is present. The rest of the blade invested by droplets shows a very small erosion rate (blue region in Figure 141). Regions named A and A' are similar for both the droplet classes, being narrower toward the tip of the blade (especially in the pressure side) and becoming wider toward the hub. Regions B and C are a bit wider in the case of 25 µm droplets, but thinner, compared to 100 µm one. These differences can be ascribed to the different inertia of the two simulated classes of droplets: smaller ones react faster to flow deviations, and this causes a wider dispersion. Despite these slight differences, the erosion patterns are similar: as all the particles have a Stokes number greater than 1, their strong inertia makes their trajectories not much influenced by the flow field. As a consequence, the droplets impacts are concentrated on the lower side of the blade following more or less a straight trajectory. Erosion mechanism is then consequently concentrated in the lower blade region, even if the larger impact velocities are reordered at the upper part of the blade.

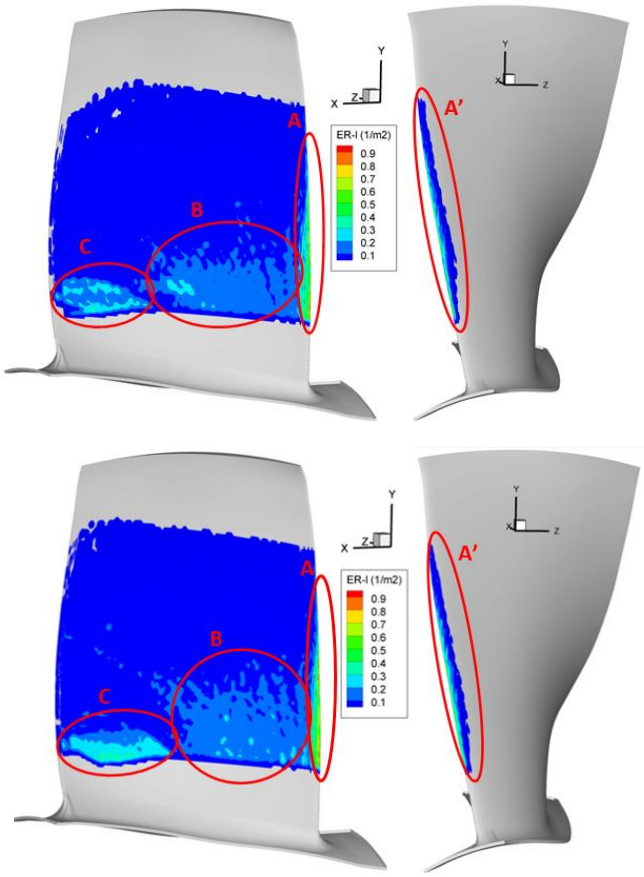

Figure 141. 25 (top) and 100 (bottom) µm droplets normalized erosion rate (ER-l) per unit surface on pressure side (left) and suction side (right). Red ellipses put in evidence the three main eroded regions

Figure 142 show the normalized erosion rate ER-n on pressure and suction side for both droplets size classes. By comparing the two simulations (Figure 142 top and bottom) it is evident that larger droplets are extremely more erosive than the smaller ones, as expected. This is due to the impact energy which is proportional to the droplet mass, that is, the larger the droplet mass the larger is its erosive potential. However, erosion also depends on other quantities (i.e., impact angle and velocity), hence the erosion rate is a combination of all these quantities.

The region most exposed to erosion is the leading edge, and this is in good (qualitative) agreement with measurements made on other compressor blades exposed to WDE (Figure 143).

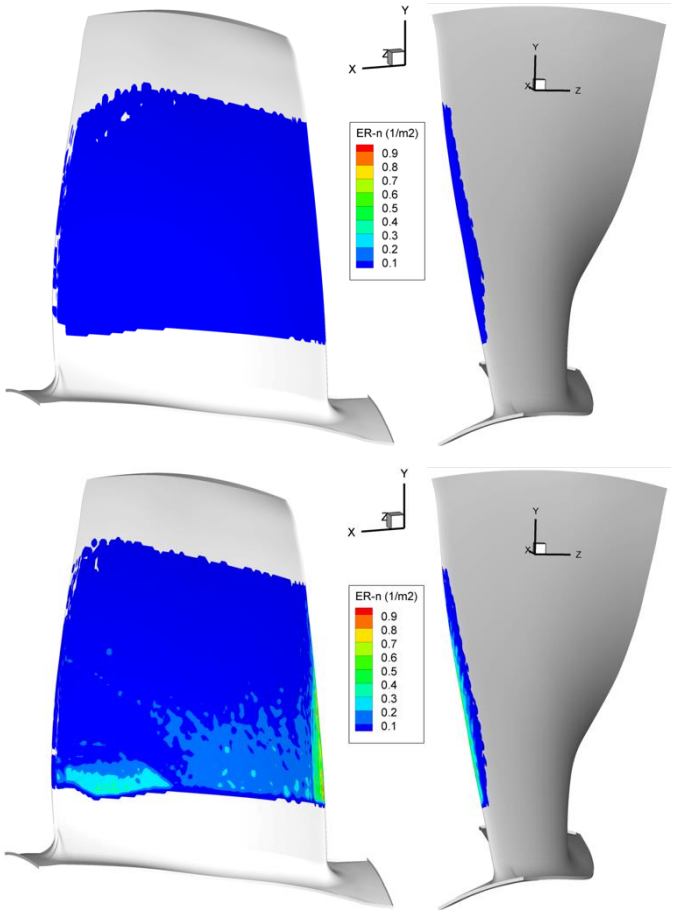

Figure 142 25 (top) and 100 (bottom) µm droplets normalized erosion rate (ER-n) per unit surface on pressure side (left) and suction side (right)

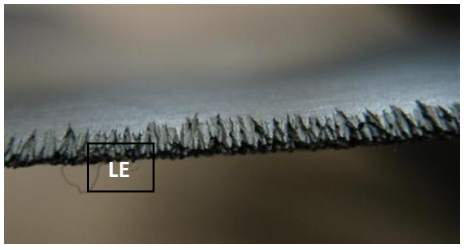

Figure 143. Compressor blade exposed to WDE process

In real situations, another aspect should be accounted for, namely the mass of different size droplets actually impacting the blade. In the present simulation, indeed, it has been simulated the same number of droplets for both classes. This was necessary to study the erosion process, the erosive behavior of different droplets, and the most critical regions of the blade. However, if one wants to realistically predict the eroded mass after a given time of exposition to WDE, the computed erosion rate should be scaled according to the actual mass of impinging droplets.

B.4. Conclusions

Erosion is a very complex problem in compressor blades especially when on-line water-washing techniques are adopted. Here a first step study of a GT compressor was carried out focusing on the droplets erosion over compressor first stage pressure surface.
In the present simulation, the erosion due to two different droplets size classes was analyzed. Introducing two different normalized erosion rates, the first normalizing by the simulation maximum erosion (ER-l) and the second normalizing by the maximum of both simulations (ER-n), are used to help the analysis. ER-l is used to study any difference in the erosion patterns of the two size classes. It was found that, even with some slight differences, the erosion patterns are very similar because of the high Stokes number of both the droplet sizes. On the other side, ER-n is used to compare the erosive capacity of different droplets. The simulations showed that, assuming the same number of simulated droplets for both size classes, the erosion is mainly due to the larger one because of their larger impact energy. However, in order to make a prediction, the actual number of droplets for each size classes should be simulated.
Even if this is only a first step of a long term study, it is already clear that it could be very useful since results can provide data that can be used in the design process, in order to optimize the blade profile, and in the management of water washing operations.

Bibliography

Bibliography

[1] R. Kurz and K. Brun, "Fouling Mechanisms in Axial Compressors," *J. Eng. Gas Turbines Power,* vol. 134, no. 3, p. 032401 (9 pages), 2012.

[2] C. Meher-Homji, M. Chaker and H. Motiwala, "Gas Turbine Performance Deterioration," in *30th Turbomachinery Symposium*, Houston, 2001.

[3] G. Aker and H. Saravanamuttoo, "Predicting gas turbine performance degradation due to compressor fouling using computer simulation technique," *Journal of Engineering for Gas Turbines and Power,* vol. 111, pp. 343-350., 1989.

[4] Tae Won SONG et all., "An Improved Analytic Model to Predict Fouling Phenomena in The Axial Compressor of Gas Turbine Engines," in *International Gas Turbine Congress (IGTC)*, Tokyo, 2003.

[5] K. Jordal, M. Assadi and M. Genrup, "Variations in gasturbine blade life and cost due to compressor fouling - A thermoeconomic approach," *Int. J. Applied Thermodynamics,* vol. 5, pp. 37-47., 2002.

[6] I. Dominizi, S. Gabriele, A. Serra and D. Borello, "Comparative Life Cycle Assessment of different Gas Turbine Axial Compressor Water Washing Systems," in *ASME Turbo Expo 2020*, Virtual Conference. Paper no. GT2020-15206, 2020.

[7] J. P. Stalder and J. Sire, "Salt Percolation Through Gas Turbine Air Filtration System and Its Contribution to Total Contaminant Level," in *International Joint Power Generation Conference*, New Orleans, Louisiana. Paper No. JPGC2001/PWR-19148, 2001.

[8] C. B. Meher-Homji and A. Bromley, "Gas Turbine Axial Compressor Fouling And Washing," in *33th Turbomachinery Symposium*, Houston, Texas, 2004.

[9] H. Margolis, "US Navy on-line compressor washing of marine gas turbine engines," in *International Gas Turbine and Aeroengine Congress and Exposition*, 1991.

[10] P. McDermott, " Apparatus for cleaning gas turbine engine". Patent US Patent No. 5 273 395, 1993.

[11] J.-P. Stalder, "Gas turbine compressor washing state of the art," in *ASME International Gas Turbine & Aeroengine Congress & Exhibition,*, Paper No.98-GT-420, 1998.

[12] Gas Turbine High Flow On-Line Water Washing Technical Description, Baker Hughes Procedures.

[13] E. Whaba and H. Nawar, "Multiphase flow modeling and optimization for online wash systems of gas turbines," *Elsevier,* pp. 7549-7560, 2013.

[14] J.-. P. Stalder and P. Van Oosten, "Compressor washing maintains plant performance and reduces cost of energy production," in *ASME International Gas Turbine & Aeroengine Congress & Exposition*, Hague, Netherlands, Paper No. 94-GT-436, 1994.

[15] S. Madsen and L. Baxxen, "Gas turbine fouling offshore; effective online water wash through high water-to-air ratio," in *ASME Turbo Expo* , Oslo, Norway paper no. GT2018-75618. , 2018.

[16] J. Oosting, K. Boonstra, A. De Haan, D. Van Der Vecht, J. Stalder and U. Eicher, "On line compressor washing on large frame 9-FA gas turbines erosion on RO compressor blade leading edge field performance with a novel on line wash system," in *ASME Turbo Expo*, Montreal, Canada , 2007.

[17] F. Heymann, "Erosion by liquids. Machine Design," *Flow, Turbulence and Combustion,* vol. 10, pp. 118-124, 1970.

[18] Y. Oka, S. Mihara and H. Miyata, " Effective parameters for erosion caused by water droplet impingement and applications to surface treatment technology," *Wear,* vol. 263, no. 1-6, pp. 386-394, 2007.

[19] A. Gujba, L. Hackel and M. Kevorkov, "Water droplet erosion behaviour of Ti-6Al-4V and mechanisms of material damageat the early and advanced stages," *Wear,* Vols. 358-359, pp. 109-122, 2016.

[20] R. Li, H. Ninokata and M. Mori, "A numerical study of impact force caused by liquid droplet impingement onto a rigid wall," *Progress in Nuclear Energy,* vol. 53, no. 7, pp. 881-885, 2011.

[21] G. Springer, C. Yang and L. P.S, " Analysis of rain erosion of coated materials," *Journal of Composite Materials,* vol. 8, no. 3, pp. 229-252, 1974.

[22] W. Tabakoff, R. Kotwal and A. Hamed, "Erosion study of different materials affected by coal ash particles," *Wear,* vol. 52, pp. 161-173, 1979.

[23] H. Kirols, "Water Droplet Erosion: Influencing Parameters, Representation, and Comparisons," in *Master's Thesis, Concordia University*, Montreal, Canada, 2015.

[24] A. S. G73, "Standard test method for liquid impingement erosion using rotating apparatus," *ASTM International, West Conshohocken, PA, ,* Vols. DOI 10.1520/G0073-10, www.astm.org., 2010.

[25] L. Seleznev, V. A. Ryzhenkov and A. F. Mednikov, "Phenomenology of Erosion Wear of Constructional Steels and Alloys by Liquid Partcles," *Thermal Engineering,* vol. 57, no. 9, pp. 741-745, 2010.

[26] B.-E. Lee, K.-J. Riu, S.-H. Shin and S.-B. Kwon, "Development of a water droplet erosion model for large steam turbine blades," *KSME International Journal,* vol. 17, no. 1, pp. 114-121, 2003.

[27] V. A. Ryzhenkov, L. Seleznev and A. V. Ryzhenkov, "Investigation of Erosive Wear of Constructural Materials," *Thermal Engineering ,* vol. 61, no. 10, pp. 736-740 , 2014.

[28] Q. Zhou, N. Li, X. Chen, T. Xu, S. Hui and D. Zhang, "Analysis of water drop erosion on turbine blades based on a nonlinear liquid-solid impact model," *International Journal of Impact Engineering,* vol. 36 , pp. 1156-1171 , 2009.

[29] M. Ahmad, M. Casey and N. Sürken, "Experimental assessment of droplet impact erosion resistance of steam turbine blade materials," *Wear,* vol. 267, pp. 1605-1618, 2009.

[30] A. Chariotti, D. Borello, P. Venturini, S. Costagliola and S. Gabriele, "Erosion model for gas turbine compressor blades subjected to water washing systems," in *ATPS 2018, March 12-15 2018, Suntec, Singapore*, Singapore.

[31] F. Menter, "Review of the shear-stress transport turbulence model experience from an industrial perspective," *International Journal of Computational Fluid Dynamics,* vol. 23, no. 4, pp. 305-316, 2009.

[32] D. Borello, F. Rispoli and P. Venturini, "An integrated particle-tracking impact/adhesion model for the prediction of fouling in a subsonic compressor," *Journal of Engineering for Gas Turbines and Power,* vol. 134, no. 9, p. 092002 (7 pages), 2012.

[33] M. Sommerfeld, B. Van Wachem and R. Oliemans, "Best practice guidelines," in *ERCOFTAC Special Interest Group on Dispersed Turbulent Multi-Phase Flow*, 2008.

[34] M. Germano, U. Piomelli, P. Moin and W. Cabot, "A dynamic subgrid-scale eddy viscosity model," *Phys.Fluids,* vol. 3, pp. 1760-1765, 1991.

[35] G. Delibra, D. Borello, K. Hanjali and F. Rispoli, "Vortex structures and heat transfer in a wall-bounded pin matrix: LES with a RANS wall-treatment, Int. Journal for Heat and Fluid Flow," *Journal for Heat and Fluid Flow (Special Issue from THMT09),* vol. 31, no. 5, pp. 740-753, 2012.

[36] C. Crowe and E. Mechaelides, Multiphase Flow Handbook. Basic concepts and definitions., Boca Raton: Routledge, 2006.

[37] D. Borello, D. Anielli, F. Rispoli, A. Salvagni and P. Venturini, "Unsteady CFD analysis of erosion mechanism in the coolant channels of a rotating gas turbine blade," in *ASME Turbo Expo* , Montreal, Canada, 2015.

[38] D. Borello, L. D'Angeli, A. Salvagni, P. Venturini and F. Rispoli, "Study of particle deposition in gas turbine blades in presence of film cooling," in *ASME Turbo Expo* , Dusseldorf. Paper n. GT2014-26250, 2014.

[39] M. Andreoli, S. Gabriele, P. Venturini and D. Borello, "New model to predict water droplets erosion based on erosion test curves. Application to on-line water washing of a compressor," in *ASME Turbo Expo*, Phoenix, 2019.

[40] R. Liu, K. Chen, J. Chen, J. Zhao and M. Liang, "Simulation studies of solid-particle and liquid-drop erosion of NiAl al-loy," *Simulation,* vol. 10001184, p. 1, 2015.

[41] A. Corsini, A. Castorrini, E. Morei, F. Rispoli, F. Sciulli and P. Venturini, "Modeling of rain drop erosion in a multi-mw wind turbine," in *ASME Turbo Expo*, Montreal. Paper n. GT2015-42174, 2015.

[42] D. Borello, G. Delibra, K. Hanjali and F. Rispoli, "Hybrid LES/RANS study of tur-bulent flow in a linear compressor cascade with moving casing," in *ASME Turbo Expo*, Glasgow. Paper n. GT-2010-23755, 2010.

[43] ANSYS, Fluent Theory Guide, release 19, Southpointe: ANSYS, Inc., 2018.

[44] T.-H. Shih, W. Liou, A. Shabbir, Z. Yang and J. Zhu, "A New Eddy-Viscosity Model for High Reynolds Number Turbulent Flows Model Development and Validation," *Computers Fluids,* vol. 24, no. 3, p. 227–238, 1995.

[45] B. E. Launder and D. Spalding, "The Numerical Computation of Turbulent Flows," *Computer Methods in Applied Mechanics and Engineering,* vol. 3, p. 269–289, 1974.

[46] A. H. Lefebvre and D. R. Ballal, Gas Turbine Combustion, Boca Raton: CRC Press Taylor & Francis Group, 2010.

[47] P. Venturini, M. Andreoli, D. Borello, F. Rispoli and S. Gabriele, "Modelling of water droplets erosion on a subsonic compressor cascade," *Flow, Turbulence and Combustion,* vol. 103, p. 1109–1125, 2019.

[48] S. B. Pope, Turbulent Flows, Cambridge University Press, 2000.

[49] D. Stanton and C. Rutland, "Multi-Dimensional Modeling of Thin Liquid Films and Spray-Wall Interactions Resulting from Impinging Sprays," *International Journal of Heat and Mass Transfer,* vol. 41, p. 3037–3054, 1998.

[50] A. Yarin and D. Weiss, " Impact of drops on solid surfaces: self-similar capillary waves, and splashing as a new type of kinematic discontinuity," *Journal of Fluid Mechanics,* vol. 283, pp. 141-173, 1995.

[51] C. Mundo, M. Sommerfeld and C. Tropea, "Droplet-wall collisions: experimental studies of the deformation and breakup process," *International Journal of Multiphase Flow,* vol. 21, no. 2, pp. 151-173, 1995.

[52] F. Di Gruttola, G. Agati, P. Venturini, D. Borello, F. Rispoli, S. Gabriele and D. Simone, "Numerical study of erosion due to online water washing in axial flow compressors," in *ASME Turbo Expo*, Virtual Conference. Paper no. GT2020-14767, 2020.

[53] F. Di Gruttola, G. Agati, P. Venturini, D. Borello, F. Rispoli, S. S. Gabriele and D. Simone, "Numerical study of droplet erosion in the first-stage rotor of an axial flow compressor," in *ASME Turbo Expo*, Virtual Conference, paper no. GT2021-59661, 2021.

[54] S. Madsen and L. Bakken, "Gas Turbine Operation Offshore; On-line Compressor Wash Operational Experience,," in *ASME Turbo Expo*, Düsseldorf, 2014.

[55] E. Syverud, O. Brekke and L. Bakken, "Axial Compressor Deterioration Caused by Saltwater Ingestion," in *ASME Turbo Expo*, Power for Land, Sea and Air, Reno , 2005.

[56] E. Syverud and L. E. Bakken, " Online Water Wash Tests of GE J85-13," in *ASME Turbo Expo*, Land, Sea and Air, Reno, Nevada, USA, Paper No. GT 2005-68702, 2005.

[57] M. Hauschild, R. Ralph and S. I. Olsen, Life Cycle Assessment: Theory and Practice, Springer, 2018.

[58] Sloan Management Review, Sustainability & Innovation-Global Executive Study and Research Project, MIT, 2012.

[59] Environmental management—life cycle assessment: requirement and guidelines, Geneva: ISO 14040 (International Organization for Standardization), 2006.

[60] Environmental management—life cycle assessment: requirement and guidelines, Geneva: ISO 14044 (International Organization for Standardization), 2006.

[61] M. Huijbregts and all, "ReCiPe2016: a harmonised life cycle impact assessment method at midpoint and endpoint level," *The International Journal of Life Cycle Assessment,* vol. 22, p. 138–147, 2017.

[62] "https://simapro.com/wp-content/uploads/2019/02/DatabaseManualMethods.pdf," [Online].

[63] M. Thompson, Cultural Theory, Routledge, 1990.

[64] A. Zehnder and W. Clune, "The Three Pillars of Sustainability Framework: Approaches for Laws and Governance," *Journal of Environmental Protection ,* vol. 9, no. 3, p. DOI: 10.4236/jep.2018.93015 , 2018.

[65] I. F. A. Report, "SimaPro Database Manual Method Intergovernmental Panel on Climate Change," The Physical Science Basis, 2013.

[66] "http://www.ipcc.ch/report/ar5/wg1/," [Online].

[67] F. Brooks, "GE gas turbine performance characteristics," GE Power Systems, Report GER-3567H, 2000.

[68] A. Castorrini, A. Corsini, F. Rispoli, P. Venturini, K. Takizawa and T. Tezduyar, "Computational analysis of performance deterioration of a wind turbine blade strip subjected to environmental erosion," *Comput. Mech,* vol. https://doi.org/10.1007.

[69] Campbell Diagram- Axial Compressor, Baker Hughes Memorandum.

[70] Guide to methods for assessing the acceptability of flaws in metallic structures." BS 7910: 2013, BSI (British Standards Institution). BS 7910: 2013, 2013.

[71] S. Erkens and all, "Using Paris law to determinate fatigue characteristics a discussion," *Eighth International Conference on Asphalt Pavements. Federal Highway Administration.,* vol. 2, 1997.

[72] G. Coelho and all, "Stress Intensity Factor of Semi-elliptical Surface Crack in Internally Pressurized Hollow Cylinder—A Comparison between BS 7910 and API579/ASME FFS-1 Solutions," *Materials,* vol. 12, no. 7, p. 104, 2019.

[73] D. Borello, P. Venturini, F. Rispoli and G. Saavedra, "Prediction of multiphase combustion and ash deposition within a biomass furnace," *Journal of Applied Energy,* vol. 101, pp. 413-422, 2013.

[74] P. Venturini, D. Borello, K. Hanjalić and F. Rispoli, "Modelling of particle deposition in an environment relevant to solid fuel boilers," *Applied Thermal Engineering,* vol. 49, pp. 131-138, 2012.

[75] F. Rispoli, G. Delibra, P. Venturini, A. Corsini, R. Saavedra and T. Tezduyar, " Particle tracking and particle–shock interaction in compressible-flow computations with the V-SGS stabilization and Y Zβ shock-capturing," *Computational Mechanics,* vol. 55, p. 1201–1209, 2015.

[76] L. Cardillo, A. Corsini, G. Delibra, F. Rispoli, A. Sheard and P. Venturini, "Simulation of particle-laden flows in a large centrifugal fan for erosion prediction," in *ASME Turbo Expo*, Düsseldorf, Germany, 2014.

[77] A. Castorrini, A. Corsini , F. Rispoli, P. Venturini, K. Takizava and E. T. Tezduyar, "Computational analysis of wind turbine blade rain erosion," *Computers and Fluids,* vol. 141, pp. 175-183, 2016.

[78] D. Borello, F. Rispoli and K. Hanjalic, "Large-eddy simulations of tip leakage and secondary flows in an axial compressor cascade using a near-wall turbulence model," *Journal Power and Energy,* vol. 223, no. A6 SI, pp. 645-655, 2009.

[79] D. Borello, K. Hanjalić and F. Rispoli, "Computation of tip-leakage flow in a linear compressor cascade with a second-moment turbulence closure," *International Journal Heat Fluid Flow,* vol. 28, pp. 587-601, 2007.

[80] A. Castorrini, A. Corsini, F. Morabito, F. Rispoli and P. Venturini, "Numerical simulation with adaptive boundary method for predicting time evolution of erosion processes," in *ASME Turbo Expo* , Charlotte, North Carolina, 2017.

[81] Z. N. Kamkar, "Water Droplet Erosion Mechnisms of Ti-6Al-4V," in *Doctoral Thesis, École de Technologie Spérieure,*, Montreal, Canada , 2014.

[82] M. Ahmad, M. Schatz and M. Casey, "Experimental investigation of droplet size influence on low pressure steam turbine blade erosion," *Wear,* vol. 303, p. 83–86, 2013.

[83] "http://www.steelnumber.com," European steels and alloys. [Online].

[84] K. Brun, R. Kurz, M. Nored and J. Thorp, "Impact of continuous inlet fogging and overspray operation on GE 5002 gas turbine life and performance," in *ASME Turbo Expo*, Berlin, 2008.

[85] M. Keegan, D. Nash and M. Stack, "On erosion issues associated with the leading edge of wind turbine blades," *J. Phys. D. Appl. Phys,* vol. 46, no. 38, 2013.

[86] G. Agati, D. Borello, G. Camerlengo, F. Rispoli and J. Sesterhenn, "Direct numerical simulation of an oblique jet in a particle laden crossflow," in *ERCOFTAC workshop Direct and Large-Eddy simulations (DLES12)*, 2019.

[87] A. Castorrini, P. Venturini, A. Corsini and F. Rispoli, "Simulation of the deposit evolution on a fan blade for tunnel ventilation," in *ASME Turbo Expo*, Phoenix, 2019.

[88] A. Castorrini, P. Venturini, A. Corsini and F. Rispoli, "Numerical simulation of the blade aging process in an induced draft fan due to long time exposition to fly ash particles," *Eng. Gas Turbines Power,* vol. 141, p. 011025, 2019.

[89] V. Ryzhenkov, A. Lebedeva and A. Mednikov, "Erosion wear of the blades of wet-steam turbine stages: Present state of the problem and methods for solving it," *Thermal Engineering,* vol. 58, no. 9, pp. 713-718, 2011.

[90] K. Tsubouchi, N. Yasugahira, S. Yoshida, R. Kaneko and T. Sato, "Evaluation of water droplet erosion for advanced large steam turbine," in *ASME Power Generation Conference*, Boston USA, 1990.

[91] M. H. Keegan, D. Nash and M. Stack, "Numerical modelling of hailstone impact on the leading edge of a wind turbine blade," in *EWEA*, 2013.

[92] M. Keegan, D. Nash and M. Stack, "Modelling rain drop impact of offshore wind turbine blades," in *ASME Turbo Expo*, Copenhagen Denmark, 2012.

[93] J. Krzyzanowski, A. Kowalski and A. Shubenko, " Some Aspects of Erosion Prediction of Steam Turbine Blading," *ASME J. Engineering for Gas Turbines and Power,* vol. 116, pp. 442-451, 1994.

[94] Z. Ruml and F. Straka, " A New Model for Steam Turbine Blade Materials Erosion," *Wear,* Vols. 186-187, pp. 421-424, 1995.

[95] C. M. Lagolio, S. Guarino, D. Del Re and A. Negrotti, "Il lavaggio on-line per ottimizzare la produttività di un turbogas," in *Plant Engineering Operations/ Turbogas*, Operation, 2003, pp. 77-81.

[96] M. Wall, R. Lee and S. Frost, "Offshore gas turbines (and major driven equipment) integrity and inspection guidance notes," ESR Technology Ltd for the Health and Safety Executive. Research Report 430., 2006.

[97] F. C. Mund and P. Pilidis, "Online compressor washing: a numerical survey of influencing parameters," in *Institution of Mechanical Engineers*, 2005.

[98] PNR, "Spray Engineering Handbook. Europe.," Commercial Catalogues, 2007.

[99] G. Agati, D. Borello, F. Rispoli and P. Venturini, "An innovative approach to model temperature influence on particle deposition in gas turbines," in *ASME Turbo Expo*, Seoul, South Korea, 2016.

[100] G. Agati, D. Borello, F. Rispoli, A. Salvagni and P. Venturini, "Numerical simulation of a particle-laden impinging jet: Effect of wall curvature on particle deposition," in *ASME Turbo Expo*, Charlotte, NC (USA), 2017.

[101] G. D. G. F. J. Agati, "DNS of an Oblique Jet in a Particle-Laden Crossflow: Study of Solid Phase Preferential Concentration and Particle-Wall Interaction," *Flow, Turbulence and Combustion,* vol. 105, no. 1, pp. DOI:10.1007/s10494-020-00150-0, 2020.

[102] D. Borello, A. Corsini, M. Delibra, M. Fiorito and A. G. Sheard, "Large-eddy simulation of a tunnel ventilation fan," *Journal of Fluids Engineering,* p. doi:10.1115/1.4023686, 2013.

[103] D. Borello, A. Salvagni and K. Hanjalic, "Effects of Rotation on Flow in an Asymmetric Rib-roughened Duct: LES Study," *International Journal of Heat and Mass Transfer, Elsevier,* vol. 36, pp. 104-119, 2015.

[104] N. Neupert, J.-C. Harbeck and F. Joos, "An Experimentally Derived Model to Predict the Water Film in a Compressor Cascade with Droplet Laden Flow," *J. Eng. Gas Turbines Power,* pp. DOI:10.1115/GT2017-64121, 2017.

[105] G. Agati, F. Di Gruttola, S. Gabriele, D. Simone, P. Venturini and D. Borello, "Water washing of axial flow compressors: numerical study on the fate of injected droplets," *E3S Web of Conferences,* vol. 197, no. 9, p. DOI:10.1051/e3sconf/202019711015, 2020.

[106] J. Bröder, C. Günther and F. Joos, " Experimental Investigation of Droplets Splashing With Varying Pressures and Impact Angles to Predict Behaviour During Wet Compression," in *ASME Turbo Expo*, Oslo, Norway, 2018.

[107] J. Grove and all, "R0 GT Erosion On-Line Water Washing," GE, 2006.

[108] V. Gopala and B. Van Wachem, "Volume of fluid methods for immiscible-fluid and free-surface flows," *Chemical Engineering Journal,* vol. 141, no. 1-3, pp. 204-221, 2008.